Smart, Biocompatible Semi-conductor Nanocrystal Constructs Designed for *in-vitro* Imaging Applications

by

Jungmin Lee

B. Sc. Biological Chemistry

Bates College

Lewiston, ME

2008

Submitted to the Department of Chemistry in Partial Fulfillment of the Requirements for the Degree of

DOCTOR OF PHILOSOPHY

at the

MASSACHUSETTS INSTITUTE OF TECHNOLOGY

[June 2013]

22 April, 2013

Signature of Author

Department of Chemistry

Date

Certified By

Moungi G. Bawendi

Lester Wolfe Professor of Chemistry

Thesis Supervisor

Accepted By

Robert W. Field

Chairman, Department Committee of Graduate Students

This doctoral thesis has been examined by a committee of the Department of the Chemistry and the Department of Chemical Engineering as follows:

Profssor Troy Van Voorhis

Chairman

Profssor Moungi G. Bawendi

Thesis Supervisor

Profssor Klavs F. Jensen

Department of Chemical Engineering

Smart, Biocompatible Semi-conductor Nanocrystal Constructs Designed for *in vitro* Imaging Applications by

Jungmin Lee

Submitted to the Department of Chemistry on 22 April, 2013, in partial fulfillment of the requirements for the degree of Doctor of Philosophy in Chemistry

ABSTRACT Quantum dots (QDs) have unique optical properties that complement fluorescent proteins and organic fluorophores. Despite the widespread use as a fluorescent label in biological imaging studies, the types of biological questions answered by utilizing QDs have been limited due to crucial shortcomings. This thesis focuses on pushing the boundaries of QD applications *in vitro*, exploring improvements in construct design and methodology to overcome these shortcomings. First, the issues of non-specific binding and reactivity are alleviated by exploring a new method to conjugate molecules onto the QD surface. The improvements that were made enabled a collaborator situated across the country to conjugate biomolecules in a one-step process without performing the usual amine/N-hydroxysuccinimide coupling, thereby diminishing non-specific binding.

The utility of QDs in biological applications is further demonstrated by incorporating the nanocrystals into a dynamic sensor construct and taking measurements in a bioenvironment. A dye construct that can act as a Fluorescent Resonant Energy Transfer (FRET) acceptor is conjugated to the FRET donor QD through a molecular linker whose conformation changes depending on the analyte in the microenvironment. As a proof-of-concept, pH is chosen as the environmental factor and the QD-dye FRET sensor is used to track the pH in subcellular compartments along the endocytosis pathway.

Lastly, a new microfluidic device is used to deliver QDs into the cell cytosol with high viability and high throughput. QDs delivered this way are shown to be non-aggregated and to interact with the cytosolic environment, opening up the possibility of single molecule tracking of a specific protein of interest inside the cytosol.

Thesis Supervisor: Moungi G. Bawendi, Ph.D.
Title: Lester Wolfe Professor of Chemistry

Preface

Chapters from this thesis were reproduced in part from the following references:

Kay ER, **Lee J**, Nocera DG, Bawendi MG. Conformational Control of Energy Transfer: A Mechanism for Biocompatible Nanocrystal-Based Sensors. Angewandte Chemie International Edition 2013, 52: 1165-1169.

Lee J, **Sharei A**, Sim WY, Adamo A, Langer R, Jensen KF, Bawendi MG. Nonendocytic Delivery of Functional Engineered Nanoparticles into the Cytoplasm of Live Cells Using a Novel, High-Throughput Microfluidic Device. Nano Letters 2012, 12: 6322-6327.

Huang J, **Lee J**, Bawendi MG, Davis MM. Stable, small and low-valency streptavidin-coupled quantum dots for single-molecule imaging. *Manuscript in preparation*

Contents

Chapter 1

Introduction to Semiconductor Nanocrystals and Their Use in Biological Research

1.1 The Unique Characteristics of Semiconductor Nanocrystals, or Quantum Dots (QDs)

1.1.1 An Analogy to the Atom, in the Nanoscale

Quantum Dots (QDs) have catapulted to widespread use in biological imaging [1],[2], photovoltaic cells [3], and lighting devices [4]. Thanks to extensive characterization, we now have a comprehensive understanding of QDs. In order to explain the properties of QDs that make them so appealing for these applications, we can take an analogy to the particle-in-a-box approach and apply it to semiconductor materials [5].

It is well known that the electronic structure of bulk semiconductors is characterized by two bands consisting of continuous energy states, the conduction band and the valence band. Under the most simplifying assumptions, the conduction and valence band are both isotropic and parabolic. Their energies vary as a continuous function

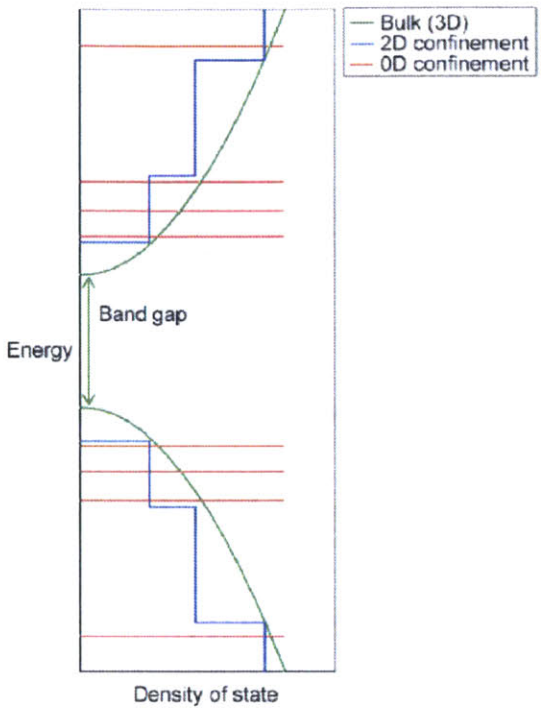

Figure 1-1: A simplified illustration of the changes in the density of energy states in a semiconductor material as the boundary conditions move from **green** bulk, **blue** 2D surface, and **red** spherical limits.

of k^2, where k is the wave vector (Fig. 1-1a). However, as more boundary conditions are imposed, the density of states becomes no longer continuous (Fig. 1-1 blue, red lines). Due to the inverse relationship between the ΔE and the size of confinement, this model predicts that the energy of the exciton will increase as the crystallite radius R^2 is decreased.

However, because of the Coulomb attraction between the electron and the hole, quantum confinement effects govern the optical and electronic properties of QDs only for a specific size range. We can assume that the confinement term dominates the Coulomb attraction term for nanocrystals smaller than the Bohr radius of the material, which is in the neighborhood of $\sim$5 nm for commonly used QD materials. Theoretically, there can therefore be some variation not only in the nanocrystal material but also in the nanocrystal size, as long as the matter is a semiconductor and the size is within the Bohr radius. Currently, we have the ability to synthesize high-quality

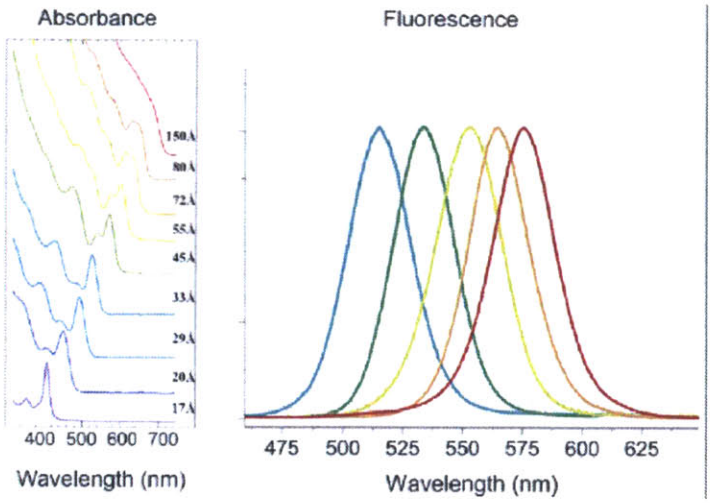

Figure 1-2: The tunability of emission and absorption wavelengths of nanocrystals by crystallite radius ($\AA$). Image reproduced from W. Liu, Ph.D. Thesis, MIT, 2010.

QDs with a limited number of materials: CdSe have been the most conventional but others such as InAs have also been developed. Currently, we can reliably achieve a monodisperse, stable solution of nanocrystals of sizes as small as 1 nm to as large as >5 nm. This tunability in material and size translates directly to tunability in emission wavelength. The QDs used in this project all consist of CdSe cores overcoated with either a CdZnS or CdS shell that passivate the CdSe surface. The Bohr radius is 56 $\AA$ for CdSe, and CdSe cores between a radius of 17 $\AA$ to ~50 $\AA$ correspond to emission in the visible wavelength (Fig. 1-2).

The CdZnS or CdS shell results in a Type-I core-shell architecture in which the electron and hole are both confined within the CdSe core. 4-5 lattice layers of such shell material passivates surface defects on the CdSe core that would otherwise cause non-radiative recombination of the electron and the hole. For more background on the Type-I core-shell structure, see references [6] and [14].

1.1.2 Overview of Core/Shell Quantum Dot (QD) Synthesis

Historically, a number of different synthesis precursors and methods have been tried [7]. For the QDs used in this project, the two CdSe core synthesis methods used either

$Cd(AcAc)_2$ or CdO as cadmium precursors. In addition, two methods were used for overcoating the cores, one for a CdZnS shell from extremely reactive precursors and one for a CdS shell from less reactive precursors. The protection of CdSe and the mitigation of surface traps result in QDs that have much higher storage stability and higher quantum yield [12]. In addition, the presence of a thick shell can greatly increase the absorption cross-section of the nanocrystals, contributing to even brighter QDs [9]. The core and the shell synthesis method were chosen based on the desired emission wavelength and the width of the emission peak required for the application. In the Bawendi group, QD synthesis methods are constantly being improved and advanced; for example, Dr. Ou Chen has recently developed extremely high quantum yield, low blinking QDs that emit in the visible wavelengths [10].

For QDs that emit in the green or yellow (510-580 nm), CdO core preparation (Fig. 1-3) followed by a CdS overcoating procedure (Fig. 1-4) will yield high quality nanoparticles. This highly reliable method was developed by Peng et al.[11], who showed that a Cd-phosphonic acid complex could be generated first by heating CdO with tetradecylphosphonic acid (TDPA) in TOP/TOPO. In this method, CdO is heated in TOP/TOPO in the presence of TDPA at 340 °C under nitrogen in order to "crack" the CdO into a clear solution. Non-coordinating solvents such as 1-octadecene and other fatty acids may also be used; both [12] and [13] are good references for an analysis of their effects. After cracking the CdO, TOP-Se is rapidly injected into the solution at 360 °C to produce high quality, monodisperse CdSe nanocrystals that can be so small that its first absorption feature is around 480-490 nm. For this project, CdSe synthesized from a CdO precursor was overcoated with a Cd_1S_1 shell. The shell was synthesized by simultaneously[1] injecting a Cd precursor consisting of Cd-oleate and decylamine in a 1:2 molar ratio in octadecene (ODE)/TOP, and a S precursor consisting of hexamethyldisilathiane $[(TMS)_2S]$ in TOP. The quantum yield of CdSe/CdS QDs synthesized by this procedure have been as high as unity [14].

Even though the quantum yield is lower, the older $Cd(AcAc)_2$ core preparation

[1]The SILAR method that Andrew Greytak from reference [14] described is not necessary. We have found that while the general Cd-oleate method is a significant advance, the SILAR injection sequence does not make a difference.

(Fig. 1-3) followed by a CdZnS overcoating procedure (Fig. 1-4) can achieve precise targeting of redder emission wavelengths (590-620 nm). In this method, Cd^{2+} is reduced to elemental cadmium using dodecanal in a solution of TOP, forming a yellow colored homogenous solution [15]. The elemental Cd precursor solution is then introduced simultaneously with TOP-Se into a solution of TOP/TOPO at high temperature, typically 300°C, to produce monodisperse and crystalline nanocrystals. For these CdSe nanocrystals, a $Cd_xZn_{1-x}S$ shell was used to overcoat the cores. The shell was synthesized by careful addition of the highly reactive precursors dimethyl cadmium ($CdMe_2$), diethylzinc ($ZnEt_2$) and bis(trimethylsilyl)sulfide (TMS_2S) simultaneously into a solution of CdSe QD cores and hexadecylamine (HDA) in TOP/TOPO.

1.1.3 QD Preparations for Applications

QDs synthesized either way can now be used for applications such as use in light-absorbing devices [16], explorations in quantum phenomena [49], and fluorescent tagging in biological microscopy [18]. For each of these applications, the nanocrystals require a different method of sample preparation. In order to be used in biological microscopy as a fluorescent label, QDs should be water-soluble and programmable, in addition to being inert towards surfaces and molecules present in the bioenvironment. For this project, we focus on how to improve QD-based fluorescent labels so that they can complement fluorescent proteins (FPs) and organic fluorophores.

1.2 An Introduction to *in-vitro* Applications of QDs in Fluorescence Microscopy

1.2.1 Conventional Fluorophores

In the recent decades, fluorescence microscopy has enormously advanced our understanding of biological processes such as protein trafficking, cellular movements, and *in-vivo* circulation [19]. Advances in microscopy techniques such as confocal, multi-photon, 4Pi, and total internal reflection techniques have provided access to smaller

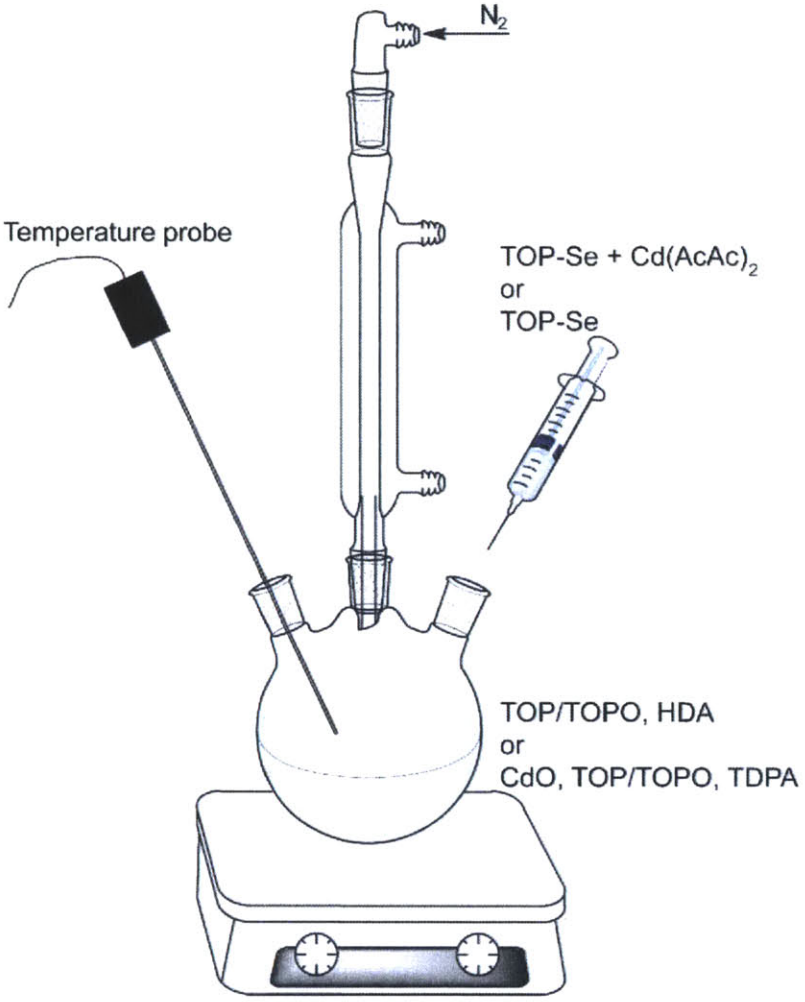

Figure 1-3: An overview of the glassware setup for synthesizing CdSe cores.

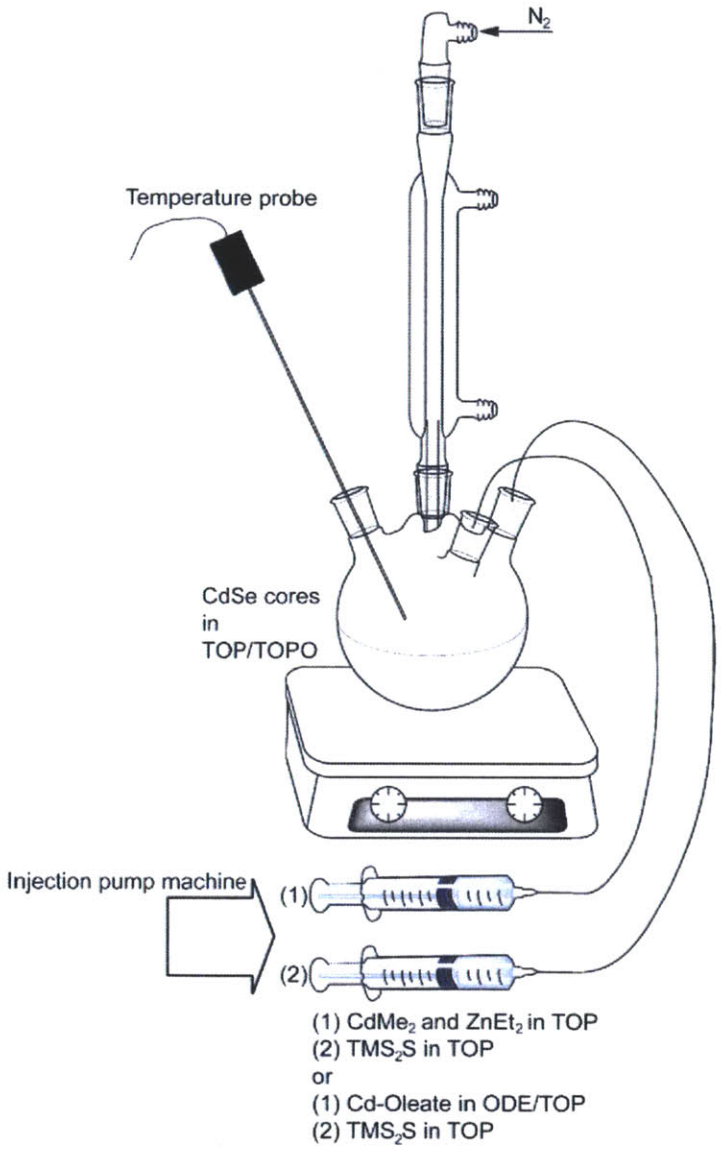

Figure 1-4: An overview of the glassware setup for overcoating CdSe cores with either a CdS or CdZnS shell.

resolution; advances in microscope parts have enabled faster acquisition. The use such fluorescence microscopy techniques would not have been possible without the discovery of GFP analogues (fluorescent proteins, FPs) and small organic fluorophores. However, both FPs and organic dyes have multiple shortcomings. First, each fluor has a different optimal absorption wavelength, which necessitates multiple excitation sources. Second, most conventional fluorophores emit at a broad range of wavelengths. This results in leakage among wavelength windows and restricts the possibility of using multiplexed imaging to investigate multiple biological interactions. The third and crippling fact is that the conventional fluorescent molecules photobleach. Therefore, more versatile and robust dyes are needed in order to probe biological phenomena that were previously inaccessible using fluorescence microscopy techniques.

1.2.2 The Niche for QD-based Fluorescence Probes in Biology

QDs are a newer generation of widely used fluorescent probes that are now used to complement organic dyes and FPs for some of the more sophisticated microscopy techniques. QDs serve as powerful fluorescent probes that are compact in size, extremely photostable, tunable in emission, and have large multi-photon cross sections. The nanoparticles also present advantages for multiplexing, due to their broad absorption bandwidth and narrow emission peak. However, the current preparation methods must be further improved and optimized in order to bring QDs to the level of convenience and widespread usage of FPs and dyes.

1.3 Building QD Constructs for Biological Applications

1.3.1 Current Methods of QD Encapsulation

Core-shell QDs as synthesized are encapsulated in long-chain alkyl ligands. Both the naked core-shell QDs and alkyl-ligand encapsulated core-shell QDs are insoluble in polar solvents. Since the universal solvent in all bioenvironments is water, QDs have to be processed to render them water-soluble. This requires a ligand that can multitask, binding to the QD and also interacting favorably with water. More traditional methods have made use of amphiphilic lipids consisting of alkyl chain(s) and a water-soluble headgroup, either a charged moiety or a water-soluble polymer (Fig. 1-5a). The hydrophobic lipid chains of such ligands can intercalate with the alkyl ligands on the QD, and the water-soluble headgroup brings the entire nanoparticle into water [6].

Recently, we have evolved from using a sulfide-based ligand to replace the native alkyl ligands on the QD by replacing the sulfide groups with imidazole groups. The old ligands rely on sulfides that strongly chelate to the nanoparticle's metal surface, which works as an anchor to either a carboxylic group or a polymeric water-solubilizing group such as poly(ethylene)glycol (PEG) (Fig. 1-5b). This method is problematic for two reasons. One, the sulfide group is so strongly chelating that it may leach metal ions from the nanocrystal, decreasing its quantum yield. Two, disulfide groups often used to anchor the ligand onto the QD surface tend to oxidize, not to mention show sensitivity to high pH [21]. For example, one of the most widely used sulfide ligands is based on dihydroxy lipoic acid (DHLA), which will oxidize to the energetically favored lipoic acid. Upon oxidation to lipoid acid, the ligand can no longer chelate to the nanocrystal surface and will fall off; therefore, QDs ligand-exchanged with DHLA-based water-solubilizing ligands will stay dissolved and fluorescent in water only for a limited amount of time. The new generation of ligands is now used almost exclusively in the Bawendi group. Developed by Wenhao Liu, the ligand is a polymer synthe-

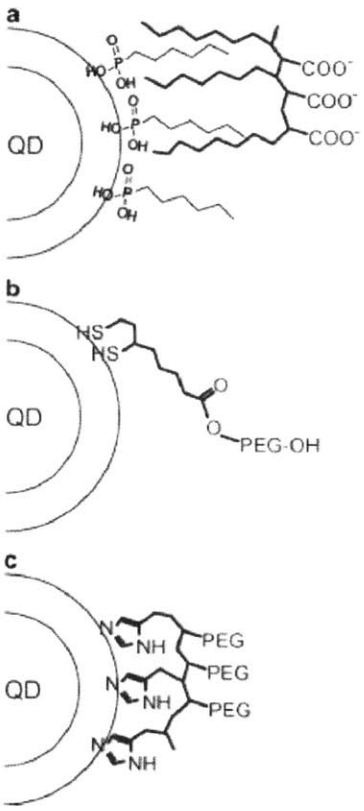

Figure 1-5: Methods that are used to solubilize QDs in an aqueous solvent. Most QDs have moved away from using intercalating amphiphilic ligands onto the native long-chain hydrophobic alkyls (**a**) to replacing the native alkyl ligands with sulfide (**b**) or imidazole (**c**) based ligands.

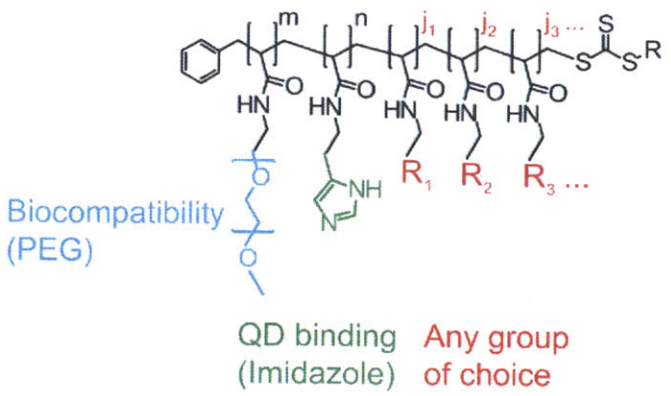

Figure 1-6: The components of the PIL and each of its role.

sized from 3-4 different types of molecules as monomers: QD-chelating monomers, water-solubilizing monomers, conjugatable (e.g., amine containing monomers), and any other functional monomers of choice as demonstrated in figure 1-6. The poly-imidazole ligands (PIL) rely on the metal affinity of imidazole group, strengthened by the multiple imidazole units on a single polymer strand. Methoxy-terminated PEG groups (mPEG) are used as a non-biofouling, neutral water-solubilizing group; a reactive moiety such as an amine-terminating PEG groups are used as a conjugation handle. This work was published in 2010 [4].

1.3.2 The PIL

The invention of the PIL revolutionized the way this group prepares QDs for biological applications. The PIL design widened the range of QD applications by endowing QD-based constructs with:

- Excellent stability in solution with respect to pH (5.5-10.5), temperature, and long-term storage
- Maintenance of high QY after ligand exchange
- Biocompatiblility and non-toxicity upon interaction with cells and with animals
- Low non-specific binding (low biofouling) with various proteins and other biomolecules in solution

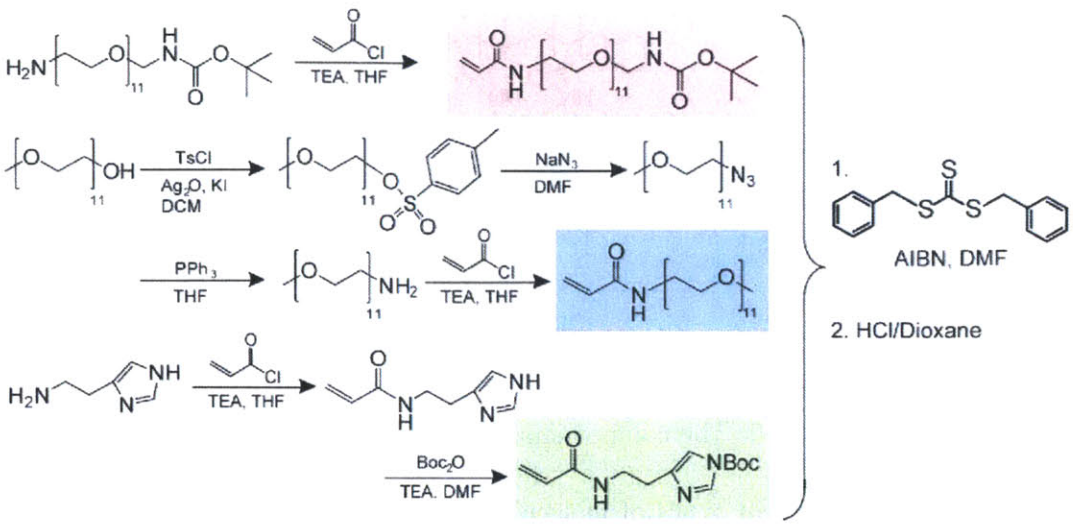

Figure 1-7: Scheme that illustrates the synthesis of commonly used PIL monomers and their polymerization.

- Ability to change the contents of the polymer in a modular fashion

The last point is particularly powerful. The PIL allows us to realize many complicated, multifunctional QD-based sensor and construct designs quite easily. Figure 1-7 describes the typical PIL synthesis scheme. The PIL synthesis and individual variations are described in detail within each chapter.

1.3.3 Overview of QD Ligand Exchange and Surface Derivatization

Ligand exchange using PIL is highly reproducible and relatively forgiving. First, QDs are prepared by gently crashing out the core-shell nanocrystals with polar solvents and centrifuging into a pellet. The solvents used to crash out QDs are methanol for HDA/TOP/TOPO coated CdSe/CdZnS and a combination of chloroform and ethanol for ODE-coated CdSe/CdS. The precipitation removes excess organic molecules in free solution and allows a solvent change upon dissolution of the pellet into 50 μl of chloroform. Then, PIL is prepared by taking the polymer at a 2 nmol QD: 5 mg PIL ratio, and dissolving into 30 μl of chloroform. The QD solution and the PIL solution are then gently stirred together for ~15-20 min, followed by an increase in the overall

polarity of the solution by addition of 30 μl of methanol. This solution is stirred for another ~30-45 min, at which point the ligand exchange should be complete and the QD-PIL construct can be crashed out by addition of hexanes. Successfully ligand-exchanged QD-PILs will often form a gel-like pellet when centrifuged. This pellet is redissolved in methanol as a method to check the solubility in polar solvents and also as a method to evaporate leftover chloroform, hexanes, and ethanol. Even though the QD:PIL ratio is optimized here, this procedure is surprisingly forgiving to slight increases in the amount of PIL, actual volumes of the solvents, and reaction times. There are other factors along this ligand exchange procedure that can be tweaked for newer generations of QDs:

- Size-selective QD crash out: For a nanoparticle solution that has a wide size distribution, a succession of two crashouts, one extremely light (centrifugation after the slightest clouding of QD solution) followed by an actual crash out (centrifugation after sustained clouding of QD solution). This removes the larger nanoparticles, as their flocculation happens more easily upon addition of a polar solvent. This is casually known as a size-selective crash out [23].

- Successive crash outs: For some QD growth solutions that are suspected of impurities, it may be necessary to add a succession of polar solvents until there is a light clouding, and removing the impurities by centrifuging to remove the pellet. Each time, the solution should be centrifuged and the pellet of impurities should be discarded. For example, some InAs/CdZnS growth solutions contained impurities that crashed out as white salts when ethanol was added.

- Slowly increasing the polarity: Instead of a single addition of 30 μl of methanol, we may change the strength, volume, number of additions, and stirring times of the polar solvent.

The conventional method of QD conjugation to another molecule (dyes, proteins) makes use of amine-containing PILs. Unfortunately, the usual sequence of ligand exchange-water solubilization-molecule conjugation, causes non-specific binding of

QD constructs to proteins. In fact, the current methods to conjugate QDs to other molecules have a number of shortcomings.

1.3.4 Shortcomings of QD-Based Fluorescent Labels

Recent advances have partially addressed some of these disadvantages of using QDs as opposed to FPs or dyes. There can be four main concerns when using QDs as fluorescent labels:

Size Organic fluorophores such as Alexa®and ROX fluors can span as small as 5-6 aromatic rings (1-2 nm). FPs have also been extensively engineered to be small, now about 26.9 kD for GFP, which is as compact as ~4.2 nm in hydrodynamic diameter (HD). In the case of QDs, our group routinely makes water-solubilized QD constructs that are 12-13 nm in HD. The differential between the inorganic nanocrystal (~3.5-6 nm in diameter) and the water-solubilized construct is mainly due to the PEG layer. While PEG endows incredible biocompatibility and water solubility to the QDs, it also increases the overall size of the construct. Some research points to using zwitterionic ligands in place of PEG as an effective solution to decreasing the size of the overall construct [24].

Delivery So far, QDs have been useful mostly in cell-surface protein labeling studies [25]. Cytosolic protein labeling in live cells has been limited because nanoparticle delivery into the cell cytosol is difficult. Two hurdles prevent nanoparticles from crossing the phospholipid bilayer: one, the relatively large HD, and two, the polar water-solubilizing coating on the nanoparticle surface. A variety of methods are currently being explored, including endosome escape [26] and liposome fusion [27]. Fluorescent proteins, on the other hand, can be engineered at the plasmid level to be synthesized and trafficked to the correct compartment.

Targeting - Non-specific binding FPs also have perfect targeting since its genetic code can be inserted next to the protein of interest at the plasmid level. Both

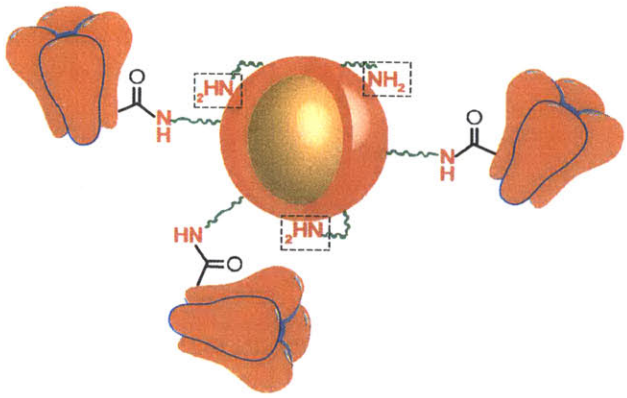

Figure 1-8: A simplified illustration of a QD that has unreacted amines on the surface after amide-coupling with targeting moieties (e.g., streptavidin). These amines remain unreacted because of an affinity to the QD surface and contribute a positive charge to the construct (dotted boxes), causing non-specific binding.

organic dyes and QD-based labels, however, have to be targeted using extraneous interactions. Most commonly used today are antibodies and streptavidin. The necessity of a targeting moiety can be problematic because it increases the construct size and complicates both the QD construct synthesis and labeling procedure. Yet another problem is the fact that this targeting may not be perfect. Conjugating a targeting moiety usually requires amine groups on QD. Because amine groups have some affinity towards the QD's metal surface, some amines remain unreacted and contribute an overall positive charge to the QD construct (Fig. 1-8). Ultimately, the positive charge due to unreacted amines will cause non-specific interactions that are energetically favorable such as dipole or amine-based charge interactions; QD labels therefore require extensive optimization of the surface chemistry and need control studies [18].

Lack of valency control The ability to label a single protein of interest with a single QD is important in probing biological processes in live cells. If a single protein is labeled by more than one QD as in figure 1-9b, then the bulky size of the labeled biomolecule may affect its function by slowing its trafficking or preventing it from entering small compartments. If a single QD labels two or more proteins (Fig.1-9c), the forced proximity between the proteins may trigger biological pathways by

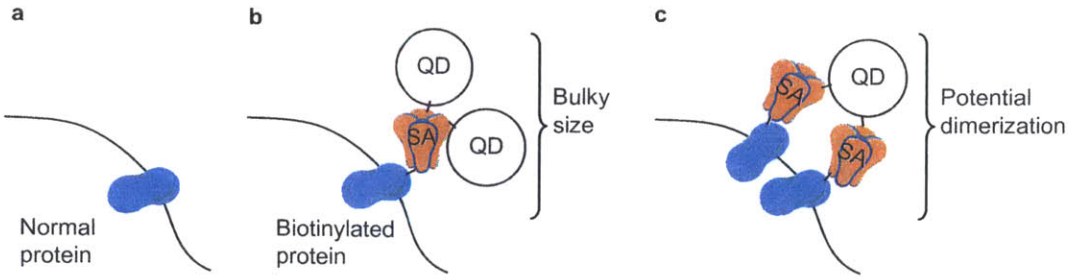

Figure 1-9: Illustration of the effects of quantum dot labeling on a protein of interest. **a** Normal protein of interest. **b** Protein of interest that has been labeled by two QDs through a streptavidin-biotin binding, demonstrating the significant increase in size. **c** Two proteins of interest that have been brought to proximity due to being labeled with one QD that has two streptavidins conjugated onto its surface, increasing the possibility of dimerization or interactions.

causing aggregation or dimerization. Since plasmids can be engineered to contain just one fluorescent protein next to the protein of interest, FPs have perfect valency control. So far, the only method that purified single streptavidin per QD and used such constructs in a biological experiment was developed by the Bawendi group and the Ting group [1].

1.4 Fluorescent Sensors for Biological Applications

1.4.1 Introduction to FRET

Fluorescence resonance energy transfer (FRET) has been instrumental in verifying the distance between proteins and their interactions. In FRET, the energy from a photo-excited donor is non-radiatively transferred to an energy acceptor, which can then emit the photon energy. The rate of energy transfer from donor (D) to acceptor (A), k_{DA}, is expressed as:

$$k_{DA} = \frac{1}{\tau_D}\left(\frac{R_0}{r}\right)^6 \tag{1.1}$$

where τ_D is the lifetime of the donor's excited state, r is the actual distance between the donor and the acceptor, and R_0 is the characteristic Forster distance dependent on the identity of the D and A. The R_0 depends on factors such as the overlap between

the D emission spectrum and the A absorbance spectrum:

$$R_0 = \frac{9000ln(10)\phi_D\kappa^2}{128\pi^5 n^4 N_A} J \tag{1.2}$$

Here, ϕ_D is the quantum yield of the donor in the absence of the acceptor, κ is the dipole orientation of the D and A, n is the refractive index of the medium, and N_A is Avogadro's number. J is the spectral overlap term, which is an integral expressed as

$$J = \int_0^\infty f_D(\lambda)\epsilon_A(\lambda)\lambda^4 d\lambda \tag{1.3}$$

involving $f_D(\lambda)$, the emission spectrum of D, and the molar extinction coefficient of A, $\epsilon_A(\lambda)$, all as a function of the wavelength. Oftentimes, we calculate the FRET efficiency with the number(x) of acceptors and the distance(r) between D and A as variables:

$$E = \frac{xR_0^6}{xR_0^6 + r^6} \tag{1.4}$$

1.4.2 Using QDs for FRET Sensors

A survey of the factors involved in the FRET process shows that choosing the right donor and acceptor is important. QDs are useful for FRET applications because of their tunable and narrow emission, which can be targeted to overlap with the acceptor's absorbance but not leak into the A's emission window. The FRET process is also extremely sensitive to r, the actual distance of the D and A. Therefore, by designing a construct whose r changes according to the microenvironment, we may translate chemical changes into spectral changes.

1.5 Thesis Overview

Some of the issues described in section 1.3.4 are tackled in the following chapters. In chapter 2, we describe a method to diminish non-specific binding as much as possible by changing the method of QD conjugation. The construct is also designed so

that the QDs can be transported in room temperature over large distances to biologists and immediately rendered reactive. This flexibility vastly widens the possibility of collaboration amongst nanoparticle chemists and biologists, enabling biologists to use more tailored, higher quality QD constructs. In our project, we collaborate with Stanford biologists who have engineered streptavidin to possibly enable purification of different valencies of streptavidin-QD constructs shown in figure 1-9.

Chapter 3 focuses on harnessing the optical properties of QDs and the versatility of PIL to synthesize a QD-based pH sensor. The QD-based sensor is used as a proof-of-concept to demonstrate that our constructs can be used in the biological environment.

In chapter 4, a new method based on a microfluidic device is used to deliver nanoparticles into live cells. In addition, the delivered nanoparticles are found to interact with the cytosolic environment, opening up the possibility to deliver QD constructs designed to target specific proteins of interest. This method preserves high viability, has high throughput, and bypasses endocytosis. By successfully demonstrating cytosolic delivery of QD constructs, we open up the possibility to specifically target a huge variety of cytosolic proteins to probe their functions.

Bibliography

[1] Dubertret, B.; Skourides, P.; Norris, D. J.; Noireaux, V.; Brivanlou, A. H.; Libchaber, A. In Vivo Imaging of Quantum Dots Encapsulated in Phospholipid Micelles. Science 2002, 298, (5599), 1759-1762.

[2] Jamieson, T.; Bakhshi, R.; Petrova, D.; Pocock, R.; Imani, M.; Seifalian, A.M. Biological application of quantum dots. Biomaterials 2007, 28, 4717-4732.

[3] Lee, H. J.; Yum, J. H.; Leventis, H. C.; Zakeeruddin, S. M.; Haque, S. A.; Chen, P.; Seok, S. I.; Grazel, M.; Nazeeruddin, M. K., CdSe quantum dot-sensitized solar cells exceeding efficiency 1% at full-sun intensity. Journal of Physical Chemistry C 2008, 112, (30), 11600-11608.

[4] Caruge, J. M.; Halpert, J. E.; Wood, V.; Bulovic, V.; Bawendi, M. G., Colloidal quantum-dot light-emitting diodes with metal-oxide charge transport layers. Nat. Photonics 2008, 2, (4), 247-250.

[5] Efros, A. L.; Rosen, M., The electronic structure of semiconductor nanocrystals. Annu. Rev. Mater. Sci. 2000, 30, 475-521.

[6] Dabbousi, B.O.; Rodriguez-Viejo, J.; Mikulec, F.V.; Heine, J.R.; Mattoussi, H; Ober, R.; Jensen, K.F.; Bawendi, M.G. (CdSe)ZnS CoreShell Quantum Dots: Synthesis and Characterization of a Size Series of Highly Luminescent Nanocrystallites. J. Phys. Chem. B, 1997, 101 (46): 94639475.

[7] Grieve, K.; Mulvaney, P.; Grieser, F. Synthesis and electronic properties of semiconductor nanoparticles/quantum dots. Curr. Op. Coll. Interface. Sci. 2000, 5(1-2):168-172.

[8] Yu, Z.; Guo, L.; Du, H.; Krauss, T.; Silcox, J., Shell Distribution on Colloidal CdSe/ZnS Quantum Dots. Nano Lett. 2005, 5, (4), 565-570.

[9] Sun, Q.; Wang, Y.A.; Li, L.S.; Wang, D.; Zhu, T.; Xu, J.; Yang, C.; Li, Y. Bright, multicoloured light-emitting diodes based on quantum dots. Nat. Photonics. 2007, 1, 717-722.

[10] Chen, O.; Zhao, J.; Chauhan, V.P.; Cui, J.; Wong, C.; Harris, D.K.; Wei, H.; Han, H.S.; Fukumura, D.; Jain, R.K.; Bawendi, M.G. Compact high-quality CdSeCdS coreshell nanocrystals with narrow emission linewidths and suppressed blinking. Nat. Mat. 2013, ASAP.

[11] Peng, Z. A.; Peng, X., Formation of High-Quality CdTe, CdSe, and CdS Nanocrystals Using CdO as Precursor. J. Am. Chem. Soc 2000, 123, (1), 183-184.

[12] Yu, W. W.; Peng, X. G., Formation of high-quality CdS and other II-VI semiconductor nanocrystals in noncoordinating solvents: Tunable reactivity of monomers. Angewandte Chemie-International Edition 2002, 41, (13), 2368-2371.

[13] Pradhan, N.; Reifsnyder, D.; Xie, R.; Aldana, J.; Peng, X., Surface Ligand Dynamics in Growth of Nanocrystals. Journal of the American Chemical Society 2007, 129, (30), 9500-9509.

[14] Greytak, A.; Allen, P.M.; Liu, W.; Zhao, J.; Young, E.R.; Popovic, Z.; Walker, B.J.; Nocera, D.G.; Bawendi, M.G. Alternating layer addition approach to CdSe/CdS core/shell quantum dots with near-unity quantum yield and high on-time fractions. Chemical Science. 20120, 3, 2028-2034.

[15] Stott, N. E. Novel synthetic routes to high-quality II-VI colloidal nanocrystals: controlled growth using mild precursors in the presence of selected ligands. Ph.D. Thesis, Massachusetts Institute of Technology, 2004.

[16] McDonald, S. A.; Konstantatos, G.; Zhang, S. G.; Cyr, P. W.; Klem, E. J. D.; Levina, L.; Sargent, E. H., Solution-processed PbS quantum dot infrared photodetectors and photovoltaics. Nature Materials 2005, 4, (2), 138-U14.

[17] Empedocles, S.A.; Norris, D.J.; Bawendi, M.G. Photoluminescence Spectroscopy of Single CdSe Nanocrystallite Quantum Dots. Phys. Rev. Lett. 1996, 77, 38733876.

[18] Gao, X.; Yang, L.; Petros, J.A.; Marshall, F.F.; Simons, J.W.; Nie, S. In vivo molecular and cellular imaging with quantum dots. Current Opinion in Biotechnology 2005, 16:6372.

[19] Hurtley, S.M. and L. Helmuth, The Future Looks Bright. Science, 2003. 300(5616) : p. 75.

[20] Smith, A. M.; Duan, H.; Rhyner, M. N.; Ruan, G.; Nie, S., A systematic examination of surface coatings on the optical and chemical properties of semiconductor quantum dots. Phys. Chem. Chem. Phys. 2006, 8, 3895-3903.

[21] Pons, T.; Uyeda, H. T.; Medintz, I. L.; Mattoussi, H., Hydrodynamic Dimensions, Electrophoretic Mobility, and Stability of Hydrophilic Quantum Dots. J. Phys. Chem. B 2006, 110, (41), 20308-20316.

[22] Liu, W.; Greytak, A.B.; Lee, J.; Wong, C.R.; Park, J.; Marshall, L.F.; Jiang, W.; Curtin, P.N.; Ting, A.Y.; Nocera, D.G.; Fukumura, D.; Jain, R.K.; Bawendi, M.G. Compact Biocompatible Quantum Dots via RAFT-Mediated Synthesis of Imidazole-Based Random Copolymer Ligand. JACS 2010, 132: 472-483.

[23] Murray CB, Norris DJ, Bawendi MG. Synthesis and characterization of nearly monodisperse CdE (E = sulfur, selenium, tellurium) semiconductor nanocrystallites. J. Am. Chem. Soc. 1993, 115: 8706-8715.

[24] Muro, E.; Pons, T.; Lequeux, N.; Fragola, A.; Sanson, N.; Lenkei, Z.; Dubertret, B. Small and Stable Sulfobetaine Zwitterionic Quantum Dots for Functional Live-Cell Imaging. JACS. 2010, 132(13):4556-4557.

[25] Medintz, I.L.; Uyeda, H.T.; Goldman, E.R.; Mattoussi, H. Quantum dot bioconjugates for imaging, labelling and sensing. Nat. Mat. 2005, 4, 435-446.

[26] Delehanty, J.B.; Bradburne, C.E.; Boeneman, K.; Susumu, K.; Farrell, D.; Mei, B.C.; Blanco-Canosa, J.B.; Dawson, G.; Dawson, P.E.; Mattoussi, H.; Medintz, I.L. Delivering quantum dot-peptide bioconjugates to the cellular cytosol: escaping from the endolysosomal system. Integr. Biol. 2010,2, 265-277.

[27] Kobayashi, S.; Nakase, I.; Noriko, K.; Yu, H.; Pujals, S.; Imanishi, M.; Giralt, E.; Futaki, S. Cytosolic Targeting of Macromolecules Using a pH-Dependent Fusogenic Peptide in Combination with Cationic Liposomes. Bioconjugate Chem., 2009, 20 (5):953959.

[28] Howarth, M.; Liu, W.; Puthenveetil, S.; Zheng, Y.; Marshall, L.F.; Schmidt, M.M.; Wittrup, D.K.; Bawendi, M.G.; Ting, A.Y. Monovalent, reduced-size quantum dots for imaging receptors on living cells. Nature Methods. 2008, 5, 397-399.

Chapter 2

Improving QD-Based Fluorescent Probes

2.1 The Need to Optimize Conventional QD-Biomolecule Constructs

Fluorescence microscopy has been extremely useful in biology with the development of fluorescent dyes and proteins in the recent decades [1]. However, imaging many complex processes require a fluorescent probe that is small but with bright, photostable, and versatile optical properties [2]. Quantum dots (QDs), a semiconductor nanoparticle, have been used widely to complement conventional organic dyes and fluorescent proteins (FPs) due to their photostability, brightness, broad absorption, and narrow emission [20]. However, most immediately available QDs are large in size and lack the precise, valency-controlled labeling of proteins of interest (POI). Thus, the construct size and multivalency of labeling pose two major challenges when using QDs as fluorescent probes. To harness the attractive optical properties of QDs, it would be ideal to minimize their size to avoid steric effects and to have monovalent binding valency to avoid crosslinking uncertainties. QD preparation is quite different from those of dyes and FPs, relying heavily on organic ligands. Thus QDs need to be passivated with a ligand that renders the nanoparticles soluble in aqueous

media. Such a ligand also needs to provide the ability to conjugate a biomolecule that targets the POI. Previously, we developed and demonstrated that passivation with poly-imidazole ligand (PIL) results in stable water-solubilized QDs that can be conjugated to targeting biomolecules [4]. QD passivation and water-solubilization is followed by amines on the ligands reacting with N-hydroxysuccinimide-(NHS) or maleimide-activated biomolecules. However, this conjugation sequence presents two problems. First, some of the amines stay unreacted due to amine interaction with the QD surface; PEG groups, often used as water-solubilizing moieties on the ligands, make amines even more inaccessible to the NHS reaction by creating steric hindrance between amines on the QD surface and the biomolecule. Ultimately, these two factors together de-crease NHS reaction yield, and the unreacted amines later contribute to non-specific binding to various surfaces other than the POI [4]. The low conjugation yield also makes it difficult to control the valency of the targeted biomolecule per QD due to the large number of amines needed. Multiple binding sites per QD may also result in the aggregation of POI, which may have inadvertent consequences such as activating biological pathways. Yet another issue with NHS- and maleimide activating schemes is that both groups are unstable even in moderately basic aqueous media (half-life = 10 min and 6 h at pH 8.5-8.6, respectively), limiting the long-distance delivery of conjugatable, water-soluble QDs from chemists to biologists for subsequent biomolecule conjugation. This stability problem persists for innovative conjugation chemistries such as norbornene-tetrazine chemistry [5], highlighting the need for a strategy that increases the efficiency of amine conversion into a stable species that can easily be rendered reactive. So far only one study has shown a clear purification of monovalent streptavidin (mSA) conju-gation to the surface of a QD [1]. However, that particular method for separating monovalent QDs was found to be tedious and difficult due to its harsh treatment involving heat and centrifugation. Also, the conjugation relies on a reversible attachment of the 6his-tag of a mSA onto a QD surface, which is a non-covalent interaction and liable to dissociation. The ideal purification method would be a chromatography-based separation of constructs that provides a quantitative and easy separation and characterization.

2.1.1 Strategy for Increasing QD-Biomolecule Conjugation Efficiency and Decreasing Non-Specific Interactions

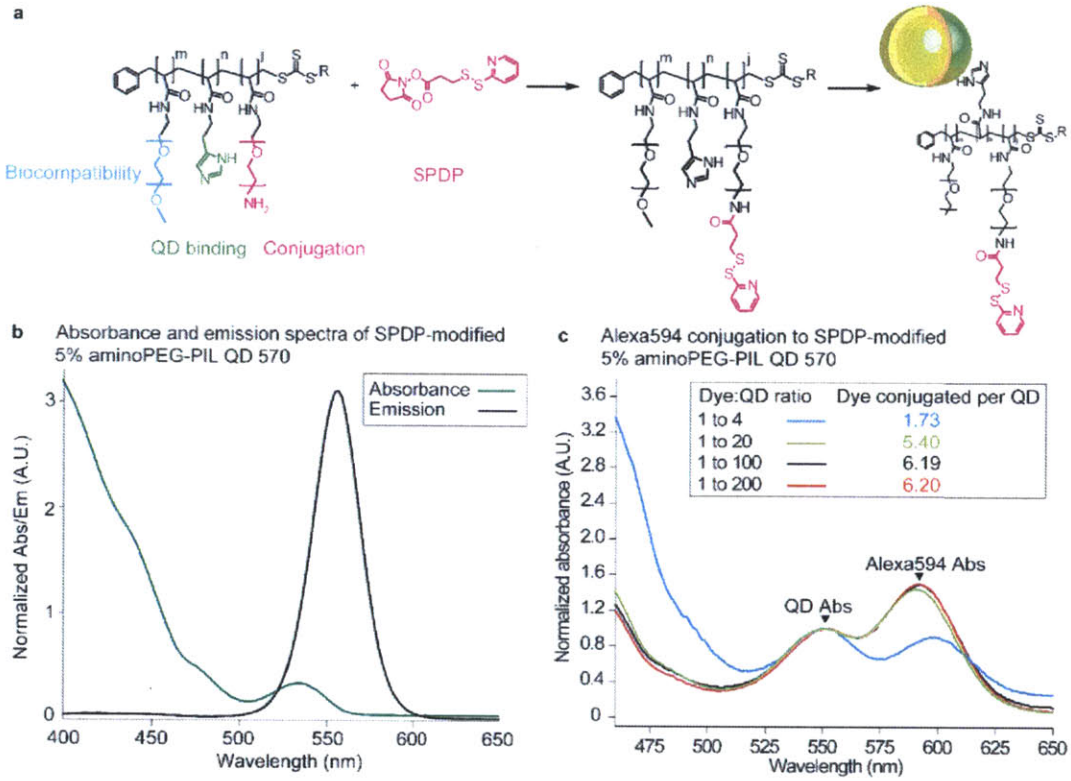

Figure 2-1: **a** Schematic of QD-mSA synthesis. Poly-imidazole ligands (PIL) containing methoxy-poly(ethylene)$_{11}$glycol (PEG_{11}), imidazole, and amine-terminated PEG_8 groups were conjugated to succinimidyl 6-[3(2-pyridyldithiol) propionamido]hexanoate (SPDP) prior to ligand exchange with native hydrophobic ligands on the QD surface. **b** The broad absorbance band and narrow emission of QD570 that has been ligand exchanged with PILs containing SPDP. **c** Verification of the average number of SPDP per QD by saturating with incremental equivalents of maleimide-Alexa 594. (Alexa594 coefficient at 588 nm=96,000 $M^{-1}cm^{-1}$, QD absorption coefficient at 350 nm=1.53 x 10^6 $M^{-1}cm^{-1}$)

The new conjugation protocol introduced in this chapter is a step forward to make small, stable, and monovalent QDs for biological applications. Stable and immediately activable QDs without non-specific binding to biomolecules were prepared by converting the amines on PIL into a protected, reactive group prior to ligand exchange and QD water-solubilization. Briefly, amine-containing PIL was reacted with succin-

imidyl 6-[3(2-pyridyldithiol)propionamido]hexanoate (SPDP) or with the NHS-ester form of biotin, purified, and exchanged with the native hydrophobic ligands on the QD surface (Fig. 2-1a). This new procedure addressed the issue of high non-specific binding and low SA-coupling efficiency because the amines on the PIL were converted to a different chemical group that does not interact with the QD surface. Thus, the percentage of amines per PIL was minimized to 5% of the imidazole and PEG-based monomer units on the PIL (compared to the conventional 25% of monomer units on the PIL) [4]. Such a low number of amines per QD suggests that the non-specific binding could be banished. Meanwhile, the easy and high efficiency of amine conversion will greatly increase the SA-coupling efficiency. Upon conjugation to SMCC-modified SA, the SPDP-modified QDs were found to have minimal non-specific binding, low valency of biomolecules, and high specificity. The biotin-modified QDs could be combined with SA (intended to label POI in a sandwich assay) to result in a population that is just as high-quality. In fact, the biotin-modification of QDs to result in QD-biotin + SA + biotin-POI labeling was chosen to be further optimized (see section 2.1.2) because it precluded the need for any modification of SA.

2.1.2 Strategy for Purifying Different QD-Biomolecules Valencies

The next step towards improving QD-based fluorescent labels is purification of QD-SA into monodisperse samples containing a known valency of SA per QD. As mentioned above, a chromatography-based separation has the potential to be not only quantitative and high-yield, but also much more gentle than previously developed gel-based method [1]. Our experience with size-selective gel chromatography has been that the size differences of 1SA-QD, 2SA-QD, 3SA-QD...etc are not enough to produce separate peaks. The alternative is to generate enough differences in the charge amongst QD-SAs of different valencies. In order to endow 1SA-QD, 2SA-QD, 3SA-QD...etc with different charge, SA was engineered to have a cleavable string of lysines (K). After ion-exchange chromatography, the string of K can be enzymatically cleaved to

result in a QD-SA construct population of known valency. By using a divalent SA composed of two dead subunits (D) and two alive units (A), we can truly achieve a monovalent QD-SA, one where a single QD-SA labels a single POI.

2.2 Results and Discussion: Highly Efficient, Stable Activation of QDs

As expected, the 5% SPDP-QD constructs maintained the broad absorption bandwidth, narrow emissions (Fig. 2-1b) and the compact hydrodynamic diameter of ~10-12 nm. To verify the number of reactive groups on the QDs, SPDP-QDs were deprotected to expose thiol groups and subsequently reacted with maleimide-activated fluorescent dye. The new procedure resulted in SPDP-QDs that that could react with a maximum of ~6 maleimide-dyes (Fig. 2-1c), compared to ~27 by SPDP-QDs prepared using the conventional technique. We believe that the conventional SPDP-QDs most likely has some amines left unreacted. This should have the effect of reducing nonspecific binding, as an abundance of free amines has been shown to aggravate this property [5]. In addition, our use of biotin or protected pyridylthiol group as the QD conjugation handle addressed the issue of stability of an activated QD, allowing optimized, home-made, reactive QDs to be transported across the US. We then made a monovalent streptavidin (mSA) with a cleavable 6-histidine tag in the alive subunit [1]. The original wild type SA subunit was inserted a TEV-protease cleavage sequence (ENLYFQG) before the 6-histidine tag using a QuickChange site-directed mutagenesis kit (Agilent Technologies). Streptavidins with different valencies were made by mixing alive subunits (A) with inactive (dead, D) subunits at a 3:1 ratio. The protein mixture was first passed through a nickel column to remove waste and high valency A4 streptavidin, and then streptavidins with different valencies were purified using an imidazole gradient (Fig. 2-2a). Four peaks were clearly observed on the chromatograph plot, and they represented D4, A1D3, A2D2 and A1D3 respectively. Their valencies were verified using an SDS-PAGE before (Fig. 2-2b) and

after (Fig. 2-2c) denaturing the streptavidins [1]. The binding valencies were further verified on an agarose gel electrophoresis after conjugating with a 58-bp single strand biotin-DNA (Fig. 2-2c). To avoid the interference of 6-his-tag binding to the QD, it was removed using TEV protease. Residual his-tagged mSA was removed by passage over a nickel resin and SDS-PAGE electrophoresis showed the resulting mSA to be free of the his-tag and quite pure (Fig. 2-2d).

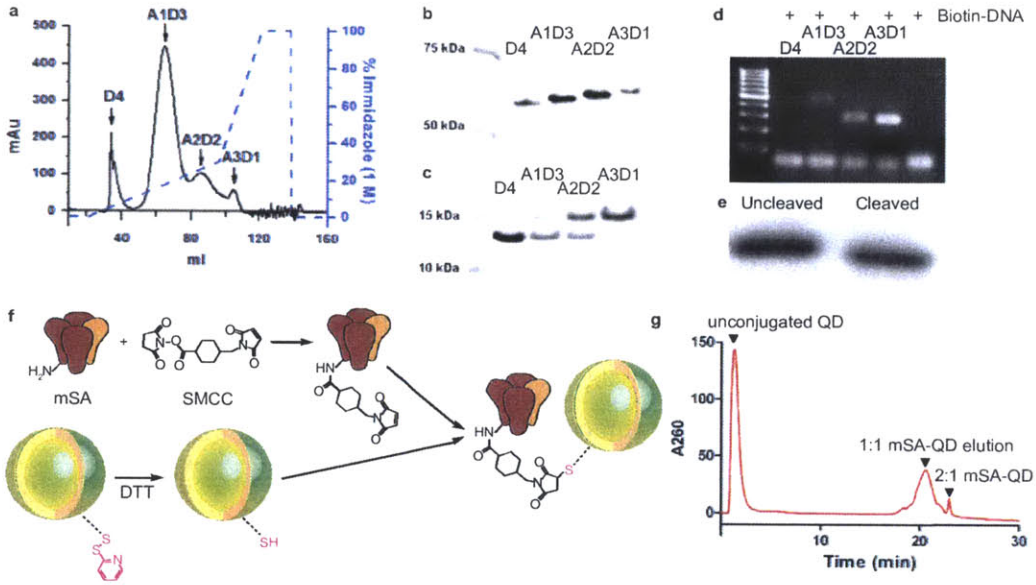

Figure 2-2: Characterization of cleavable monovalent streptavdin (cmSA) and the final labeling construct, mSA-QD. **a** Streptavdin dead subunits (D) and alive subunits with a cleavable 6his-tag (A) were refolded from denaturant in a ratio of 3:1, generating a mixture of streptavidins with five different binding valencies. Pre-purified streptavdin mixture was purified using a gradient FPLC. Four peaks were detected and they are D4, A1D3, A2D2 and A3D1. The imidazole gradient is shown as a dashed blue line. **b-c** SDS-page of purified chimeric streptavidins under nondenaturing (b) and denaturing conditions (c). **d** Streptavidin valency verification using a 58-bp biotin-DNA on a 1% agarose gel. **e** The 6his-tag of purified cmSA (A1D3) was cleaved by the TEV protease and the completion of cleavage was verified by a SDS-page. **f** Schematic showing the mSA and QD conjugation strategy. Thiols on the QD were exposed by reducing pyridyldithiol groups with dithiothreitol and were reacted with maleimide-conjugated mSA. **g** Anion exchange FPLC of the QD-cmSA sample. The peak assignments are tentative.

As illustrated in figure 2-2, the SPDP-handles on the QDs were cleaved using DTT and the his-tag free mSA was activated using sulfo-SMCC. After desalting

twice using with 7KDa Zeba Spin Desalting Columns, the sulfhydryl group on QD reacted with the sulfhydryl-reactive maleimide on mSA to yield specific covalently coupled QD-mSA conjugates. The product was purified on an S200 gel filtration column to re-move unconjugated mSA. After conjugation with 58-bp bio-tin-DNA, the valencies of QD-mSA conjugates were tested with an anion exchange column [7]. The elution peaks tentatively showed that majority of the QDs were not conjugated with mSA (Fig. 2-2). We next tested the functionality of the monovalent QDs. We first stained the biotinylated RBCs [8] with these QDs. The staining was specific and completely blocked by excess small biotin molecules (Fig 3a). The non-specific binding could be regarded as non-existent because the staining pattern of blocked QDs was indistinguishable to that of unstained RBCs. The high specificity was verified using single-molecule microscopy. Binding specificity is critical to many biological applications, in particular to the broad field of single-molecule research which greatly benefits from the unparalleled brightness and photostability of QDs. The presence of PEG groups on the nanoparticle surface improves specificity in general [9],[10], but the specificity of our QDs exceeds that of previous PEG-containing PIL-passivated QDs that has showed negligible non-specific binding [11]. Here, we have banished non-specific binding by minimizing the number of amines to 5% of PIL and by increasing the amine conversion yield.

After demonstrating the specific targeting of these QDs, we further used them for single-molecule experiments. We first attached individual QDs onto a biotin-polylysine coated glass coverslip and visualized single QDs' fluorescence using a 488-nm laser excitation. Individual QDs showed typical blinking behavior (Fig. 2-3b, blue curve), which supported single-QD detection. Meanwhile, we used our QDs to label biotinylated peptide major histocompatibility complexes (pMHC) on the CH27 cell surface at a very low density [12]. We were able to easily identify single molecules on live cell membranes. On an animation pane (video not included in thesis), it is clear that the QDs are blinking, but we found that an intensity trace of single QDs on the cell membrane have smaller variations, possibly due to slight movements across the z-plane due to cell events (Fig. 2-3b, red curve). Here we show an example of tracking a

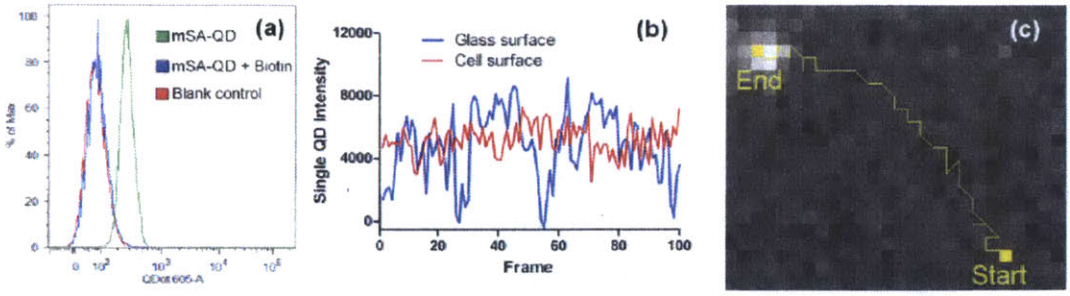

Figure 2-3: Specific cell surface staining and single-molecule tracking using monovalent QDs. **a** Specific staining of monovalent QDs to biotinylated RBCs. The green histogram is the specific staining, and the red and blue histograms are the unstained RBCs control and the blockage of monovalent QD-staining by excess biotin, respectively. **b** Representative intensity time traces of single quantum dots on the surface of coverslip glass (blue) and on the membrane of a CH27 cell (red). Each single QD emission (10 ms exposure) was collected for 100 consecutive frames. **c** Single molecule tracking of a biotinylated molecule on a CH27 cell membrane labeled by a monovalent QD with good spatiotemporal resolution (~30 nm, ~50 ms). The single QD emission (10 ms exposure) was collected with a frame rate of 50 ms/f for 71 consecutive frames.

single pMHC on the CH27 cell surface (Fig. 2-3c) with good spatiotemporal resolution (~30 nm and ~50 ms). The temporal resolution of QD imaging can easily reach ~1 ms using a laser with a higher power (Huang et.al, unpublished data). Therefore, the stable, small, and monovalent QDs demonstrated here can be used to label and track a wide variety of biomolecules with minimal perturbation and with excellent brightness and stability.

2.3 Experimental Details

Materials and equipment All chemicals were obtained from Sigma Aldrich or Thermo Fisher Scientific and used as received unless indicated otherwise. Air sensitive materials were handled in an Omni-Lab VAC glovebox under dry nitrogen atmosphere with oxygen levels <0.2ppm. All solvents were Spectroscopic or reagent. Aromatic ring-bearing compounds were visualized on TLC using a hand-held UV lamp and $KMnO_4$. Amine-bearing compounds were visualized on TLC using a Ninhydrin stain. Flash column chromatography was performed on a Teledyne Isco Combi

Flash Companion. Size selective chromatography was performed on GE Healthcare PD-10 columns.

QD and ligand synthesis CdSe/CdS coreshell quantum dots and Polymeric imidazole ligand (PIL) were synthesized according to previous reports [4]. The PILs used throughout this work consisted of 50% methoxy-terminated poly(ethyleneglycol) sidechains (mPEG), 5% amine-terminated oligo(ethyleneglycol) side chains (AminoPEG), and 45% histamine side chains.

PIL activation with (1) SPDP (2) biotin 50% mPEG/5% AminoPEG/45% histamine-PILs were stirred with SPDP or with NHS-biotin in DMF in RT overnight. NHS by-products were removed by sequential addition of solvent, centrifugation, and removal of pellet using methanol and chloroform. The activated PIL was then purified by size-selective chromatography (Biobeads) in THF solution.

QD ligand exchange with activated PIL for water-solubilization The native hydrophobic trioctyl phosphine and trioctyl phosphine oxide NC ligands were displaced by PIL following a previously described procedure. Briefly, CdSe/CdS coreshell quantum dots in trioctylphosphine/octadecene were precipitated with acetone and methanol. After centrifugation, the supernatant was discarded and the pellet redispersed in chloroform. This solution was added to PIL in chloroform under stirring. After 10 minutes, methanol was added and stirring continued for a further 30 minutes. After this time, the solution was diluted with an ethanol/chloroform mixture (1 : 1 v/v) and precipitation induced by the addition of hexane. The nanoparticles were collected by centrifugation, and the supernatant discarded. The resulting product was dissolved in water, filtered through a 0.2 μm HT Tuffryn membrane and dialyzed against PBS, pH 7.4 buffer. The concentration of the recovered solution was determined by UV-Vis spectroscopy.

SA design and purification QuickChange method was used to insert a TEV cleavage sequence (ENLYFQG) preceding the 6-His tag of the original alive strep-

tavdin using a two-stage PCR protocol [18]. The PCR products were transected into a XL10-Gold ultracompetent cells by following the manufacture instructions. Briefly, 100 μl of cells were thawed and added with 4 μl β-ME mix and 2 ml PCR product in a 14-ml BD Falcon polypropylene round-bottom tube. The tube was heat-pulsed in a 42 °C water bath for 30 seconds, incubated on ice for 2 minutes, added with 0.9 ml preheated (42 °C) NZY+ broth and incubate the tubes at 37 °C for 1 hour with shaking at 250 rpm. 200 μl of the transformation mixture was spread on a LB agar Ampicillin-plate and incubated at 37 °C overnight. Six single clones were picked and culture in LB overnight. The cultured cells were spun down and collected. The DNA was purified using a QIAprep Spin Miniprep Kit. Purified DNA was sequenced and confirmed the correct insertion of TEV cleavage sequences. Here is the amino acid sequence of the alive subunit: AEAGITGTWYNQLGSTFIVTAGADGALTGTYE SAVGNAESRYVLTGRYDSAPATDGSGTALGWTVAWKNNYRNAHSATTWSG QYVGGAEARINTQWLLTSGTTEANAWKSTLVGHDTFTKVKPSAASENLYFQ GHHHHHH. We followed the protocol of Alice ting et al. to express and refold the strepavdins [14], and we used a imidazole gradient protocol to purify the chimeric streptavidins as described in the main text.

SA activation with SMCC and conjugation onto QD We dissolved 2 mg Sulfo-SMCC into 200 μl fresh water purified at by a milli-Q integral water purification system. We then added 50 μl Sulfo-SMCC into 100 μl mSA (0.5 mg/ml). We incubated reaction mixture for 30 minutes at room temperature and removed excess crosslinker with desalting columns equilibrated with PBS/1mM EDTA by desalting twice. Meanwhile, SPDP-QDs were activated using 50 mM DTT for 30 minutes in room temperature and desalted twice to remove excess DTT. We then mixed the reactive forms of QDs and mSA with a ratio of 1:1 or 1:2 and incubated overnight in 4 °C cold room. The un-conjugated mSA was removed by size exclusion chromatography on S200 resin.

Flow cytometry to test QD specific labeling Mouse red blood cells (RBCs) were isolated from mouse whole blood. In brief, 1 ml of whole blood was collected using a sterile tube containing EDTA, then carefully layered over 1 ml of Histopaque (Sigma-Aldrich), centrifuged and washed 5 times with PBS. Isolated RBCs were biotinylated using Biotin-X-NHS (Calbiochem) according to the manufacturers instruction. In brief, RBCs were incubated with titrated Biotin-X-NHS at pH 7.2 for 30 min at room temperature, and washed five times with PBS/1% BSA to remove Biotin-X-NHS and stop the reaction. Biotinylated RBCs were stained with 20 nM QD-mSA conjugates in the presence or absence of 2 mM free biotin molecules. After three times wash, the RBCs were analyzed by an LSR-II flow cytometer (BD) at Stanford University Shared FACS Facility.

Cell culture and single-cell imaging The B-cell lymphoma cell line CH27 cells were maintained in complete medium (RPMI 1640 medium, 10% fetal calf serum, 2 mM L-glutamine, 50 μM β-mercaptoethanol and penicillin/streptomycin). The biotin-MCC (88103) peptide was custom synthesized and purified by Elim Biopharm. The peptide consisted of a biotin flexible linker and a peptide sequence, biotinAHX-SGGGSGGGANERADLIAYLKQATK. Underlined residues were synthesized as d-stereoisomers to avoid possible proteolytic cleavage of residues extending outside the MHC binding groove. This extended uncleavable flexible linker provided the space and flexibility for following fluorescent labeling.

APCs were pulsed with 50 μM of biotin-MCC peptides. The peptide pulsed APCs were washed five times using cold PBS supplemented with 2% BSA and 0.05% NaN_3 (to prevent any possible internalization or export of MHC), resuspended in 1 mL the same medium and labeled with QD-mSA conjugates at 4 °C for 30 minutes. After 5 times wash, the cells were imaged with a Zeiss microscopy imaging system equipped with an Axio Observer Microscope body, a Zeiss 100 oil objective (numerical aperture 1.45), a nanofocusing z-drive, and an Andors iXon 897 back-illuminated electron-multiplying charge-coupled device (EMCCD) that has single photon detection capability combined with >90% quantum efficiency (Andor Technology), a mo-

torized x-y stage and a 488-nm line laser. For the single-cell and single-molecule imaging, we acquired a differential interference contrast (DIC) exposure and a QD fluorescent image excited by the 488-nm line laser excitation and collected through a single band 586/20 mission filter (Semrock).

Single-QD imaging We tested single-QD fluorescent signals on glass cover slips and on the APC surface. QD-mSA were either bound onto the surface of a biotinylated poly-lysine coated coverslip or conjugated with the biotinylated peptides loaded onto a CH27 cell surface. With the 488-nm line laser excitation and the highly sensitive Andor EMCCD, we readily detected single QD signals with high signal-to-noise ratio. All the images were taken with 10 ms exposure time in the stream model of the CCD camera.

Bibliography

[1] Lippincott-Schwartz, J.; Patterson, G. H. *Science* **2003**, 300, 87-91.

[2] Resch-Genger, U.; Grabolle, M.; Cavaliere-Jaricot, S.; Nitschke, R.; Nann, T. *Nature Methods* **2008**, 5, 763-775.

[3] Medintz, I. L.; Uyeda, H. T.; Goldman, E. R.; Mattoussi, H. *Nature Materials* **2005**, 4, 435-446.

[4] Liu, W. H.; Greytak, A. B.; Lee, J.; Wong, C. R.; Park, J.; Marshall, L. F.; Jiang, W.; Curtin, P. N.; Ting, A. Y.; Nocera, D. G.; Fukumura, D.; Jain, R. K.; Bawendi, M. G. *Journal of the American Chemical Society* **2010**, 132, 472-483.

[5] Devaraj, N. K.; Weissleder, R.; Hilderbrand, S. A. *Bioconjugate Chemistry* **2008**, 19, 2297-2299.

[6] Howarth, M.; Chinnapen, D. J. F.; Gerrow, K.; Dorrestein, P. C.; Grandy, M. R.; Kelleher, N. L.; El-Husseini, A.; Ting, A. Y. *Nature Methods* **2006**, 3, 267-273.

[7] Claridge, S. A.; Liang, H. Y. W.; Basu, S. R.; Frechet, J. M. J.; Alivisatos, A. P. *Nano Letters* **2008**, 8, 1202-1206.

[8] Huang, J.; Zarnitsyna, V. I.; Liu, B. Y.; Edwards, L. J.; Jiang, N.; Evavold, B. D.; Zhu, C. *Nature* **2010**, 464, 932-U156.

[9] Bentzen, E. L.; Tomlinson, I. D.; Mason, J.; Gresch, P.; Warnement, M. R.; Wright, D.; Sanders-Bush, E.; Blakely, R.; Rosenthal, S. J. *Bioconjugate Chemistry* **2005**, 16, 1488-1494.

[10] Mei, B. C.; Susumu, K.; Medintz, I. L.; Delehanty, J. B.; Mountziaris, T. J.; Mattoussi, H. *Journal of Materials Chemistry* **2008**, 18, 4949-4958.

[11] Liu, W.; Howarth, M.; Greytak, A. B.; Zheng, Y.; Nocera, D. G.; Ting, A. Y.; Bawendi, M. G. *Journal of the American Chemical Society* **2008**, 130, 1274-1284.

[12] Irvine, D. J.; Purbhoo, M. A.; Krogsgaard, M.; Davis, M. M. *Nature* **2002**, 419, 845-849.

[13] Wang, W.; Malcolm, B. A. *Biotechniques* **1999**, 26, 680-2.

[14] Howarth, M.; Liu, W. H.; Puthenveetil, S.; Zheng, Y.; Marshall, L. F.; Schmidt, M. M.; Wittrup, K. D.; Bawendi, M. G.; Ting, A. Y. *Nature Methods* **2008**, 5, 397-399.

Chapter 3

QD-based Sensors as a Paradigm

3.1 The Need for Fluorescent, *in-situ* Sensors for Biological Applications

Recent advances in disease therapy has greatly benefited from modern diagnostic methods. The ability to monitor the progress of disease or the effects of therapy enables better prognosis or choice of medication; the ability to monitor in real-time, with higher sensitivity, and through less invasive procedures, should help identify treatment resistance or lack of clinical benefit, ultimately leading to higher patient survival rates [1]. Existing diagnostics include ELISA and MRI scans, but most cancers are diagnosed by biopsy. Depending on the size and location of the cancer, biopsies may be painful and expensive. The conventional diagnostics rely on open biopsy to determine malignancy and grade. Due to the operating room costs, potential morbidity, associated time, insufficient tissue sample, and for incisive biopsy, complications involving incisions, diagnostic biopsies could be much improved [2]. *In-vivo* imaging addresses many of these concerns. Using IR imaging, tissue imaging could potentially be an incredibly powerful complement to the newer CT or MRI methods that provide non-invasive, continuous, real-time, large-area, and sensitive measurements. However, in order to harness the advantages of fluorescence microscopy in the biological environment, there is a need for powerful, smart fluorescent probes that image and

identify simultaneously.

3.1.1 Criteria for a Fluorescent Sensor for the Biological Microenvironment

A biological sensor must have the following criteria:

- Non-toxicity and biocompatibility: Biosensors should minimally perturb the in vivo environment and should not be affected by the bioenvironment. The fluorescent probe should not interact non-specifically with other biomolecules in its environment, not only because biofouling could adversely affect the sensor performance, but also because there could be immune responses or trafficking issues *in vivo*. Research has indicated that PEO/PEG groups increase biocompatibility [3].

- Specificity: Specificity, or selectivity, is largely dependent on the molecular recognition element. Unfortunately, other factors such as sensitivity and sensor complexity often have to be sacrificed in order to increase specificity. For example, sensors based on dehydrogenase activities may be quite specific, but typically require co-factors, posing restrictions on dehydrogenase-based biosensors.

- Sensitivity: Sensitivity is dependent on the technique, fluorescent probe, and the molecular recognition element. Sensors that rely on enzymes or biomolecules with low activity and stability may not be sensitive enough, but such challenges may be overcome by using techniques\probes that have inherently high signal-to-noise ratio.

- Spatial and temporal resolution: Theoretically, advanced fluorescence microscopy methods such as multi-photon and confocal imaging may decrease spatial resolution to the diffraction limit. The temporal resolution, dependent on the microscopy technique but also on the excitation and relaxation time of the flu-

orescent probe, is particularly important for biosensors that measure neuronal response to therapeutics.

- Chemical and photostability: For long-term imaging, e.g., delineating the boundary of tumor and normal tissue in the operating room, fluorescence should not fade. Photobleaching therefore could be a serious problem for conventional organic dyes.

- Calibration: Fluorescent sensing within living environments must ultimately address confounding factors such as variations in probe concentration, excitation intensity, and collection efficiency [16],[20].

Previous *in vivo* biosensors have included microelectrode-based sensors [5], implantable microarrays [4], and molecular biosensors. Yet to be as widely explored is the concept of exploiting mechanically active components to create an engineered nanoconstruct whose movements modulate its own properties [9]. Such a construct could, for example, report on its microenvironment by modulating the optical properties of NCs through a nanomechanical process that responds only to a specific analyte. Several intrinsic properties make NC fluorophores apt tools for advanced imaging applications mentioned above such as intravital multi-photon microscopy [8],[10],[11]. Attributes wuch as narrow and tunable emission spectra, high quantum yields, broad absorption profiles, high photostability, and large single and multi-photon cross sections provide strong motivation for finding ways to incorporate NCs into fluorescent sensors that fulfill the criteria listed above. One of the most promising concepts for constructing NC sensors is to attach a second chromophore (such as an organic dye or a transition metal complex) that can act as a fluorescence resonant energy transfer (FRET) partner with the NC [12]. While NC-based constructs have shown detection abilities by employing cleavage [13],[14], displacement [15],[16] or chemical modification [17],[18] by an analyte to irreversibly modulate the FRET interaction, continuous monitoring of analyte levels requires a reversible response to analyte concentration. Most of the reported NC-based sensors have thus been based on a strategy that necessitates analyte-sensitive dyes, resulting in several shortcomings including the limited

variety of available analyte-responsive dyes and difficulty of use in biological environments [19],[20],[21]. In addition, to address the calibration criteria above, NC sensors must be self-referencing, where a ratio of fluorescence intensities reports on the microenvironment. In this project, a chemically insensitive NCmolecule FRET pair is connected through a linker that undergoes a reversible conformational change upon binding to the analyte (Fig. 3-1a). As energy-transfer interactions are extremely sensitive to distance, conformational changes in the linker lead to a substantial change in optical signal. Monitoring the emission from both fluorophores therefore provides a sensitive, ratiometric response that can be used to track analyte concentrations within individual intracellular vesicles.

3.2 Results and Discussion: A QD-based pH Sensor

3.2.1 QD-based pH Sensor Design

The NC-based sensor synthesized during this project consists of a linker whose conformation is sensitive to such pH changes in living environments. This linker is based on the phenomenon that certain cytosine-rich oligonucleotide sequences are known to undergo folding or unfolding in response to changes in pH, depending on the protonation state of the cytosine imino group [22]. Recently, a ratiometric pH sensor was created by appending two molecular fluorophores to one such sequence, allowing pH changes in the endosomes of haemocytes to be monitored [23]. To create a NC-based sensor in which a reversible conformational change is transduced into an optical response, a simpler pH-responsive oligonucleotide was selected (Fig. 3-1c). This sequence is capable of cycling between duplex and CT-motif triplex structures with an effective pK_a aimed at greatest sensitivity in mildly acidic biological environments [24]. The relatively rigid DNA adduct helps to ensure that the two ends of the switch are held far apart in the unfolded state. Protonation of cytosine imino groups in the single-stranded region results in folding to allow Hoogsteen triplet base-

pairing interactions in the major groove of the duplex. This conformational change dramatically alters the distance between the termini of the DNA adduct (Fig. 3-1c). In order to build the NC-based pH sensor, 5(6)-carboxy-X-rhodamine (Rox) a pH insensitive fluorophore was installed at the 3 overhang end of the 35-mer (Fig. 3-1c). At the opposite end of the construct, a thiol at the 3 terminus of the 16-mer acted as a handle for attachment to polymer-coated NCs. We have previously demonstrated compact, biocompatible and bright NCs based on polymeric imidazole ligands (PILs) (Fig. 3-1b) [16]. Water-soluble CdSe/CdS coreshell NCs, emitting at 560 nm, were prepared using PIL 1. Activation of the primary amines with the heterobifunctional linker sulfosuccinimidyl-4-(N-maleimidomethyl)cyclohexane-1-carboxylate (sulfo-SMCC) then allowed covalent attachment of the thiol on the hybridized double-stranded oligonucleotide (see appendix for details). Successful conjugation of the oligonucleotide to the nanoparticles was confirmed by the UV-Vis absorption spectrum, featuring both the inorganic NC and organic dye peaks. A linear fit of this spectrum to reference NC and Roxoligonucleotide spectra gave an average valence of 3.6 Roxoligonucleotide units per NC.

3.2.2 pH Sensor Characterization in Solution

When placed in phosphate buffers of varying pH and excited at 460 nm, the construct exhibits a time-invariant emission, comprising two features at wavelengths corresponding to the NC (λ_{PLmax} = 560 nm) and Rox (λ_{PLmax} = 610 nm) components (Fig. 3-2a). As Rox absorbs minimally at 460 nm, this indicates excitation through energy transfer from the NC. On varying pH from 8.0 to 6.1, a dramatic change in the relative intensity of these two features is observed (Fig. 3-2). At high pH values, strong emission from the NC and poor FRET efficiency to Rox is observed, consistent with the unfolded oligonucleotide switch holding the donor and acceptor far apart. As pH is lowered, NC emission becomes increasingly quenched, with concomitant enhancement of emission from the Rox. This is consistent with increasing FRET efficiency from the NC to Rox as the folded triplex conformation of the oligonucleotide brings the NC energy donor and Rox energy acceptor closer. A practical parameter

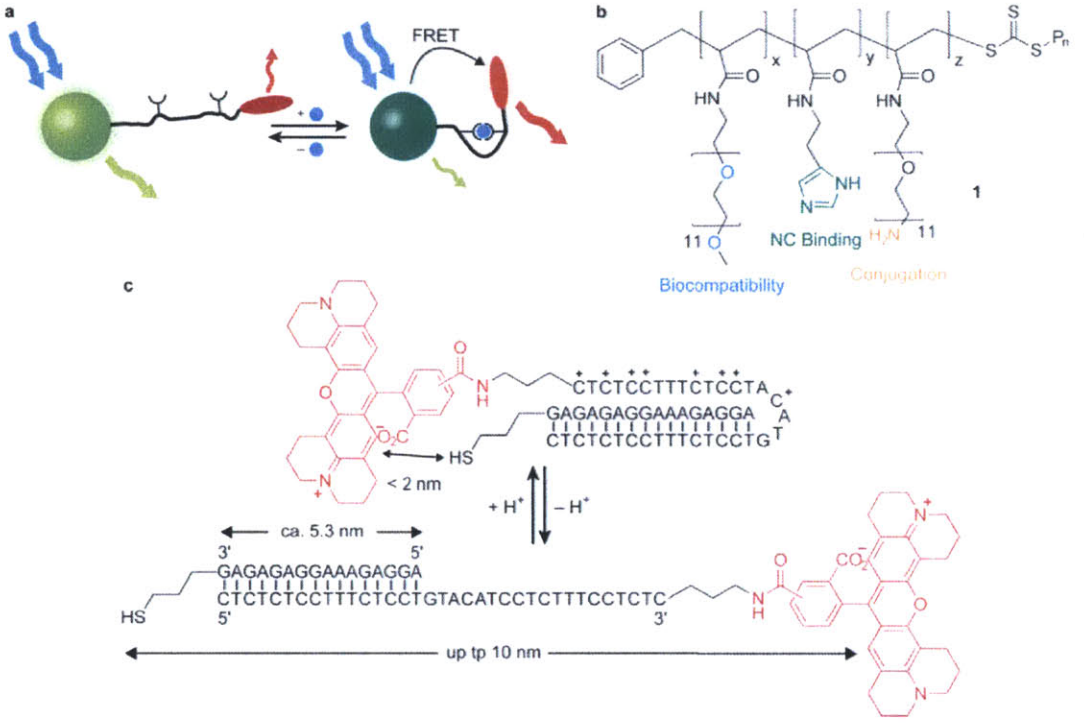

Figure 3-1: Sensor design and constituent parts. **a**, Schematic illustration of sensor design wherein a fluorescent NC (green) is conjugated to one or several molecular fluorophores (red) through an analyte-sensitive linker. Binding of a specific analyte (blue) to the linker triggers a conformational change that alters the donoracceptor distance, hence changing the FRET efficiency and therefore eliciting a wavelength ratiometric optical response. **b**, Chemical structure of PIL. Monomer units were arranged randomly, ratio x:y:z was 1 : 2 : 1, and typically x+y+z = n $\sim$ 16 (i.e., an average of 32 monomer units per chain). **c**, pH-Responsive oligonucleotide triplexduplex conformational switch, bearing carboxy-X-rhodamine and thiol functionalities. Not drawn to scale.

for expressing sensor response is the proportion of green channel emission (using 590 nm as a cutoff) compared to the total integrated emission. A plot of this ratio shows a sigmoidal response (Fig. 3-2b, black squares), with maximum sensitivity around pH 7.0, in line with the characteristics of the oligonucleotide conformational switch [24]. This pH range for conformational switching is ideal for imaging mildly acidified biological microenvironments. The sensor response was found to be robust to changes in both temperature and in electrolyte content (Fig. 3-2c), it was reproducible across several samples and the construct could be recovered, stored and re-used with no adverse effects (see Appendix). Furthermore, a control construct with Rox dyes coupled directly to amino-PIL coated NCs with no oligonucleotide linker showed no variation in the ratio of emission across the same pH range (Fig. 3-2b, blue circles).

A deeper understanding of the underlying chemomechanical and photophysical processes can be gained by examining the Fórster model, which describes well the efficiency of energy transfer from a NC to an acceptor conjugated to it. When multiple acceptors are conjugated to each NC, the ensemble FRET response can be reproduced by assuming a Poisson distribution of coupling stoichiometries. The equations for these calculations are presented in the supplementary information. Comparing a set of modeled FRET efficiencies to the experimentally observed efficiencies (Fig. 3-2d) at low and high pH, we can infer that the donoracceptor separations in the all-folded (A) and all-unfolded (B) states are 6.3 nm and 9.4 nm, respectively (Fig. B-1). These values are consistent with the physical dimensions of the sensor construct measured by dynamic light scattering (DLS) measurements (Fig. 3-2e). The hydrodynamic radius of the PIL-coated NCs before conjugation of the DNA was measured as 6.1 nm, suggesting that in the folded state the Rox dye is located as close to the NC as possible, without penetrating the polymer coating. The fully assembled sensor displays a hydrodynamic radius of 9.4 nm at all pH values (Fig. 3-3). These results together suggest that the size of the nanoconstruct is defined by the extent of the double-stranded DNA region, and in the unfolded state, the single-stranded component does not extend into solution beyond the solvation shell.

The folding and unfolding motion of the oligonucleotide is mediated by principles

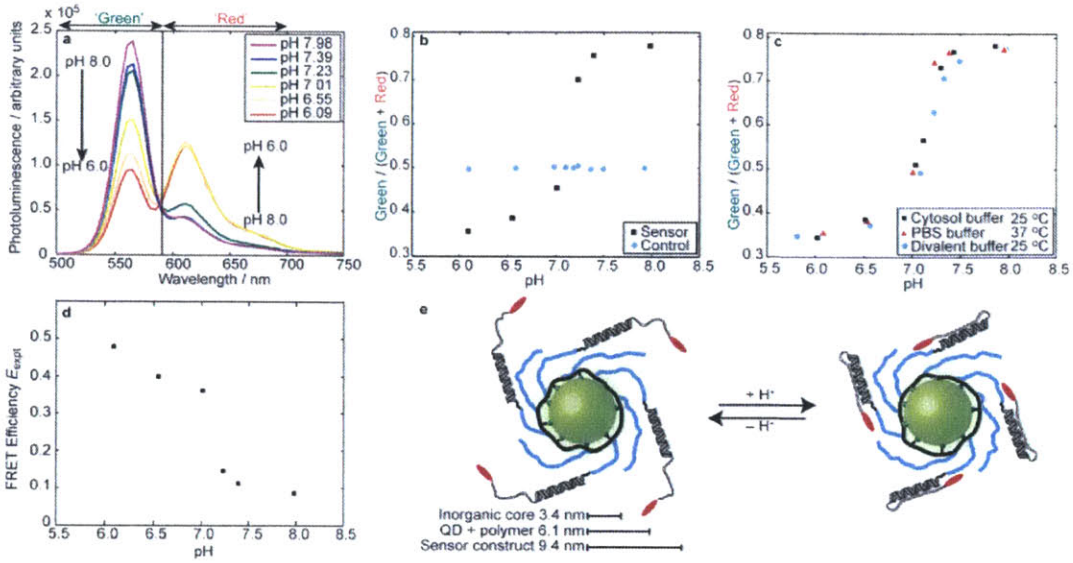

Figure 3-2: Spectroscopic characterization of the sensor. **a**, Sensor photoluminescence spectra on excitation at 460 nm in PBS buffers with differing pH values at 25 °C. Solid black line at 590 nm indicates cutoff wavelength for integration of intensities in green and red channels. Spectra were corrected for variation in concentration using absorbance measurement at excitation wavelength. **b**, Proportion of total emission intensity in green channel (as defined in a) as pH is varied at 25 °C for the sensor (black squares) and a control NCRox construct that lacks the oligonucleotide switch. **c**, Sensor performance under varying environmental conditions. PBS (phosphate buffered saline): (10 mM phosphate, 137 mM Na^+, 2.7mM K^+); Cytosol buffer: 10 mM phosphate, 139 mM K^+, 12 mM Na^+; Divalent buffer: 12 mM phosphate, 137 mM NaCl, 2.7 mM KCl, 0.9 mM Ca^{2+}, 0.5 mM Mg^{2+}. **d**, Efficiency of energy transfer from NC to Rox components with varying pH. **e**, Cartoon representation of sensor construct and operation, indicating inorganic core radius as determined by TEM and hydrodynamic radii of unfunctionalized and functionalized water-soluble NC constructs, as determined by DLS.

Sample	r / nm			<r> / nm
	Measurement 1	Measurement 2	Measurement 3	
NC–PIL 1	6.2	6.1	6.1	6.1
Control (no DNA linker)	7.6	7.7	7.6	7.6
Sensor pH 6.0	9.3	9.6	9.5	9.5
Sensor pH 7.9	9.5	9.3	9.3	9.4

Figure 3-3: Hydrodynamic radii results from DLS analysis of sensor construct, control construct and unfunctionalized water-soluble NCs.

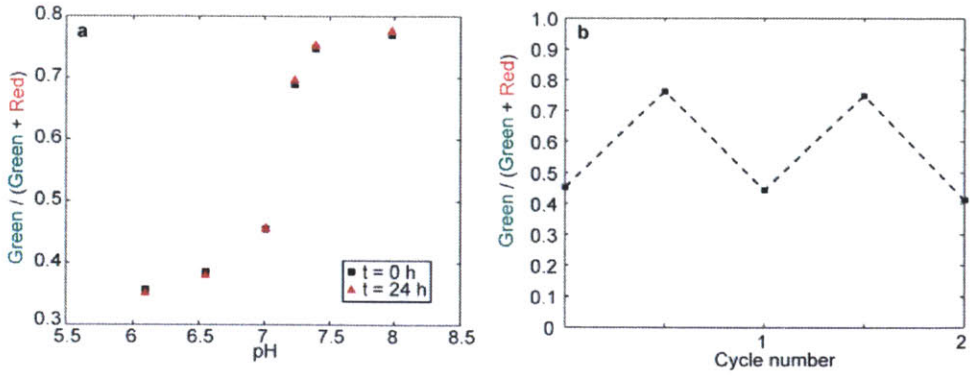

Figure 3-4: **a**, Sensor and control construct PL intensity ratios in green and red channels (cutoff at 590 nm) upon re-dilution into buffers of differing pH, before and after 24 h in pH 7.4 storage buffer. **b**, Sensor response on cycling between acidic and basic buffers by repeated dialysis.

of equilibrium. This means that the sensor response is reversible; indeed, sensor response on cycling between acidic and basic buffers by repeated dialysis shows the response is fully recapitulated on recovering samples from buffers at all pH values shown, returning to a storage buffer at pH 7.4 by dialysis, storage for 24 h, then re-dilution into buffers of differing pH values (Fig. 3-4a). Finally, the emission ratio remained reproducible on alternately exchanging the buffer of one sample of the construct into acidic and basic conditions (Fig. 3-4b).

3.2.3 Measurement of Cellular Endosomal pH *in-vitro*

Robust maintenance of the sensor response under a variety of environmental conditions *in vitro* gives confidence that the design can be applied to image pH variation in living systems. As a proof of concept, we probed the pH of endosomes in human adenocarcinoma cells. It is well known that during endosome maturation, there is a significant pH drop from early endosomes to the late endosomes through action of H^+-ATPases [26]. It has remained challenging however to probe live cell endosome pH values and track the acidification of endosomes over time to develop a complete understanding of this dynamic process. In order to calibrate the sensor response to pH on a biological imaging setup, the construct was imaged in buffers of varying pH

under a confocal microscope. The sample was excited at 488 nm and the image acquired simultaneously in the green NC channel (560-580 nm) and the red Rox channel (590-620 nm). The proportion of green channel intensity as a fraction of the total intensity at different pH values is shown in Figure 3-5a. Although absolute intensities are affected by changing excitation wavelength and green and red channel widths, the power of the ratiometric approach is that the sigmoidal sensor response is maintained (Fig. 3-5a, black squares). The control construct, which lacks the oligonucleotide conformational switch, shows no such variation in PL response with pH. The proportion of QD fluorescence for the control construct (Fig. 3-5a, blue circles) is lower than that of the folded form of the pH sensor because there are fewer Rox units per control construct.

The sensor constructs were then endocytosed into HeLa cells by incubation at 37 °C for 10 minutes. Following rinsing to remove excess sensor, incubation at 37 °C was continued for $0, 10, 20$ and 30 minutes prior to imaging on a confocal setup. Qualitatively, punctate staining characteristic of endosomes was apparent in all healthy cells examined, with these features closer towards the center of each cell at later time points. The images were processed to calculate the average proportion of green channel fluorescence to the total fluorescence for each identifiable endosomal structure, as illustrated in the example shown in Figure 3-5b. Multiple cells at each time point were analyzed. The ratio values (Figure 3-5c) show a clear decrease with increasing time, consistent with progressive acidification of the endosomes. No such variation was observed upon incubation of cells with the control construct lacking the oligonucleotide conformational switch (Figure 3-6). Comparing the ratio values with those from the calibration step (Figure 3-5a) reveals an average drop in pH from >7.4 to <6.9 over the time course of the experiment, with significant numbers of vesicles showing pH values of ~ 6.0 by the last time point recorded.

When control constructs are delivered, the ratio values do not show any significant difference amongst different incubation times (Fig. 3-6).

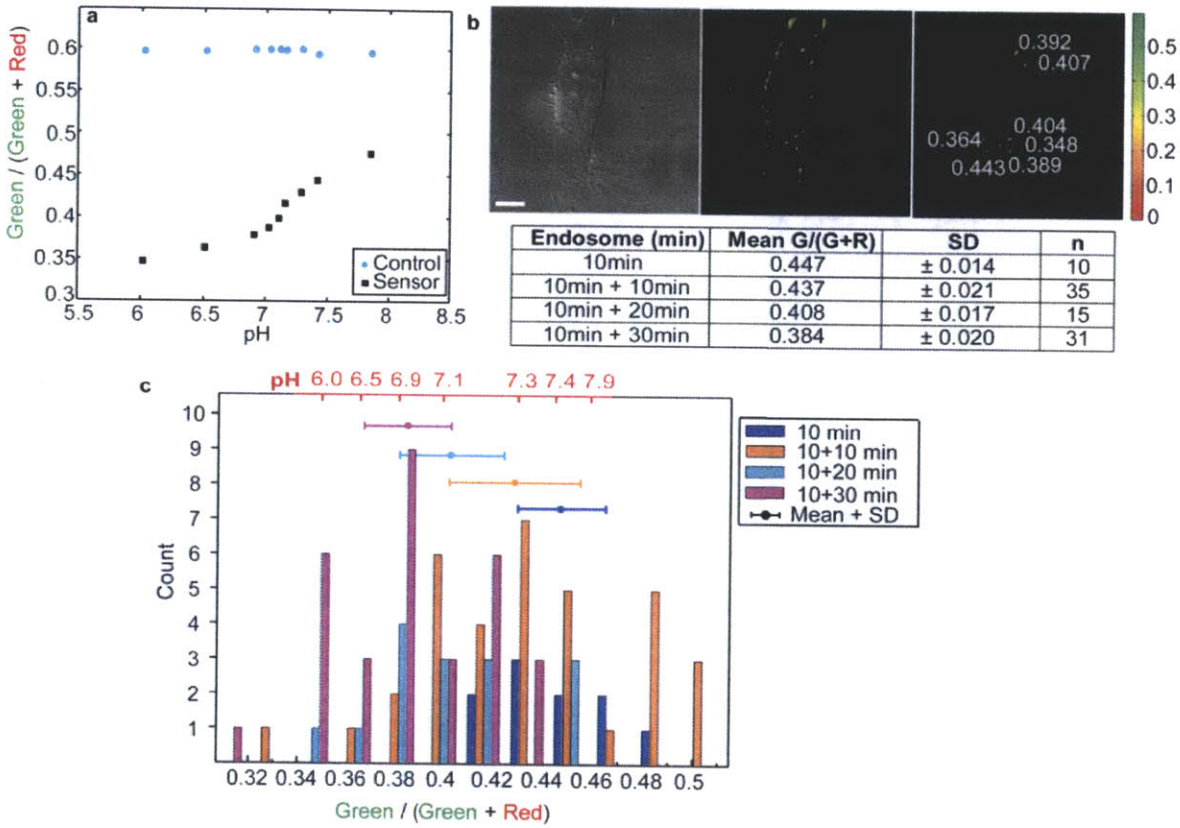

Endosome (min)	Mean G/(G+R)	SD	n
10min	0.447	± 0.014	10
10min + 10min	0.437	± 0.021	35
10min + 20min	0.408	± 0.017	15
10min + 30min	0.384	± 0.020	31

Figure 3-5: Measurement of endosomal pH in live cells. **a**, Proportion of total emission in green channel on confocal imaging of the sensor (black squares) and the control (blue circles) constructs in phosphate buffers with varying pH. **b**, Representative raw image, false-colored ratiomap, and picked endosomes of a cell from the 10 min + 20 minute group. **c**, Emission ratios for endosomes found in cells incubated with the sensor construct for a 10 minute pulse period followed by 0, 10 minute, 20 minute, and 30 minute chase periods (endosome n = 10, 35, 15, 31 respectively). (Scale bar = 10μm)

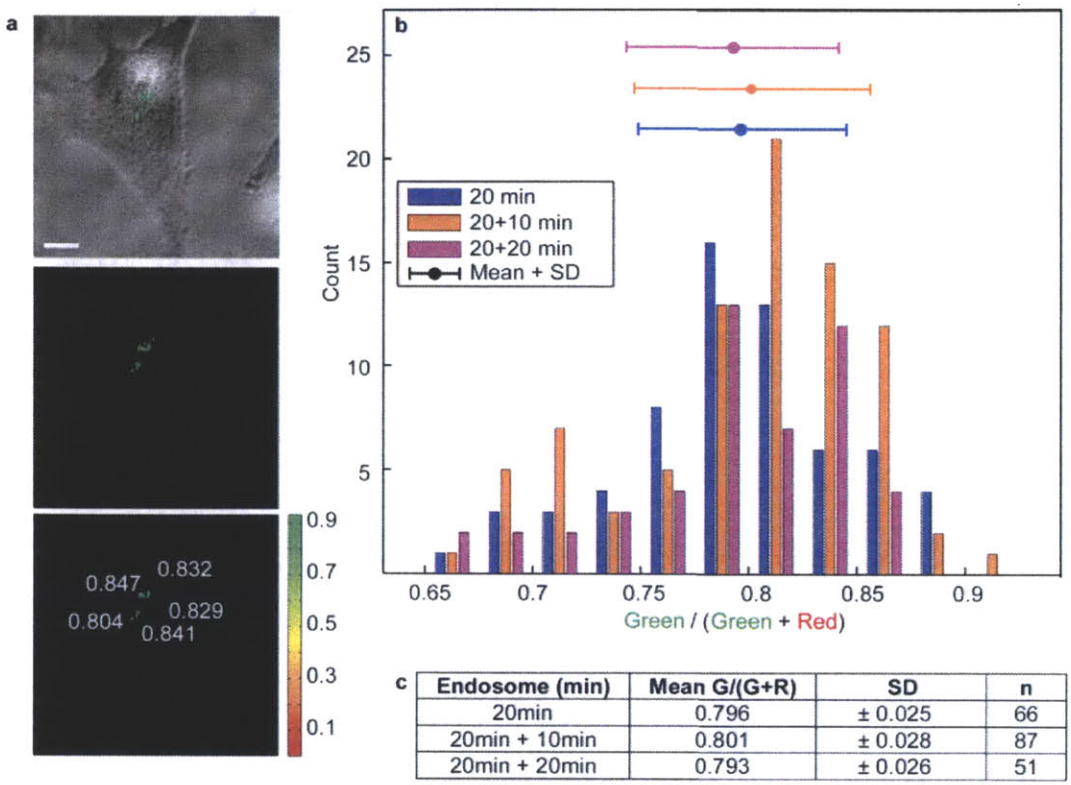

c

Endosome (min)	Mean G/(G+R)	SD	n
20min	0.796	± 0.025	66
20min + 10min	0.801	± 0.028	87
20min + 20min	0.793	± 0.026	51

Figure 3-6: Ratios of green and red channel intensities from endosomes in cells treated with control construct. Cells were labeled with the control construct with a 20 minute incubation period followed by 0, 10 minute, and 20 minute chase periods (endosome n = 66, 87, 51 respectively). **a**, A representative raw image, false-colored ratiomap, and picked endosomes of a cell from the 20 minute chase group. **b**, Histogram of endosomal ratios. For the control experiments, the z-focus during the cell experiment does not correspond to the z-focus in buffer. **c**, Emission ratios for endosomes found in cells incubated with the control construct. (Scale bar = 10μm)

3.3 Conclusion

The strategy reported here represents a novel and flexible approach to designing NC sensors. By transducing a mechanical property rather than an optical property, we separate the sensing and signaling functions. Such sensors are no longer constrained to operate within the parameters defined by available analyte-sensitive fluorophores. The conjugation chemistries employed here are universal and so any FRET pair of fluorophores can be employed, including the attractive possibility of creating all-NC ratiometric sensors. Likewise, the conformational switch may be optimized per analyte and concentration range without necessitating a change to the fluorescent components or imaging setup. Oligonucleotide conformational switches triggered by other simple stimuli have been characterized [22], along with DNA-based aptamers that exhibit a conformational change on binding non-nucleotide targets [27], while the field of supramolecular chemistry has provided a host of synthetic receptors that undergo a conformational change on guest binding [28]. The sensor design reported here demonstrates that any of these systems may be harnessed in a NCnanomachine sensor. The application of NCs to study complex living systems has the potential to yield molecular level information with unprecedented spatial resolution together with the ability to track changes over long periods of time. Using molecular machines to control the optical properties of NC constructs presents a new opportunity for creating sensors that realize this goal. Achieving control over nanoconstruct stoichiometry is a key challenge that now must be addressed. While applications that involve imaging large numbers of NC fluorophores (such as mapping the tumor environment) are not limited by the distribution of NC valencies, NC constructs with precisely defined stoichiometry would allow quantitative measurement even for applications involving only a few NC-sensors.

3.4 Experimental Details

General Materials and Methods Unless stated otherwise, all reagents were purchased from commercial sources and used without further purification. Ultrapure water from a Barnstead Nanopure system with D3750 0.2μm filter (Thermo Scientific) was used throughout. Dialysis and concentration of NCs by ultrafiltration was performed using Vivaspin centrifugal concentrators with PES membranes (Sartorius Stedim). Gel filtration chromatography was performed on self-packed Superdex 200 columns, eluting with PBS, pH 7.4, using an AKTAprime plus system (GE Healthcare) with absorbance detection. Dynamic light scattering was performed on a DynaPro Titan instrument (Wyatt Technology) at the MIT Biophysical Instrumentation Facility. UV-vis absorbance spectra were taken using an HP 8453 diode array spectrophotometer or a BioTek Synergy 4 Microplate Reader, on which all photoluminescence spectra were also recorded. pH measurements were taken using an Orion PerpHecT Ag/AgCl electrode and Orion PerpHecT model 310 LogR Meter. PBS refers to phosphate buffered saline containing 10 mM phosphate, 137 mM NaCl, 2.7 mM KCl. STE buffer refers to 10 mM tris(hydroxymethyl)aminomethane, 2 mM ethylenediaminetetraacetic acid, and 100 mM NaCl. MES buffer refers to 100 mM 2-(N-morpholino)ethanesulfonic acid, 100 mM NaCl. The following buffers were prepared at different pH values between 6.0 and 8.0 for assessing sensor performance: PBS (defined above); cytosol buffer (10 mM phosphate, 12 mM NaCl, 139 mM KCl); divalent buffer (12 mM phosphate, 137 mM NaCl, 2.7 mM KCl, 0.9 mM Ca^{2+}, 0.5 mM Mg^{2+}). To ensure accurate assessment of the final pH in diluted sensor samples, the sensors were first dialyzed against 0.1 buffers (1 mM phosphate), containing the appropriate electrolyte concentrations, before diluting to the desired concentration with 10 mM buffer at the target pH.

Cell culture and imaging HeLa cells were cultured at 5% CO_2 and 37 °C in MEM supplemented with 10% FBS and 50 U/50μg of penicillin/streptomycin, in 8-well Labtek chamber slides. When 80% confluent, these cells were incubated in plain PBS or in PBS containing NC constructs (diluted to a final concentration of

200 nM from a stock solution in MES, pH 6.5) at 5% CO_2 and 37 °C. After NC incubation, all wells were washed with PBS to remove any excess constructs before further incubation at 5% CO_2 and 37 °C for varying lengths of time and imaging under a confocal microscope. Imaging was carried out using a Nikon TE confocal microscope with a 60x water immersion objective, green channel 570/20 and red channel 605/30; 3.5-4.0x magnification on the software; $n = 4$ acquisitions. For all images, background/autofluorescence subtraction and data analysis were done in Matlab. Numerical analysis consisted of discarding out-of-focus signals by picking out only the highly fluorescent signals, calculating the ratio of fluorescence collected through the green channel and the red channel on each pixel, and calculating the average of these ratios within the same endosome.

Preparation of water-soluble QDs for sensor and control constructs Polymeric imidazole ligand (PIL) 1, a random copolymer, consisting 25% methoxy-terminated oligo(ethyleneglycol) side chains, 25% aminoethyl oligo(ethyleneglycol) sidechains and 50% imidazole sidechains was synthesized according to our previous report. Typical polymer characteristics (as determined by GPC analysis with reference to polystyrene standards) were Mw = 15.1 kDa (corresponding to an average of 32 monomer units per polymer chain); PDI = 1.2. The native hydrophobic trioctyl phosphine and trioctyl phosphine oxide NC ligands were displaced by PIL 1 as follows. CdSe/CdS coreshell quantum dots in trioctylphosphine/octadecene (typically 2 nmol) were precipitated by the careful addition of acetone and methanol. After centrifugation, the supernatant was discarded and the pellet re-dispersed in chloroform (25μL).This solution was added to PIL 1 (5 mg) in chloroform (25μL) under vigorous stirring. After 10 minutes, methanol (30μL) was added and stirring continued for a further 30 minutes. After this time, the solution was diluted with an ethanol/chloroform mixture (1 : 1 v/v) and precipitation induced by the addition of hexane. The nanoparticles were collected by centrifugation, and the supernatant discarded. The pellet was re-dispersed in ethanol/chloroform (1 : 1 v/v) and the precipitationcentrifugation cycle repeated once more. The resulting product was then dissolved in water, filtered

through a 0.2μm HT Tuffryn membrane and dialyzed against PBS, pH 7.4 buffer. The concentration of the recovered solution was determined by UV-Vis spectroscopy.

Oligonucleotide preparation The functionalized single-stranded oligonucleotide sequences below were supplied by Integrated DNA Technologies.

5'-CTC TCT CCT TTC TCC TGT ACA TCC TCT TTC CTC TC-ROX-3'

5'-AGG AGA AAG GAG AGA G$(CH_2)_3SS(CH_2)_3$OH-3'

Each oligonucleotide was re-suspended at 100μM in STE buffer, pH 8.0. Equal aliquots of each strand were mixed, heated to 94 °C and allowed to cool slowly to produce duplex samples. Immediately prior to use, the disulfide protecting group was reductively cleaved by addition of 1M dithiothreitol (300 equiv.) in PBS, followed by incubation for 30 min then purification on an illustra NAP desalting column (GE Healthcare).

Final preparation of sensor and control constructs For sensors, NCs in PBS (11μM) were treated with sulfosuccinimidyl-4-(N-maleimidomethyl)cyclohexane-1-carboxylate (300 equiv., 10 mM in H_2O) and the mixture incubated at 24 °C for 2h. After this time, excess crosslinker was removed by passage through an illustra NAP desalting column (GE Healthcare). The activated NCs were then mixed with deprotected oligonucleotide (10 equiv.) and the mixture shaken at 24 °C in the dark for 4.5 h. After this time, the solution was concentrated by ultrafiltration, and purified by GFC. Appropriate fractions were collected, concentrated and dialyzed against the appropriate buffer for the following experiment. The concentration of the resulting solution was determined by UV-Vis spectroscopy. Control constructs were prepared by attaching Rox fluorophores directly to the primary amines on PIL-coated NCs ligand (Scheme *S*1). Water-soluble NCs in PBS (11μL), prepared as described above, were diluted 1 : 1 (v/v) with 0.1 M $NaHCO_3$ (pH 8.3). To this was added 6-carboxy-X-rhodamine N-succinimidyl ester (8 equiv.) in H_2O. The mixture was incubated at 24 °C for 1 h in the dark, then filtered through a 0.2μm HT Tuffryn membrane and purified by GFC. Collected fractions were concentrated by ultrafiltration and

dialyzed against an appropriate buffer. The concentration of the resulting solution was determined by UV-Vis spectroscopy.

Appendices

Appendix A

Calculating the experimental FRET efficiency

The overall efficiency of energy transfer (E_{expt}) from the NC donor (D) to appended acceptor(s) (A) is commonly ascertained by determining the extent of quenching experienced by the donor species as a result of FRET (equation A.1), using intensity recorded under identical conditions and normalized for donor concentration.

$$E_{expt} = \frac{I_D}{I_D^0} \tag{A.1}$$

An alternative approach that does not require accurate measurement of sensor concentrations at the low optical densities required to avoid inter-construct energy transfer and other inner filter effects, is to use the proportion of total emission coming from the donor (R), which can be expressed as equation A.2.

$$R = \frac{I_D}{I_D + I_A} = \frac{\frac{\phi_D^0}{\phi_A^0}(1 - E_{expt})}{\frac{\epsilon_A^{460}}{\epsilon_D^{460}}M + \frac{\phi_D^0}{\phi_A^0}(1 - E_{expt}) + E_{expt}} \tag{A.2}$$

In equation A.2, the constants M and $\left(\frac{\epsilon_A^{460}}{\epsilon_D^{460}}\right)$ are easily determined. M is the ensemble number of acceptors per donor, determined by fitting the sensor absorption spectrum as shown in Figure A-1, while the ratio of extinction coefficients at the

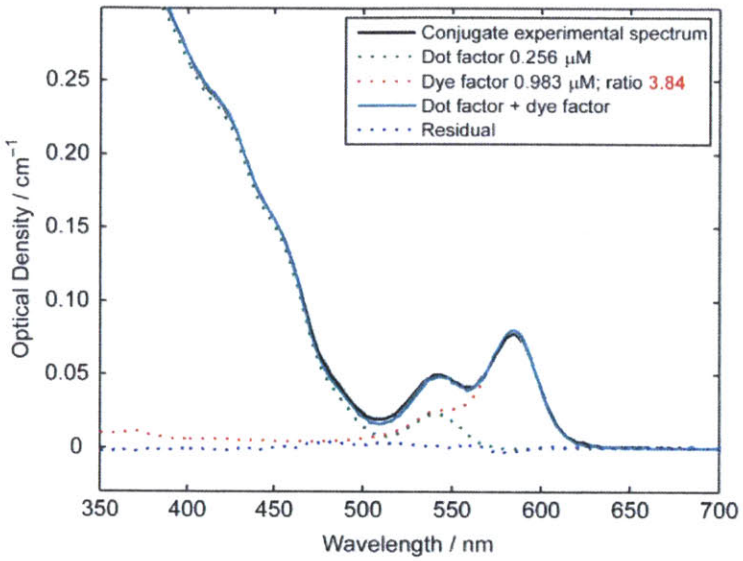

Figure A-1: Absorbance spectrum for a representative sensor conjugate. Spectrum was recorded in PBS at pH 7.39 buffer and the calculated individual NC and dye components, used to calculate the number of dyes per QD, are shown overlaid.

excitation wavelength $\left(\frac{\epsilon_A^{460}}{\epsilon_D^{460}}\right)$ measures the extent of direct excitation of acceptors.

The ratio of quantum yields in the absence of FRET $\left(\frac{\phi_D^0}{\phi_A^0}\right)$ varies slightly with pH as a result of the small but different responses of the donor and acceptor components to pH. The ratio was therefore determined at each pH value by creating NColigonucleotide and oligonucleotideRox reference samples that were subjected to the same synthetic and purification protocols as the sensor and measuring their PL spectra for samples of known concentration. Thus, the sensor PL spectra at each pH were deconvoluted into donor and acceptor components to determine R, and subsequently experimental FRET efficiencies at each pH could be calculated (Fig. 3-2d) using equation A.3.

$$E_{expt} = \frac{\left(\frac{\phi_D^0}{\phi_A^0}\right) - R\left(\frac{\epsilon_A^{460}}{\epsilon_D^{460}}M + \frac{\phi_D^0}{\phi_A^0}\right)}{\left(R\frac{(1-\phi_D^0)}{\phi_A^0} + \frac{\phi_D^0}{\phi_A^0}\right)} \tag{A.3}$$

Appendix B

Modeling the FRET Response

For a population of NC donors, each attached to identical energy acceptors, the energy transfer efficiency for each subspecies (E_i) can be calculated using equation B.1. The total ensemble FRET efficiency (E_{total}) is then obtained by summing contributions from each member of the population, weighted by their relative abundancies (equation B.2).

$$E_i = \frac{m_i R_0^6}{m_i R_0^6 + r^6} \tag{B.1}$$

$$E_{total} = \Sigma_i E_i P(m_i) \tag{B.2}$$

where,

$$P(m_i) = \frac{3.6^{m_i} e^{-3.6}}{m_i!} \tag{B.3}$$

In the current example, it is assumed that: first, each oligonucleotide switch exists in only as folded (A) or unfolded (B) the resulting difference being the distance r between the NC and Rox dye; and second, at the extremes of the pH range tested only one of these states exists to any significant extent (folded state A at acidic pH values; unfolded state B at basic pH values). Using equations B.1, B.2, B.3, we can plot the expected FRET efficiency with respect to the distance between the NC and the dye. Upon calculation, the expected sigmoidal variation as a function of donor acceptor distance, r is observed (Figure B-1).

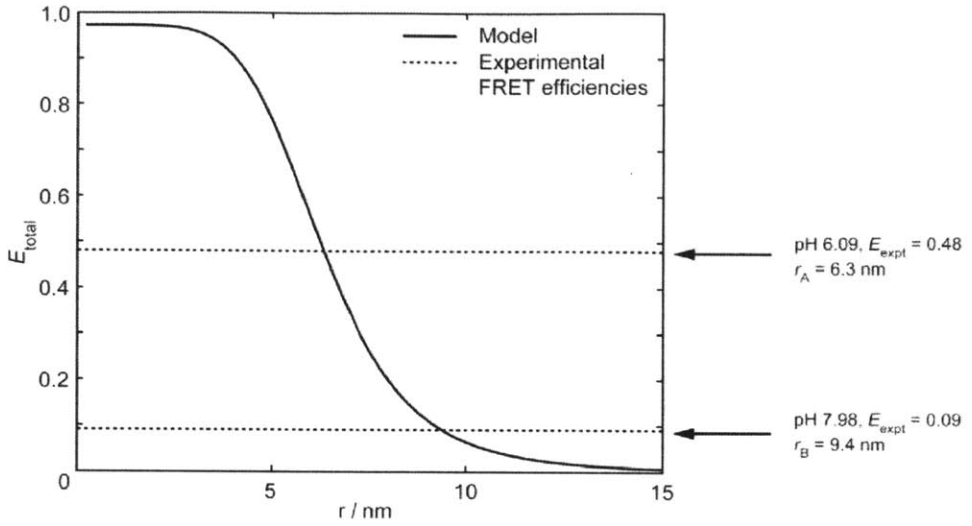

Figure B-1: Variation of FRET efficiency (E_{total}) with radius (r) for a population of NCRox constructs where the acceptor:donor ratio follows a Poisson distribution with average value 3.6, and comparison to experimentally determined FRET efficiencies E_{expt} at the extremes of the pH range investigated.

This plot can now be used to match the observed FRET efficiency calculated with equation A.3 above to the modeled FRET efficiency. Therefore, comparing the expected FRET efficiency (E_{total}) to the experimental values (E_{expt}) for pH 6.1 and 8.0 gives an estimation of the donor-acceptor distances in the folded and unfolded states (Figure B-1).

Appendix C

Endosome Image Analysis

C.1 Example

In order to collect the Green:Red ratio within the endosomes from confocal images, each cell image was processed by the Matlab code presented in the following pages. Figure C-1 describes the process of analysis using this code. Briefly, fluorescence images were subtracted of background (autofluorescence) level signals, followed by the signal on each pixel coming from the green channel being divided by the signal on that same pixel in the red channel. Endosomes were then hand-picked, and the $\frac{\text{Green channel}}{\text{Red channel}}$ within each endosome were averaged and recorded.

C.2 MATLAB CODE for Imaging Analysis

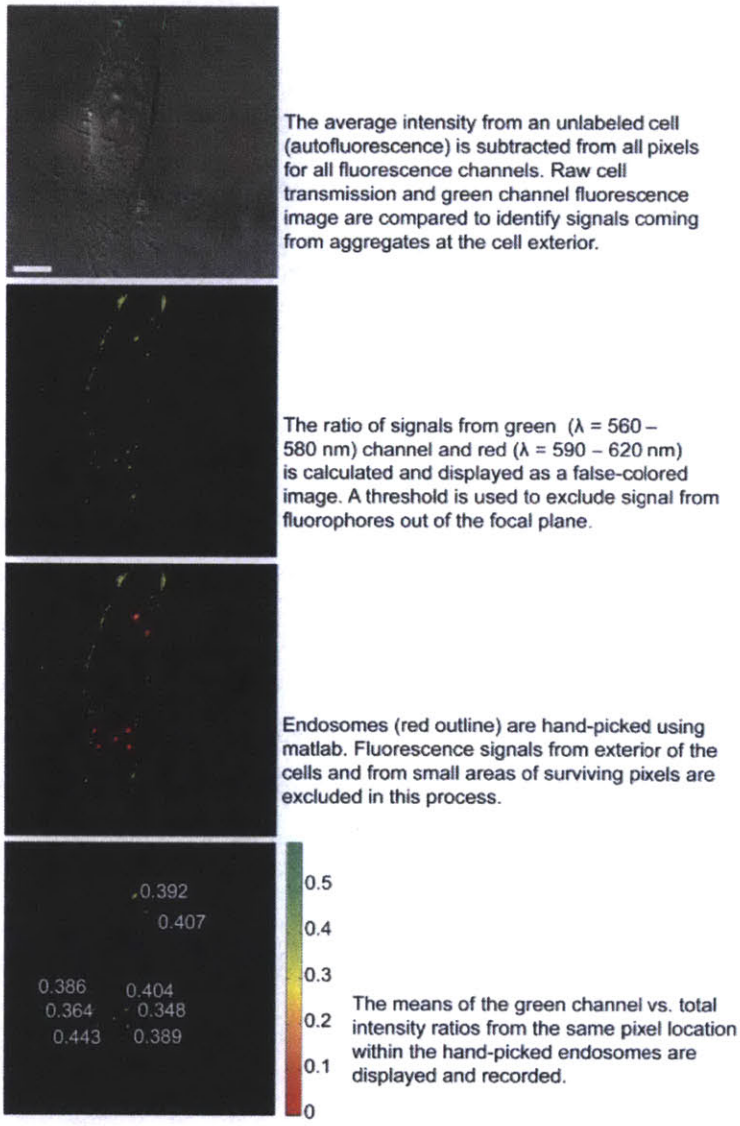

Figure C-1: Representative example depicting the steps involved in calculating fluorescence ratios from individual endosomes. Fluorescence that came from exterior of the cell, from out of the focal plane, and from aggregated samples was excluded from data points. (Scale bar = 10μm)

```
%% Script to load cell images, pick out good regions based on an appropriate
% THRESHOLD, then PICK REGIONS in this new ratio image

%% Choose Directory and Get Filenames
% Current path should include folders with scripts, but not those with
% image files
p = path;

% Get path of folder containing image folders. This would normally already
% be on search path as it contains the scripts written for these images
% (but it doesn't have to be).
% L = input('Type path of folder containing image folders: ', 's');
L = '/Users/JM/Desktop/Endosome picking';

F = '10+30 TIFF-3';
path(fullfile(L, F), path);
cd(F);
extention='.tif';

% For using all files, uncomment these lines
myfiles = dir(fullfile(L, F, '*.tif'));
myfilename = {myfiles.name};

%% setup structure & colormaps

Data = zeros(512, 512, 4, 'uint16');
Images = struct('filename', myfilename,...
                'Green', {zeros(512, 512, 'uint16')},...
                'Red', {zeros(512, 512, 'uint16')},...
                'DIC', {zeros(512, 512, 'uint16')},...
                'Green_bsub', {zeros(512, 512, 'uint16')},...
                'Red_bsub', {zeros(512, 512, 'uint16')},...
                'endoIm', {zeros(512, 512, 'double')},...
                'Ratios', {zeros(512,512, 'double')},...
                'Ratios_ABG', {zeros(512,512, 'double')},...
                'RatioAND_ABG_list', {[]},...
                'RatiosAND_ABG_mean', {[]},...
                'endos_index', {[]},...
                'endos_labeled', {[]},...
                'endovalues', {[]});
redmap=zeros(256,3);
redmap(:,1)=linspace(0,1,256);

greenmap=zeros(256,3);
greenmap(:,2)=linspace(0,1,256);

ratiomap=zeros(256,3);
ratiomap(1:128,1)=linspace(0,1,128);
ratiomap(129:256,1)=1;
ratiomap(1:128,2)=1;
ratiomap(129:256,2)=linspace(1,0,128);
ratiomap(1,:)=0;

ratiomapB=zeros(256,3);
ratiomapB(1:128,1)=1;
ratiomapB(129:256,1)=linspace(1,0,128);
ratiomapB(1:128,2)=linspace(0,1,128);
ratiomapB(129:256,2)=1;
ratiomapB(1,:)=0;

%% Load Data
for k=1:length(myfilename)
%     Data = importdata(strcat(myfilename{k}, extention)); % For when extension NOT included in
filename
    Data = importdata(myfilename{k}); % For when extension IS included in filename
    Images(k).Green = Data(:,:,2);
    Images(k).Red = Data(:,:,3);
    Images(k).DIC = Data(:,:,4);
end
```

```
%% Use a pre-determined background and AF values for each channel
% AF&background values determined together (N/Book II p127)
Green_corr  = 9;
Red_corr = 16;

for k=1:length(myfilename)
    Images(k).Green_bsub = imsubtract(Images(k).Green, Green_corr);
    Images(k).Red_bsub = imsubtract(Images(k).Red, Red_corr);

%     Show raw
%     figure(k), imshow(Images(k).Green_bsub, []), colormap(greenmap), colorbar,...
%     title([Images(k).filename ', Green bsub']);
%
%     figure(20+k), imshow(Images(k).Red_bsub, []), colormap(redmap), colorbar,...
%     title([Images(k).filename ', Red bsub']);
%
% %     Blur and show
%     figure(NUMBER), imshow(imfilter(Images(k).Green_bsub, h,'replicate'), []), colormap(greenmap),
colorbar,...
%     title([Images(k).filename ', Green bsub blur']);
%
%     figure(NUMBER), imshow(imfilter(Images(k).Red_bsub, h,'replicate'), []), colormap(redmap),
colorbar,...
%     title([Images(k).filename ', Red bsub blur']);
end

%% For each image, define appropriate threshold and use only pixels over this value
limitsDIC=[0 max(max(Images(k).DIC))];
G_thresh = 600;
R_thresh = 600;

% F_out = input('Folder name for output? ', 's');
F_out = strcat('singletime_threshthenpick_060411_', num2str(G_thresh), '_', num2str(R_thresh));
A = exist(F_out, 'dir');

if A==0
    mkdir(F_out);
end

cd(F_out);

for k = 8:length(myfilename)
    Greenmask = Images(k).Green_bsub > G_thresh;
    Redmask = Images(k).Red_bsub > R_thresh;

    MymaskA = Greenmask | Redmask; % For OR logic
    MymaskB = Greenmask & Redmask; % For AND logic

%     Show mask used
%     figure(40+k), imshow(MymaskB),...
%         title({['Mask for ' F ', ' Images(k).filename]; ['Using green threshold > '...
%         num2str(G_thresh) ' AND red threshold > ' num2str(R_thresh)]});
%     imagefile = strcat(myfilename{k}, '_mask_using_greenANDred_thresh_', num2str(G_thresh), '.eps');
%     print(gcf, imagefile, '-depsc2');

%     Calculate ratio image using ABG ratios
    Images(k).Ratios_ABG = double(Images(k).Green_bsub) ./...
        (double(Images(k).Green_bsub) + double(Images(k).Red_bsub));

%     FOR ABG RATIOS
%     NO infinities (if green+red = 0 then green = 0 and 0/0 gives NaN)
%     Identify NaNs(from green/red = 0/0) and convert to 0
    NN=isnan(Images(k).Ratios_ABG);
    Images(k).Ratios_ABG(NN)=0;
    clear NN

%     SHOW ABG RATIOS in regions determined by thresholds above
    figure(100+k),
    imshow(Images(k).Ratios_ABG.*MymaskB, []), colormap(ratiomapB), colorbar,...
        title({['ABG Ratio map of ' F ', ' Images(k).filename]; [' using green threshold > '...
        num2str(G_thresh) ' AND red threshold > ' num2str(R_thresh)]});
```

```
figure(400+k),
    imshow(Images(k).DIC, []), limitsDIC,...
    title({['DIC channel of ' myfilename{k} ]});

    % Basic Data Collect for ABG AND logic
    R_ABG_locations = (Images(k).Ratios_ABG.*MymaskB) ~=0;
    Images(k).RatioAND_ABG_list = Images(k).Ratios_ABG(R_ABG_locations);
    Images(k).RatiosAND_ABG_mean = mean(Images(k).RatioAND_ABG_list);

    clear R_ABG_locations Greenmask Redmask MymaskA MymaskB
end


%% Manually pick out some ROIs that look like they correspond to endos

for k=8:length(myfilename)

    figure(100+k), zoom reset,
    endos = input('How many endosomoes do you want to calculate? ');

%       OLD METHOD (still the best?!)
    Images(k).myroi = cell(1,endos);
    Images(k).roix = cell(1,endos);
    Images(k).roiy = cell(1,endos);
    BW = false(512, 512);

    figure(100+k), hold on,
    for j = 1:endos
%         disp([myfilename{k} ', Choose endosome ' num2str(j) ' of ' num2str(endos) '.'])
        message = strcat({[myfilename{k} ', choose endosome ' num2str(j) ' of ' num2str(endos) '.'];...
            'Take care not to inculde any zero-intensity pixels.'});
        uiwait(msgbox(message));
        [Images(k).myroi{1,j} Images(k).roix{1,j} Images(k).roiy{1,j}]=roipoly; % OR could do this as
layers in a 3D array?
        plot(Images(k).roix{1,j}, Images(k).roiy{1,j}, 'Color', [0.9 1 1]);
        BW = BW + Images(k).myroi{1,j};
        zoom out,
    end
    hold off
    BW=logical(BW);

    imagefile = strcat(myfilename{k}, '_marked_rois_after_greenANDred_thresh_', num2str(R_thresh),
'.eps');
    print(gcf, imagefile, '-depsc2');

    Images(k).endos_index = bwconncomp(BW);
    Images(k).endos_labeled = labelmatrix(Images(k).endos_index);
    Images(k).endoIm = Images(k).Ratios_ABG.*BW;

    figure(120+k), imshow(Images(k).endoIm, []), colormap(ratiomapB), colorbar,...
        title([myfilename{k} ', abg ratios in regions picked after thresholding.' ]);

    imagefile = strcat(myfilename{k}, '_rois_only_after_greenANDred_thresh_', num2str(R_thresh),
'.eps');
    print(gcf, imagefile, '-depsc2');

%     Pull out data for each of the defined regions
    Images(k).endovalues = regionprops(Images(k).endos_index, Images(k).Ratios_ABG, 'centroid',
'MeanIntensity', 'PixelValues');

    centroids = cat(1, Images(k).endovalues.Centroid);

    figure(120+k), hold on
    for j = 1:length(centroids)
        x = centroids(j, 1);
        y = centroids(j, 2);
        text(x,y,num2str(Images(k).endovalues(j).MeanIntensity, 3), 'Color', [0.9 1 1]);
    end

    hold off
```

```
imagefile=strcat(myfilename{k}, '_rois_only_after_greenANDred_thresh_', num2str(R_thresh),
'_labelled.eps');
    print(gcf, imagefile, '-depsc2');

    clear BW centroids

end

%% Collect Data

AND_ABG_Ratios_m = [Images.RatiosAND_ABG_mean]; % Global mean ratios for each image just based on
threshold image

A=vertcat(Images.endovalues);
Ratio_means = [A.MeanIntensity];

PixelRatios = vertcat(A.PixelValues);

clear A

save('thresh_then_pick');

%% Remove image folder from search path, ready for next loop
cd ../../
path(p);
```

Appendix D

Error/Uncertainty Due to the Stochastic Nature of Conjugation Reactions

Through a short statistical analysis, it was found that the size of the error bars depicted in figures 3-5 and 3-6 arises from the Poisson distribution of dye-valency per QD. A short simulation of the error bar on a population of endosomes with $3, 4, 5...$ QDs, each QD having a Poissonian probabilized number of Rox dyes per Dot, was carried out to find out the theoretical precision limit of our pH sensor construct. The assumptions and process were as follows:

1. Generate a histogram of a poisson distributed number of Rox conjugated per dot, knowing the ensemble average is 4.8 Rox per QD .

2. Assume that one Rox per QD corresponds to some pH-dependent $\frac{G}{(G+R)}$ and two Rox per QD corresponds to another $\frac{G}{(G+R)}$, etc. With this assumption, we can assign each the frequency of corresponding $\frac{G}{(G+R)}$ that is observed. This is our new x-axis. (Almost like change of variable)

3. From the population of observed $\frac{G}{(G+R)}$ above, calculate the mean and SD of having a bunch of endosomes with 1 pH sensor per endosome.

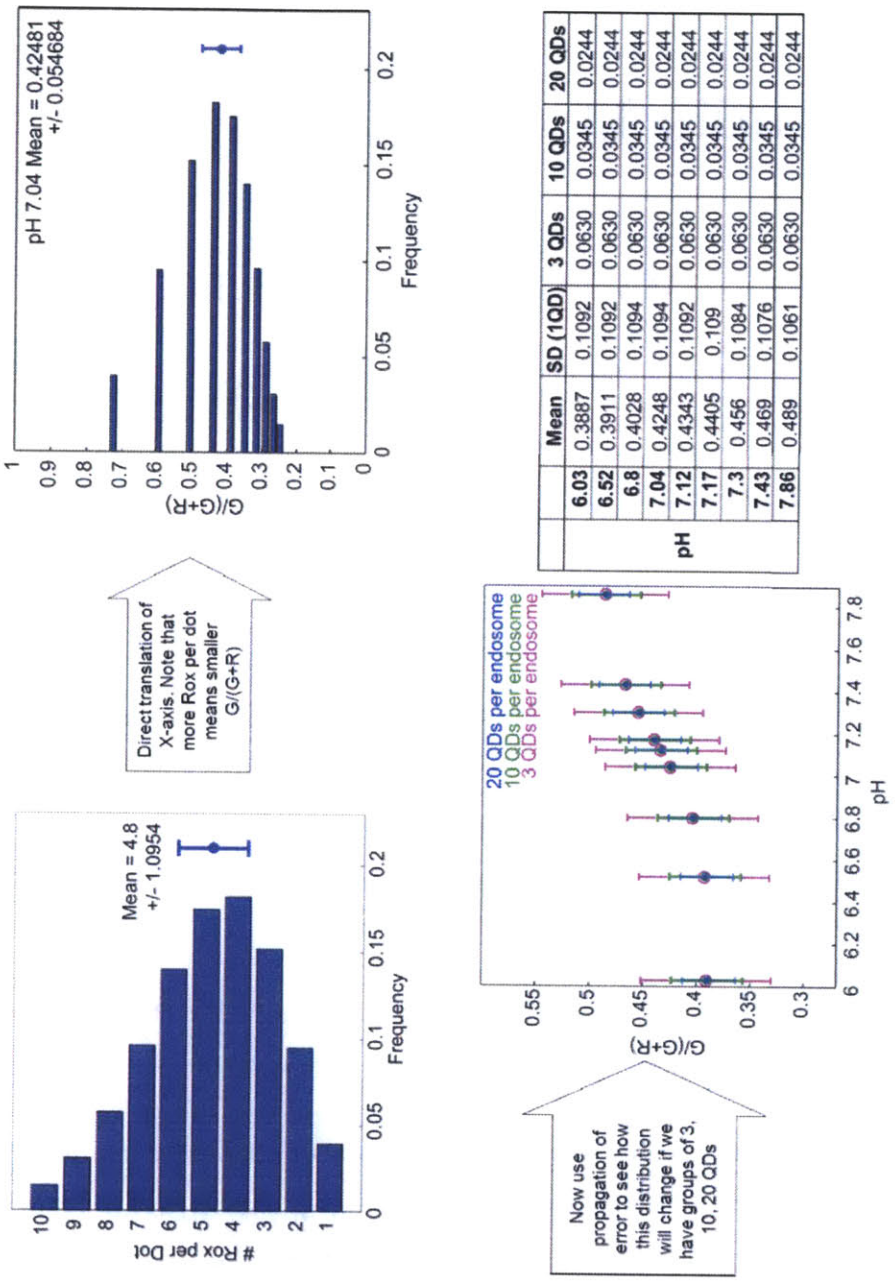

pH	Mean	SD (1QD)	3 QDs	10 QDs	20 QDs
6.03	0.3887	0.1092	0.0630	0.0345	0.0244
6.52	0.3911	0.1092	0.0630	0.0345	0.0244
6.8	0.4028	0.1094	0.0630	0.0345	0.0244
7.04	0.4248	0.1094	0.0630	0.0345	0.0244
7.12	0.4343	0.1092	0.0630	0.0345	0.0244
7.17	0.4405	0.109	0.0630	0.0345	0.0244
7.3	0.456	0.1084	0.0630	0.0345	0.0244
7.43	0.469	0.1076	0.0630	0.0345	0.0244
7.86	0.489	0.1061	0.0630	0.0345	0.0244

Figure D-1: Process of calculating the error bar of $\frac{G}{(G+R)}$ values within endosomes.

Incub (min)	Mean	SD	SEM
10 min	0.447	0.0704	0.0226
10 min + 10 min	0.437	0.0592	0.0100
10 min + 20 min	0.408	0.0690	0.0178
10 min + 30 min	0.384	0.0746	0.0134

Values are all within 1~10 QDs

Figure D-2: Actual measured errorbar size from endocytosed pH sensors.

4. Now calculate the SD of a bunch of endosomes if we had $3, 4, 5 \ldots 20$ QDs in each of them.

The process is demonstrated in figure D-1 along with the predicted error bar sizes for a population of endosomes containing various numbers of QD per endosome. When compared to the measured error bar size (Fig. D-2), the degree of uncertainty is consistent with having on the order of 1-10 QDs per endosome inside the cells.

Bibliography

[1] C. K. Zoon, E. Q. Starker, A. M. Wilson, M. R. Emmert-Buck, S. K. Libutti, and M. A. Tangrea. 2009. *Expert Rev Mol Diagn* **9**(5):455-467.

[2] M. J. Heslin, J. J. Lewis, J. M. Woodruff, and M. F. Brennan. 1997. *Annals of Surgical Oncology* **4**(5):425-431.

[3] G. S. Wilson and R. Gifford. 2005. *Biosensors and Bioelectronics* **20**:2388-2403.

[4] J. J. Burmeister, M. Palmer, and G.A. Gerhardt. 2003. *Anal. Chim. Acta* **481**:65074.

[5] J. P. Lowry and M. Fillenz. 2001. *Bioelectrochemistry* **54**:39-47.

[6] R. Freeman, et al. 2009. *Angew. Chem. Int. Ed.* **48**:309-313.

[7] I. L. Medintz, et al. 2010. *Nature Mater.* **9**:676-684.

[8] D.R. Larson, et al. 2003. *Science* **300**:1434-1436.

[9] R. Klajn, J.F. Stoddart, and B. A. Grzybowski. 2010. *Chem. Soc. Rev.* **39**:2203-2237.

[10] M. Stroh, et al. 2005. *Nat. Med.* **11**:678-682.

[11] O. T. Bruns, et al. 2009. *Nature Nanotech.* **4**:193-201.

[12] R. C. Somers, M. G. Bawendi, and D. G. Nocera. 2007. *Chem. Soc. Rev.* **36**:579-591.

[13] M. Suzuki, Y. Husimi, H. Komatsu, K. Suzuki, and K. T. Douglas. 2008. *J. Am. Chem. Soc.* **130**:5720-5725.

[14] K. Boeneman, et al. 2009. *J. Am. Chem. Soc.* **131**:3828-3829.

[15] I. L. Medintz et al. 2003. *Nature Mater.* **2**:630-638.

[16] R. Freeman, T. Finder, L. Bahshi, and I. Willner. 2009. *Nano Lett.* **9**:2073-2076.

[17] R. Freeman, et al. 2009. *Angew. Chem. Int. Ed.* **48**:309-313.

[18] S. Wang, M.-Y. Han, and D. Huang. 2009. *J. Am. Chem. Soc.* **131**:11692-11694.

[19] P. T. Snee, et al. 2006. *J. Am. Chem. Soc.* **128**:13320-13321.

[20] E. J. McLaurin, A. B. Greytak, M. G. Bawendi, and D. G. Nocera. 2009. *J. Am. Chem. Soc.* **131**:12994-13001.

[21] L. E. Page, X. Zhang, A. M. Jawaid, and P. T. Snee. 2011. *Chem. Commun.* **47**:7773-7775.

[22] J. Bath and A. J. Turberfield. 2007. *Nature Nanotech.* **2**:275-284.

[23] S. Modi, et al. 2009. *Nature Nanotech.* **4**:325-330.

[24] M. Brucale, G. Zuccheri, and B. Samori. 2005. *Org. Biomolec. Chem.* **3**:575-577.

[25] W. H. Liu, et al. 2010. *J. Am. Chem. Soc.* **132**:472-483.

[26] I. Mellman, R. Fuchs, and A. Helenius. 1986. *Annu. Rev. Biochem.* **55**:663-700.

[27] J. W. Liu, Z. H. Cao, and Y. Lu. 2009. *Chem. Rev.* **109**:1948-1998.

[28] L. Kovbasyuk, and R. Krámer. 2004. *Chem. Rev.* **104**:3161-3187.

Chapter 4

Delivering QDs into Intracellular Compartments

4.1 Semi-Permeable Barrier into Cells

Engineered nanomaterials have immense potential as live cell imaging tools, therapeutic molecular delivery agents, or even as ways to manipulate live cells with external handles such as light or magnetic fields [1]. For example, quantum dots (QDs) as fluorescent labels have provided new insights into cellular processes such as the dynamics of receptor proteins [2],[3]. But much of these potential applications require that nanomaterials be delivered into the cell cytosol. Herein lies the challenge of nanoparticle applications in biology: invention of an entryway through the double phospholipid bilayer for a man-made, nanometer-scale particle. Due to the difficulty of this challenge, biological applications of nanomaterials have thus far been limited to proteins localized on the outer cell membrane. Most nanoparticles, such as QDs, need to be passivated with a polymer that renders the nanoparticles soluble in aqueous media, and this also generally prevents them from easily diffusing across the cell membrane. Microinjection and nanoneedle injection [4],[5] of nanoparticles is considered impractical due to specialized equipment/skills required and low throughput [6],[7], while electroporation [8],[9] may cause QD aggregation inside the cell. Therefore, most attempts to deliver QDs into the cell cytoplasm have relied on QDs

being endocytosed by the cell and escaping from the endosome. Osmotic lysis of endosomes [10],[11], endosome escape by positively charged polymers [12]-[15] and cell-penetrating peptides [11],[16], and liposome-mediated delivery [17] have demonstrated some cytosolic delivery as supported by evidence including diffuse staining patterns on confocal microscopy. Unfortunately, all suffer from some combination of low reproducibility, low cell viability, incomplete endosome escape, and poor delivery efficiency. In addition, such approaches require achieving a well-controlled dual conjugation of an intracellular delivery handle and a cytosolic protein-targeting handle on the same nanoparticle, which can be difficult. Despite reports of reliable cytosolic delivery of gold nanoparticles [3],[18], quantum dots have yet to be delivered into the cell cytoplasm in a robust and scalable manner [19].

Because QD delivery into the cell cytoplasm has remained difficult, the utility of QD fluorescent labels in cell biology has been limited to fixed cell imaging or membrane protein labeling [1],[19] of live cells [2]. Fluorescence microscopy has provided countless insights into cellular architecture, biomolecule interactions, and protein localizations thanks to brighter, more stable fluorophores and fluorescent proteins (FPs). FPs in particular can be genetically encoded, ensuring labeling specificity and proper intracellular localization. However, FPs have shortcomings that may be complemented by the photostability, broad absorption bandwidth, high absorption coefficient, and narrow emission of QDs [20]. For example, QDs are emerging as strong candidates for single-molecule, long-term tracking studies in fluorescence microscopy because QDs provide an order of magnitude higher brightness than FPs and are more photostable [19],[21]. Unlike FPs, QDs are exogenous to the cell and thus need a conjugation handle that binds specifically to the protein of interest, in addition to being directed into the cellular compartment where the protein resides. Recent work has addressed the issue of specific conjugation through methods such as antibody targeting, streptavidin-biotin labeling schemes, HaloTag-chloroalkane and acyl carrier protein-acetyl CoA labeling [6],[22].

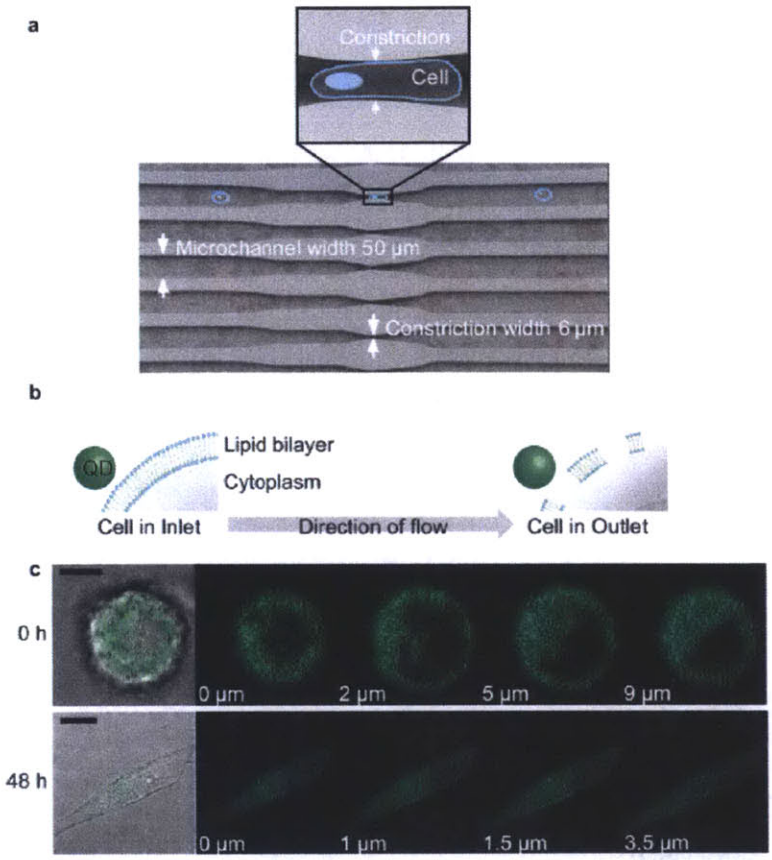

Figure 4-1: **a** Schematic of the microfluidic device and flow of cells. **b** Hypothesized method of entry for nanoparticles. Images not to scale. **c** Overlay of transmission and confocal fluorescence images, followed by z-section confocal fluorescence images of treated cells delivered with QDs. Top, immediately after treatment and bottom, after 48 h incubation at 37 °C and 5% CO_2. The diffuse staining pattern is constrained to the cytoplasm and the nanoparticles appear not to enter the nucleus (dark region within the cell). Scale bar is 10 μm.

4.1.1 Delivery Using a Microfluidic Device

The microfluidic, intracellular delivery device which we use here to deliver aqueous QDs into the cytosol, and its mechanism of delivery [23] are illustrated in figure 4-1a-b. In this device, cells are rapidly deformed as they pass through a constriction in a microfluidic channel, thus resulting in the formation of transient membrane disruptions. Macromolecules, such as QDs, may then diffuse into the cytosol during the life-time of these disruptions (Fig. 4-1b) [23]. Here we combine this microfluidic device with a new generation of recently described biologically compatible QDs [24]. The QDs used throughout this study were coated with a poly-imidazole ligand (PIL) comprised of multiple metal-chelating imidazole groups and multiple water-solubilizing, passivating poly(ethylene) glycol (PEG) [24]. The particular PIL that coated the QDs imaged in figure 1c had no functionality other than providing biocompatibility through PEG groups [24].

4.2 Results and Discussion: Device-Based Cytosolic Delivery of QDs

4.2.1 Delivery of PEG-coated, Biocompatible QDs into the Cytosol

Confocal microscopy images show that HeLa cells, detached and round after flowing through the microfluidic device, have diffuse cytoplasmic QD staining throughout different z-sections of the cell (Fig. 4-1c, top). The diffuse staining persists even after 48 hours, following incubation and adherence of the cells at 37 °C in 5% CO_2 (Fig. 4-1c, bottom). The diffuse QD fluorescence is dimmer at 48hrs, likely due to cell division (Fig. 4-1c). The device delivered QDs (~13 nm hydrodynamic diameter) into ~40% of the live cell population at a throughput rate of ~10,000 cells/s (Fig. G-4). Cell viability was >80% as measured by flow cytometry (Fig. G-1). The viability of treated cells as measured by flow cytometry, the diffuse staining on the confocal

images, and the cells ability to adhere are consistent with delivery of QDs into the cytoplasm of a live cell.

4.2.2 Delivery of a QD Construct that Interacts with the Cytosolic Environment

To confirm that the fluorescence indeed arises from QDs delivered to the cytosol as opposed to QDs sequestered in endosomes, we designed a nanoparticle engineered to change its emission profile upon interaction with the reducing environment of the cytosol. The reduction potential inside the cell cytoplasm is -260 to -220 mV and is primarily dictated by the maintenance of high concentrations (5-10 mM) of the tripeptide glutathione [25],[26]. Therefore, by measuring the fluorescence of a QD-dye construct whose emission changes when exposed to the cytosolic environment, we can simultaneously determine the localization and chemical accessibility of the delivered nanoparticles.

We engineered a QD-dye construct comprising of a green emitting QD ($\lambda_{emission}$ = 541 nm) that acts as an energy donor to a carboxy-X-Rhodamine (Rox) dye ($\lambda_{emission}$ = 610 nm), conjugated through a reducible disulfide bond (Fig. 4-2a). Thiol groups that were incorporated into the PIL formed disulfide bonds with thiolated Rox dyes. The absorbance spectrum of the purified construct has absorbance features of both QD (green arrow) and Rox (red arrow) (Fig. 4-2b) at an average of 13 Rox dyes per QD, effectively quenching the QD fluorescence (Fig 4-2c). This construct serves as an irreversible sensor of the specific reducing environment in the cytosol. When the QD is selectively excited by a laser at 488 nm (microscopy) or 405nm (flow cytometry) while the disulfide bridges are intact, the construct undergoes FRET so that Rox emission in the red dominates. In a solution assay, the cellular reductant glutathione cleaves the disulfide bridges, releasing Rox dyes and allowing the QD fluorescence to recover (Fig. 4-2d). The non-thiol based reductant tris-(2-carboxyethyl)phosphine also allows QD fluorescence recovery, indicating that the release of Rox from the QD surface is not via PIL displacement by glutathione (Fig. 4-2e). Rox fluorescence

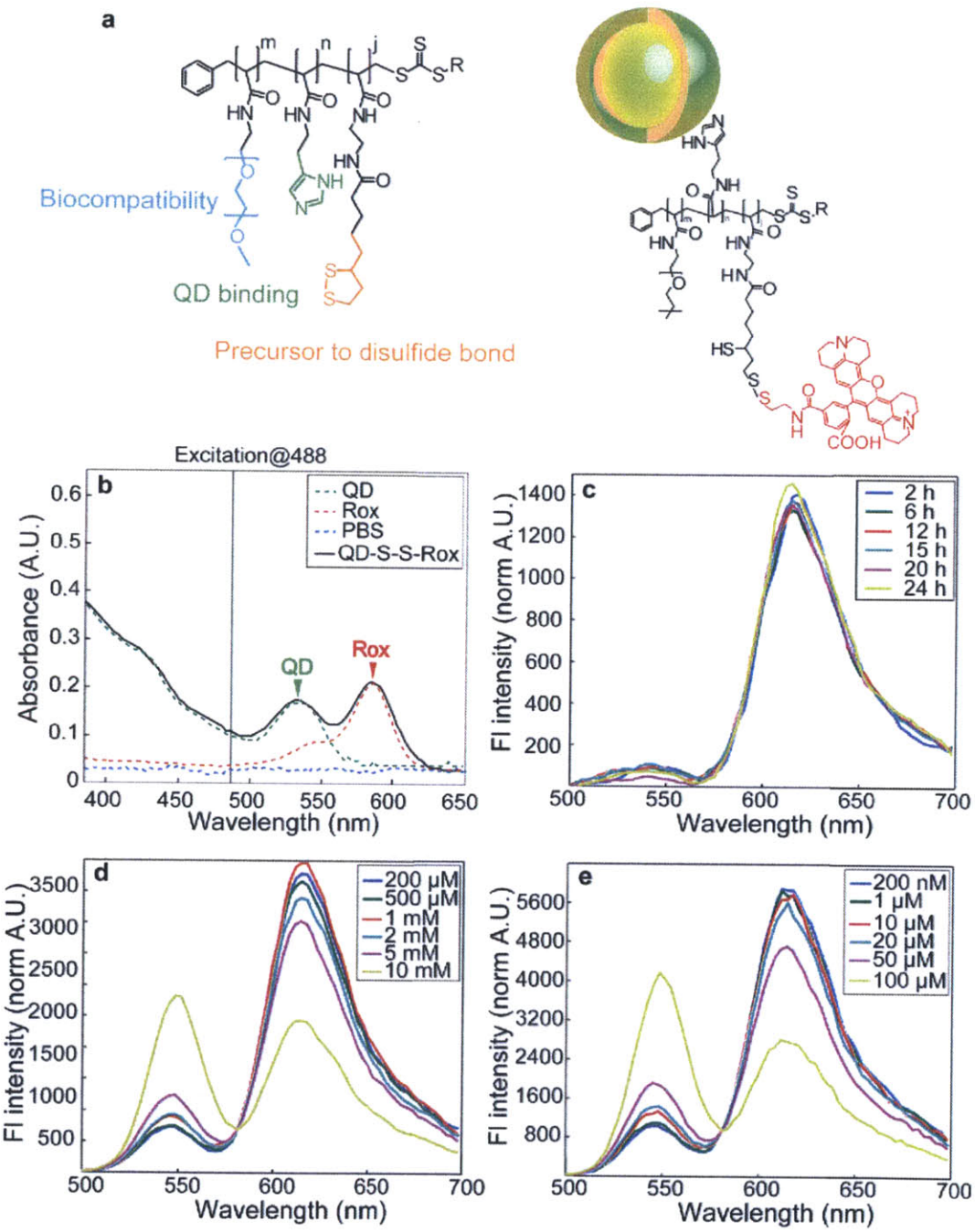

Figure 4-2: **a** Schematic of the PIL (left) and of the QD-S-S-Rox construct (right). Not to scale. **b** The absorbance spectrum of the QD-S-S-dye construct. Excitation at 488 nm and at 405 nm provided exclusive absorption by the QDs. **c** The stability of fluorescence energy transfer from QD to Rox for the construct in full culture media at 37 °C and 5% CO_2, demonstrating that the disulfide bond is not cleaved in the extracellular environment. **d** Recovery of QD fluorescence upon cleavage of the disulfide bond by the cytosolic reductant glutathione. **e** Recovery of QD fluorescence upon treatment by the non-thiol reductant tris(2-carboxyethyl)phosphine.

may not completely disappear due to some of the disulfide bridges being sterically hindered by long PEG groups on the PIL, and due to some small amount of non-specific interaction between the dye and the QD surface.

Changes in the fluorescence profile of the construct, as measured by flow cytometry and confocal microscopy, were used to confirm the delivery of QD-disulfide-Rox constructs to the cell cytoplasm. When exposed to the reducing cytosolic environment, the cleavage of the disulfide bonds disrupts the FRET process from the QD to the dye. Therefore, upon exclusive excitation of the QD, QD channel fluorescence increases while Rox channel fluorescence decreases with time. Live HeLa cells were treated by the microfluidic device in a solution with a high concentration of QD-disulfide-Rox, incubated for 5 minutes, and washed to remove excess QDs before adding cell culture media (these are referred to below as the treated cells). Control cells were incubated with QD-disulfide-Rox for 5 minutes instead of being treated by the microfluidic device, and washed before being placed in cell culture media (See Appendix for procedure and 40 minute incubation control). The Rox and QD channel fluorescence of these treated and control cells were observed by both confocal microscopy and flow cytometry.

Under the confocal microscope, the diffuse fluorescence that appears across the cytoplasm of treated cells progresses from strongly red to strongly green (Fig. 4-3a, top. See Appendix for additional images). Control cell images show some non-specific binding on the outer membrane as demonstrated by the ring-shaped fluorescence, and there is no increase in green channel signals (Fig. 4-3a, bottom). These effects are consistent with the expected cleavage of cytosolic disulfide bonds which reduce the FRET effect. In figure 4-3b, the line graph plots the average QD and Rox channel intensity per cell after correcting for cell-to-cell differences in delivered fluorescent material by normalizing for total fluorescence, for treated and control cells and autofluorescence. For treated cells, the graph shows a cross over between 2-4 hours of incubation where the QD fluorescence rises above the Rox fluorescence. Interestingly, the treated cell Rox signal is shown to stabilize above autofluorescence levels after 9 hours. This is consistent with results from solution assays, where some FRET re-

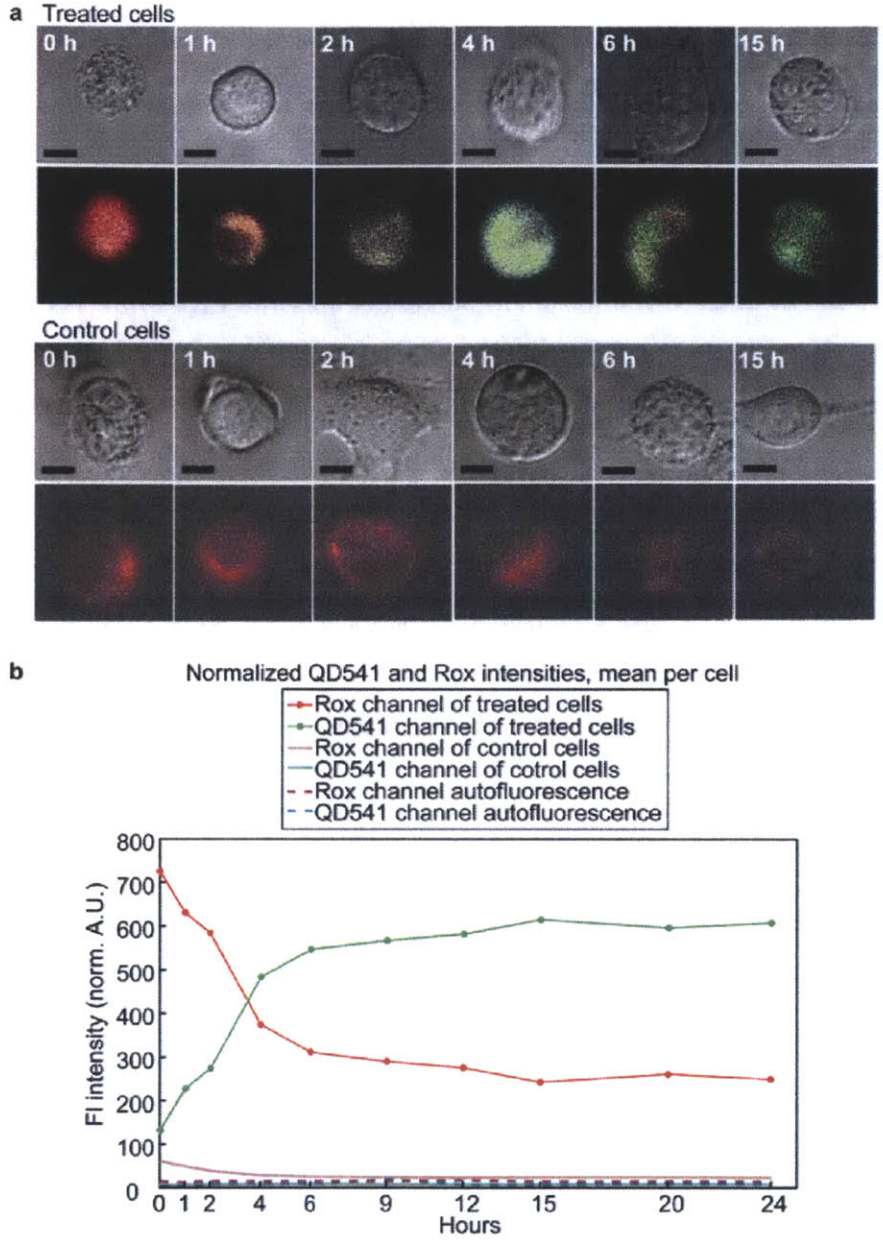

Figure 4-3: Live cell confocal microscopy images and fluorescence intensity analysis demonstrating cytoplasmic staining and chemical accessibility of QD surface. **a** Images of treated cells (top) and control cells (bottom). The appearance of diffuse green fluorescence is present only in treated cells. Scale bar is 10 μm. **b** Change in intensity as a function of time in the green and red channels. Because n<20 at each time point, fluctuations in total average fluorescence were corrected by normalizing to the 0 h time point.

mained after reduction. The observed diffuse staining and increase in QD signal and reduction in Rox signal strongly support cytosolic delivery and subsequent disulfide bond cleavage. The QD fluorescence in control cells, quenched by FRET to the Rox, appears indistinguishable from autofluorescence (Fig. 4-3b, Fig. H-3). The control cells display some Rox fluorescence above autofluorescence at early time points, which then steadily decreases. This is attributed to non-specific interactions between QD-S-S-Rox and the surface of the cell, followed by re-solvation of the constructs into the medium.

Flow cytometry measurements (Fig. 4-4) confirm that the QD-disulfide-Rox constructs can interact with the cytosolic environment. Flow cytometry measurements were recorded on all live cells, encompassing both delivered (~35% of the treated cell population, Fig. G-6) and undelivered cells. Figure 4-4a shows the average fluorescence per cell of the treated and control populations. The average QD fluorescence rises initially for the treated cells, peaking at ~9 hrs and falling gradually thereafter, in contrast to the QD fluorescence of the control cell population, which stays comparable to autofluorescence levels. This is consistent with the cytosolic reduction of disulfide bridges between the QD and dye inside the treated cells followed by dilution of fluorescence constructs by cell division. The Rox fluorescence for both the treated and control cells start high and drop within the first 2 hrs. This drop is attributed to the re-solvation into the medium of particles that had become bound to the cell surface during incubation. The average Rox fluorescence in the treated cell population appears similar to control cells due to the presence of undelivered cells within the treated population. The presence of both delivered and undelivered cells within the treated population can be distinguished in the histograms of QD and Rox intensity (Fig. 4-4b). With increasing time, the fluorescence histograms become bimodal for treated cells but stay unimodal for control cells. QD fluorescence rises with time in a subset of the treated cell population (Fig. 4-4b, left), further supporting the disruption of the FRET process in the cytosol of treated and delivered cells. Rox fluorescence decreases overall as membrane-bound constructs are re-solvated into the medium, but a subset of the treated cell population retains Rox fluorescence. This is

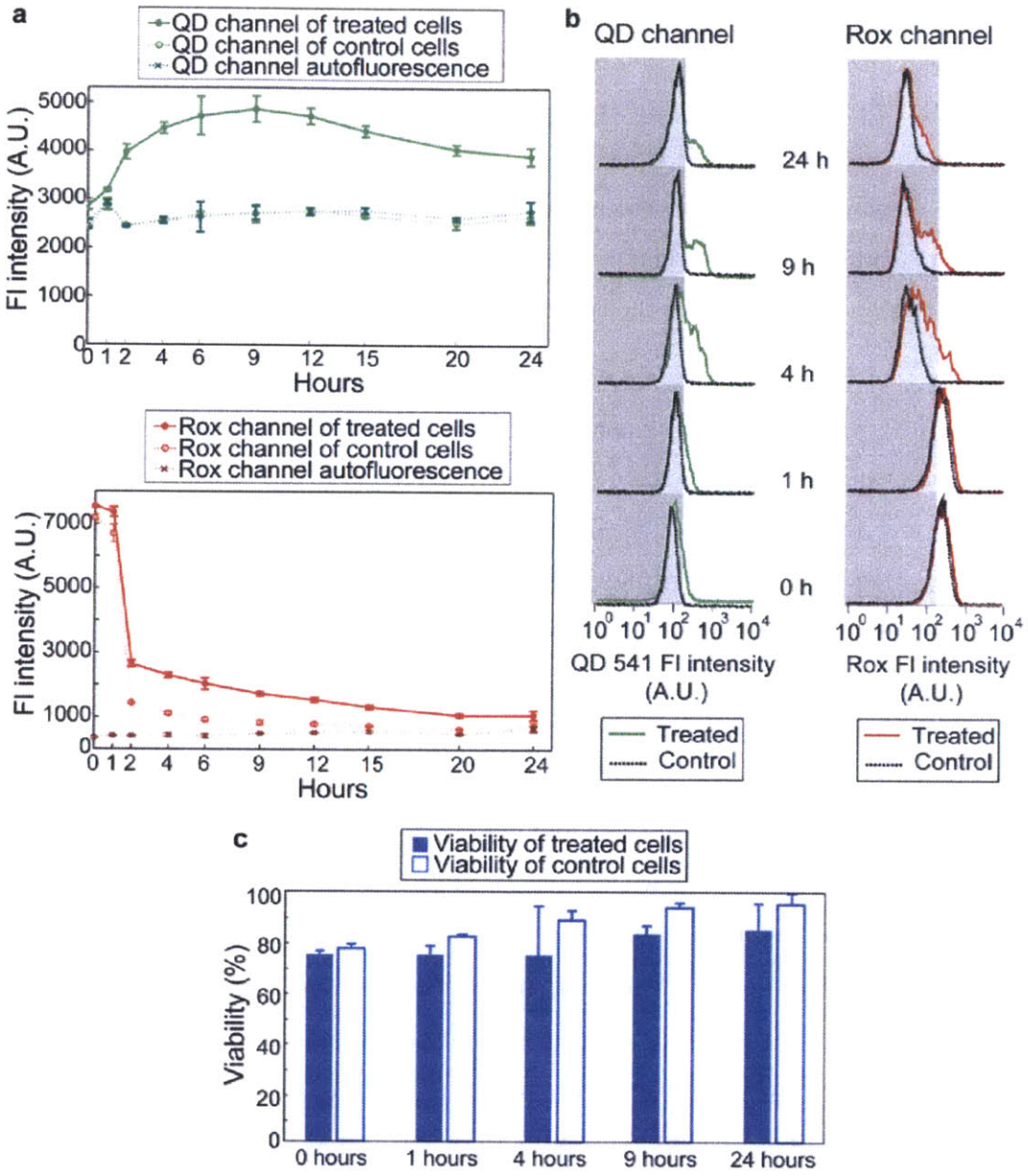

Figure 4-4: Flow cytometry measurements of average cell fluorescence and viability. **a** Average fluorescence of QD (left) and Rox (right) per cell, showing an increae in QD fluorescence only in treated cells. Rox fluorescence in both treated and control cells is at autofluorescence levels by the 24 h time point. **b** Histogram of the distribution of fluorescence intensities among treated and control cells at select time points, in the QD channel (left) and Rox channel (right). QD delivery is estimated to have occurred in at least 35% of the cell population (Fig G-6). Grey areas are meant to guide the eye in the movement of fluorescence intensity histogram peaks. **c** Viability of control and treated cells as measured by propidium iodide.

consistent with the incomplete reduction of QD-S-S-Rox bonds observed in confocal microscopy. The viability of the treated cell population, as measured by propidium iodide staining, is within 10% of the control population at all time points (Fig. 4-4c). Our cell viability of >90% relative to the control group compares favorably to alternative methods such as electroporation and polymer-based methods, which have yielded post-treatment viabilities as variable as 0-50% [27] and low as 40-60% [28], respectively.

4.2.3 Confirmation of Single QDs in the Cytosol

The QD delivery platform also enabled single molecule imaging by delivering un-aggregated QD-disulfide-Rox constructs, as the observed emission intermittency is consistent with single QDs [29]. For this experiment, QD-disulfide-Rox constructs were delivered into the cytosol followed by a 10 hour incubation and imaged on an epifluorescence microscope. The 10 hour incubation ensured that the QD fluorescence from inside the cytosol has recovered via disulfide bond reduction; epifluorescence microscopy was used to ensure that enough photons are collected. We observed several blinking QDs when cells were treated by the device at low QD concentrations (Fig. 4-5). Intensity traces of blinking QDs in the cytosol, shown in the bottom panel of figure 4-5, appear non-binary as a result of long acquisition bin times (500 ms). Translational cell movements were deemed minimal during the time frame of the acquisition ($\sim$1 min). This proof-of-concept experiment highlights the possibility of observing single molecule events within the cell cytosol by delivering QDs as fluorescent labels using this device.

4.3 Conclusion

In summary, we have demonstrated nanoparticle delivery into the cell cytosol using a novel microfluidic device. By observing the cleavage of QD-disulfide-Rox by cytosolic reductants, we show that the nanoparticle surface interacts with cytosolic components. The delivery platform, introduced and explained in full elsewhere [23],

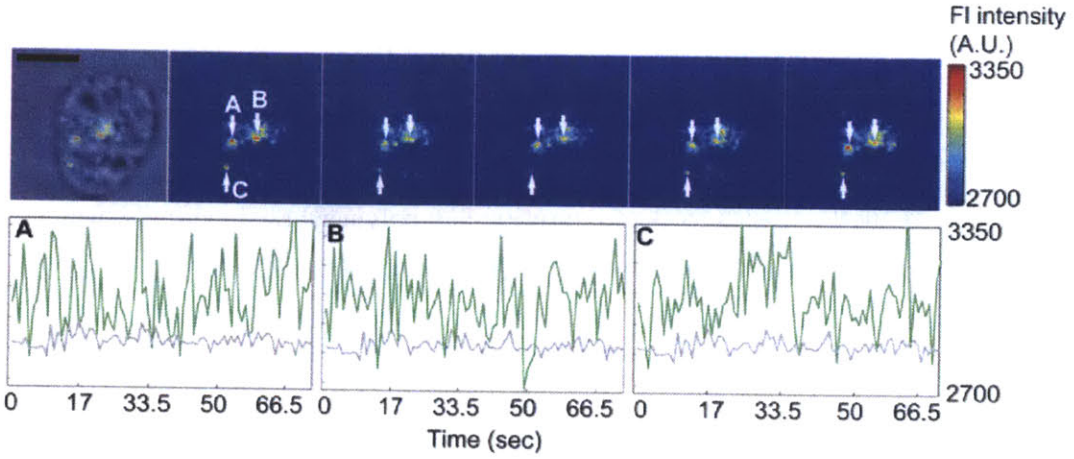

Figure 4-5: Epifluorescence imaging of unaggregated single QDs within the cell cytosol after device treatment with a 10 nM QD solution (top), and blinking traces of the three QDs labeled A, B, and C (bottom, green lines) with autofluorescence (bottom, grey lines). QD blinking traces appear to be non-binary due to long acquisition bin times (500 ms). Scale bars are 10 μm.

enables us to deliver QDs into the cell cytoplasm at high throughput without any cell penetrating or endosome escaping ligands, or laser ablation [30], while conserving cell viability and QD integrity. The delivery efficiency of 35% may be further increased by increasing the number of microfluidic constrictions, changing constriction dimensions, or increasing the number of treatment cycles. Unlike most of the current cell penetrating peptide or positive charge-assisted delivery methods, our approach does not require dual conjugation of an intracellular delivery handle and a cytosolic protein-targeting handle on the same nanoparticle. By dispensing the need for the former, we mitigate the concerns of cross-reactivity, unequal reactivity efficiencies of conjugation strategies, and conjugation stoichiometry. Therefore, we garner significant flexibility in QD construct design, paving the way for intracellular protein labeling and tracking. We expect this method to enable cytosolic delivery of many fluorescent nanomaterials with complex designs that target intracellular proteins and organelles through proven protein-targeting strategies such as streptavidin-biotin, HaloTag-chloroalkane, and sortase tagging [6],[22].

4.4 Experimental Details

Materials All chemicals were obtained from Sigma Aldrich and used as received unless indicated otherwise. Air sensitive materials were handled in an Omni-Lab VAC glovebox under dry nitrogen atmosphere with oxygen levels < 0.2ppm. All solvents were Spectroscopic or reagent. Aromatic ring-bearing compounds were visualized on TLC using a hand-held UV lamp and $KMnO_4$. Amine-bearing compounds were visualized on TLC using a Ninhydrin stain. Flash column chromatography was performed on a Teledyne Isco Combi Flash Companion. HeLa cells were purchased from ATCC and all cell medium materials were purchased from Mediatech unless indicated otherwise.

Instrumentation ^{1}H NMR spectra were recorded on a Bruker DRX 401 NMR Spectrometer. MS-ESI was performed on a Bruker Daltonics APEXIV 4.7 FT-ICR-MS machine. UV-Vis absorbance spectra were taken using an HP 8453 diode array spectrophotometer. Photoluminescence and absorbance spectra were recorded with a BioTek Synergy 4 Microplate Reader. Polymer molecular weights were determined in DMF solution on an Agilent 1100 series HPLC/GPC system with three PLgel columes ($103, 104, 105\mathring{A}$) in series against narrow polystyrene standards. Dye derivatives were purified using Varian ProStar Prep HPLC system. Modified polymer was purified using GE Healthcares PD-10 columns packed with SephadexTM G-25M. Ligand exchanged QDs were purified by centrifugation dialysis with Millipore Amicon Ultra 30K cut-off centrifugal filters and by GFC on AKTAprime Plus chromatography system (Amersham Biosciences) equipped with a self-packed Superdex 200 10/100 glass column. Flow cytometry measurements were made on LSR Fortessa (BD Biosciences).

QD synthesis CdSe cores with 478nm first absorption peak were synthesized using a previously reported method [31]. To summarize, 0.4 mmol (54.1mg) of CdO, 0.8 mmol (0.2232g) of TDPA, 9.6mmol (3.72g) of TOPO were placed in 25mL round bottom flask. The solution was degassed for 1 hr at 160 °C and heated to 300 °C under argon until the CdO dissolved and formed a clear homogenous solution. This

was followed by putting the solution under vacuum at 160 °C to remove evolved water. The solution was reheated to 360 °C under argon and a TOP-Se solution (1.5mL of 1.5M TOP-Se in 1.5mL of TOP) was rapidly added to give CdSe cores with the first absorption feature at 478nm. CdS shells were deposited on CdSe cores via modification of previously reported procedures [24]. Cores isolated by repeated precipitations from hexane with acetone were brought to 180 °C in a solvent mixture of oleylamine (3 mL) and octadecene (6 mL). Cd and S precursor solutions were then introduced continuously at a rate of 4 mL/hr. The Cd precursor consisted of 0.33 mmol Cd-oleate and 0.66 mmol oleylamine in a solvent mixture of octadecene (1.5 mL) and TOP (3 mL). The S precursor consisted of 0.3 mmol hexamethyldisilathiane [$(TMS)_2S$] in 6 mL TOP. Addition of a total of 3 monolayers each of Cd and S yielded QDs with emission at 541 nm and a quantum yield of 60% when diluted in octane. The extinction coefficient of CdSe(CdS) was calculated using the extinction coefficient of CdSe cores from the literature [32] and assuming that 95% of the CdSe cores were retained during the overcoating step.

Device fabrication and mounting system The silicon-based devices are fabricated at the MIT microfabrication facility using photolithography and deep reactive ion etching techniques. In this process, 6 silicon wafers with a 450μm thickness are treated with Hexamethyldisilazane (HMDS), spin coated with photoresist (OCG934, FujiFilm) for 60s at 3000rpm, exposed to UV light (EV1- EVG) through a chrome mask with the constriction channel design, and developed in AZ405 (AZ Electronic Materials) solution for 100s. After 20min of baking at 90 °C, the wafer is etched by deep reactive ion etching (SPTS Technologies) to the desired depth (typically 15μm). Piranha treatment (H_2O_2 and H_2SO_4) is used to remove any remaining photoresist after the etching process is complete. To etch the access holes (i.e. inlet and outlet) the process is repeated on the opposite side of the wafer (i.e. the one not containing the etched channels) using a different mask, which contains the access hole patterns, and a thicker photoresist AZ9260 (AZ Electronic Materials). Oxygen plasma and RCA cleaning are used to remove any remaining impurities. Wet oxidation is then

used to grow $100 - 200$nm of silicon oxide before the wafer is anodically bonded to a Pyrex wafer and diced into individual devices. Each device is individually inspected for defects prior to use.

Before each experiment, devices are mounted onto a holder with inlet and outlet reservoirs (all designed in-house and produced by Firstcut). These reservoirs interface with the device using Buna-N O-rings (McMaster-Carr) to provide proper sealing. The inlet reservoir is connected to a home-made pressure regulator system using Teflon tubing to provide the necessary driving force to push material through the device. The current system can only accommodate pressures up to 70psi.

Synthesis of PIL and QD construct The overall synthesis is shown as a scheme in figure 4-6. Detailed descriptions of the compounds and overall PIL follow.

Compound 1 To a solution of lipoic acid (5 g, 20 mmol) and dicyclohexylcarbodiimide (6 g, 30 mmol) in THF at 4 °C, a solution of N-hydroxysuccinimide (3.34 g, 30 mmol) in THF was added drop by drop. The solution was brought to room temperature and stirred for 3 h. The precipitate was removed by vacuum filtration and the solvent evaporated in vacuo, followed by a second precipitation in ethyl acetate and vacuum filtration. The crude product was recrystalllized from a solution of hot ethyl acetate/hexane (1:1 v/v) as a pale-yellow solid. ^{1}H NMR (400MHz, CDCl3): δ (ppm) 3.59 (1H, quin), 3.03-3.13 (2H, m), 2.85 (4H, t), 2.6 (2H, t), 2.45 (1H, quin), 1.91 (1H, quin), 1.63-1.8 (4H, m), 1.5-1.6 (3H, m)

Compound 2 A solution of lipoic acid NHS-ester (**1**, 2g, 6.6 mmol) in THF was added drop by drop to a solution of ethylene diamine (3.96 g, 70 mmol) and triethylamine (1.2 eq) in THF at 4°C. The reaction brought to room temperature and stirred until NMR of crude product in solution phase showed ethylene diamine peaks but no NHS peaks. The reaction was filtered and the solvent and excess ethylene diamine were removed in vacuo. Entire product was transferred to the next reaction to form compound 3.

Compound 3 To a solution of lipoic ethylene amine (**2**) and triethylamine (0.8 g, 10 mmol) stirring in dry THF at 4 °C, a solution of acroyl chloride(0.72 g, 10 mmol) in

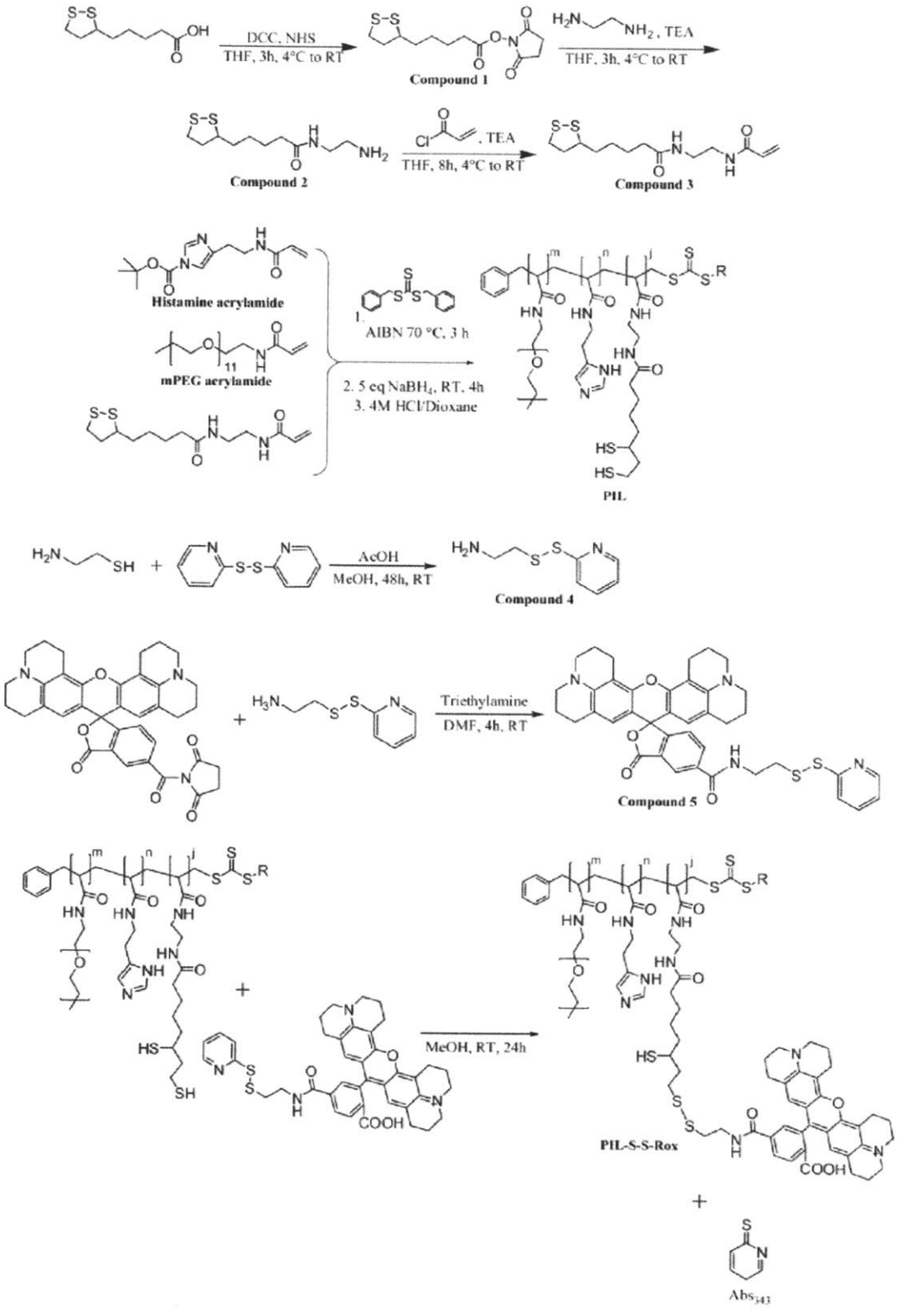

Figure 4-6: Synthesis scheme of PIL

THF was added drop by drop. The reaction was brought back to room temperature and stirred for 6 h. Disappearance of amine was monitored with TLC. The solution was filtered and the solvent evaporated in vacuo. The crude product was purified by silica column (4% to 10% methanol/dichloromethane gradient) to give the pure product. ^{1}H NMR (400 MHz, CDCl3): δ (ppm) 6.3 (1H, d), 6.19 (1H, q), 5.62 (1H,d), 3.5 (2H, sex), 3.43 (3H, m), 3.1 (2H, sex), 2.21 (1H, sex), 2.18 (2H, t), 1.83 (1H, sex), 1.61 (4H, m), 1.4 (1H, q)

Typical PIL synthesis Methoxy terminated poly(ethylene glycol)$_{11}$ acrylamide and Histamine acrylamide were synthesized with slight modifications on an established procedure [24]. Briefly:

Methoxy poly(ethylene glycol)$_{11}$ amine Neat methoxy poly(ethylene glycol) (mean MW 550, 8 g, 14.5 mmol), Ag_2O (5.06 g, 21.8 mmol), Tosyl chloride (3.05 g, 16 mmol), and KI (0.6 g, 3.6 mmol) were stirred in dichloromethane at RT overnight. Salts were filtered through celite followed by ethyl acetate wash of the crude solution. The solvent was evaporated in vacuo and the crude product purified by silica column (2% methanol/dichloromethane). The entire crude was dissolved in DMF and sodium azide (1.42 g, 21.8 mmol) was added. The reaction was stirred at 110 °C for 3 h, then cooled to RT and the solvent evaporated in vacuo. Tosylate salts were crashed out in dichloromethane until NMR showed tosylate peaks had disappeared. To the entire product dissolved in dry THF at 4 °C was added triphenylphosphine (4.2 g, 16 mmol). This reaction was brought to RT and stirred for 10 h, at which point 1 mL of water was added. After 3 h further stirring, the solvent was removed in vacuo and the crude product was purified with silica column (10% hydroxylamine0.1-methanol0.9/ethyl acetate).

Methoxy poly(ethylene glycol)$_{11}$ acrylamide The purified methoxy poly(ethylene glycol)$_{11}$ amine (1.3 g, 2.36 mmol) and triethylamine (0.36 g, 3.55 mmol) were dissolved in dry THF at 4 °C. A solution of acroyl chloride(0.32 g, 3.55 mmol) in THF was added drop by drop and the reaction brought back to room temperature and stirred for 6 h. Disappearance of amine was monitored with TLC. The solution was filtered and the solvent evaporated in vacuo. The crude product was purified by silica column (4% to

10% methanol/dichloromethane gradient) to give the pure product.

Histamine acrylamide To a solution of histamine free base (2.9 g, 26 mmol) and triethylamine (3.17 g, 31.3 mmol) in 2.2:1 DMF/THF mixture at at 4 °C was added a solution of acroyl chloride (2.83 g, 31.3 mmol) in DMF/THF drop by drop. The reaction was raised to RT and stirred for 6 h. Precipitates were filtered and the solvent was evaporated in vacuo. The crude product was purified on silica column (10% hydroxylamine0.1-methanol0.9/dichloromethane).

Boc-protected histamine acrylamide To a solution of purified histamine acrylamide and triethylamine (2.90 g, 28.7 mmol) in DMF was added a solution of Boc-anhydride (6.26 g, 28.7 mmol) in DMF drop by drop. The solution was stirred at RT for 6 h and purified by silica column (50% to 80% ethyl acetate/hexane gradient).

Polymer synthesis All monomers were kept as a dilute stock solution in ethylacetate. RAFT-mediated polymerization has been reported elsewhere [24]. To summarize, all monomers were weighed out volumetrically into an 8 mL vial. The solvent was removed in vacuo and RAFT reagent and AIBN were added along with dry DMF. The contents of the vial were mixed, centrifuged, and transferred to a 1 mL ampule. The ampule was freeze-pump-thawed 4x and sealed under vacuum. Polymerization proceeded in a 70 °C oil bath for 6 h.

PIL deprotection and reduction Disulfide on PIL was deprotected with 3-4 eq $NaBH_4$ in 1:4 MeOH/water mixture for 4 hours followed by quenching of $NaBH_4$ and deprotection of Boc-protecting groups with 0.5 mL of 4 M HCl in dioxane. After 1h at RT, the HCl was removed in vacuo. The deprotected polymer was dissolved in MeOH, to which a solution of NaOH in water (4M) was added dropwise to adjust the pH to be between 8-9. The solvent was removed in vacuo, and then $CHCl_3$ was added to precipitate the salts. The solution was filtered through a 0.45 μm PTFE filter and solvent removed in vacuo to yield the final polymer for Rox-S-S-pyr conjugation.

Compound 4 Aldrithiol-2 (4.98 g, 22.6 mmol) was dissolved in 40 ml of methanol and 1.8 ml of AcOH under N_2. A solution of 2-aminoethanethiol HCl (1.28 g, 11.30 mmol) in methanol was added drop by drop and the reaction was stirred at RT for 48 h. The solvent was evaporated in vacuo and the residual oil was washed 2x with

40 ml of diethyl ether. The crude compound was dissolved in 10 ml of methanol and the product was precipitated twice with cold diethyl ether to get the pure product as a white solid.

Compound 5 5(6)-Rox NHS ester from Invitrogen (100 mg, 0.16 mmol), triethylamine (22.4 mg, 0.22 mmol), and cysteamine thiopyridine (**4**, 41 mg, 0.22 mmol) were stirred in methanol for 4 hours. The product was extracted 2x in water/$CHCl_3$ and 4x in brine/$CHCl_3$. The crude product was purified with HPLC Varian column (45% to 100% ACN0.8/water/$TFA_{0.5\%}$ gradient). M/Z 703.2439 (100), 704.2483 (44.2), 705.2482 (18.4), 706.2492 (5.4).

PIL-S-S-Rox synthesis Varying equivalents of Rox-S-S-pyr was dissolved in methanol and added to a solution of PIL in methanol. The solution was stirred for 24 hours at room temperature, devoid of light. The mixture was precipitated with CHCl3 and filtered with a 0.45 μm PTFE filter, and solvent removed in vacuo to be dissolved in water. The aqueous solution of Rox-S-S-polymer was purified from excess Rox-S-S-pyr by PD-10 size exclusion column (GE-Healthcare). The solvent of the eluted product was removed in vacuo to yield the final PIL for QD ligand exchange.

Ligand exchange QDs (2 nmol) were precipitated using acetone and ethanol, and brought into 50 μL of $CHCl_3$. The QD stock solution was mixed with a solution of PIL-S-S-Rox (5 mg) in 30 μL, stirred for 15 min at RT, after which 30 μL of methanol was added. The solution was stirred for another 30 min, then precipitated by the addition of ethanol (30 μL) and $CHCl_3$ (30 μL) and excess hexanes. The sample was centrifuged at 4000xg for 2.5 min, clear supernatant discarded. The pellet redissolved in ethanol (50 μL) and $CHCl_3$ (50 μL) and precipitated by the addition of excess hexanes, centrifuged, and the supernatant discarded. The pellet was dried in vacuo and dissolved in PBS (500 μL, pH 7.4). The sample was purified by GFC with PBS (pH 7.4) as the mobile phase with a flow rate of 1.0 mL/min. Detection was achieved by measuring the absorption at 280 nm.

In summary, the QD-S-S-Rox construct synthesis scheme is as shown in fig. 4-6

Characterization of glutathione and TCEP reduction QD-PIL-S-S-Rox was incubated at 37 °C on a stirplate in a solution of varying concentrations of glutathione in PBS and varying concentrations of TCEP in PBS (pH adjusted to pH 7.4) for 30 minutes. Absorbance and emission were measured and recorded simultaneously on BioTek Synergy 4 Microplate Reader at 488 nm excitation.

Disulfide bond stability in full cell medium The construct was incubated on a 37 °C stirplate in air and its emission spectrum measured at various hours. To measure the stability of disulfide bond in full medium at 37 °C at 5% CO_2, the construct was incubated in a cell incubator and the emission intensity in QD541 and Rox channel was measured with a confocal microscope. The constructs were run on AKTA GFC column to measure any aggregation.

Cell culture HeLa cells were cultured in high glucose Dulbeccos modified essential medium supplemented with 10% FBS and 1% penicillin streptomycin, at 37 °C and 5% CO_2. When applicable, adherent cells were suspended in solution by treatment with 0.05% trypsin/EDTA for 5 minutes.

Confocal microscopy Confocal images were taken on live cells using the C1 confocal add-on unit on a Nikon TE2000-U inverted microscope with a 60x water-immersion lens. Fluorescence samples were excited at 488 nm from an argon-Ion laser. Emission was collected with a 585 Long-Pass dichroic mirror for QD541 fluorescence collection through 535/30 filter and Rox fluorescence collection through a 605/30 filter. A single image is an average from n=8 scans.

Epifluorescence microscopy Epifluorescence images were taken on live cells using a Nikon TE2000-U inverted microscope with a 60x water-immersion lens and a Princeton Instruments MicroMAX camera with an additional 1.5x magnification tube lens. Bright field images were collected using differencial interference contrast and 10 ms exposure. Fluorescence samples were excited from an LED lamp source centered on 480 nm excitation and collected with 50-500 ms exposure. Collection of

QD541 fluorescence was through a 460/30 nm excitation filter, 488 dichroic mirror, and 525/30 emission filter. Collection of Rox fluorescence was through a 488 dichroic mirror and 595/50 emission filter.

Flow cytometry Cells were centrifuged at 400 rcf and washed 2-3 times with PBS prior to being suspended in FACS buffer comprised of PBS supplemented with 3% FBS, 1% F-68 Pluronics (Sigma), and 10 μg/ml propidium iodide (Sigma). QD and QD-Rox fluorescence upon excitation at 405 nm excitation wavelength was analyzed. Dead cells were sorted out from the sample by discarding cells showing propiedium iodide fluorescence excited at 488 nm and measured through a 695 Long-Pass filter. Emission for QD541 was collected using a 525/50 filter and emission for Rox fluorescence was collected using a 595 Long-Pass filter.

Delivery procedure To perform an experiment, cells are first suspended in PBS (although growth medium or other buffers have been found to work equally well) mixed with the desired delivery material and placed in the devices inlet reservoir. This reservoir is connected to a compressed air line controlled by a regulator and the selected pressure (0-70psi) is used to drive the fluid through the device. Treated cells are then collected from the outlet reservoir. Cells are incubated at room temperature in the delivery solution for 5min post-treatment to ensure pore closure before being subject to any further treatment. All experimental conditions were carried out in triplicate and the error bars represent two standard deviations.

Appendices

Appendix E

Characterization and *in vitro* Analysis of QD Construct

Compound and PIL were characterized by a variety of methods including NMR, GPC, spectroscopy, and mass apectrometry, as appropriate.

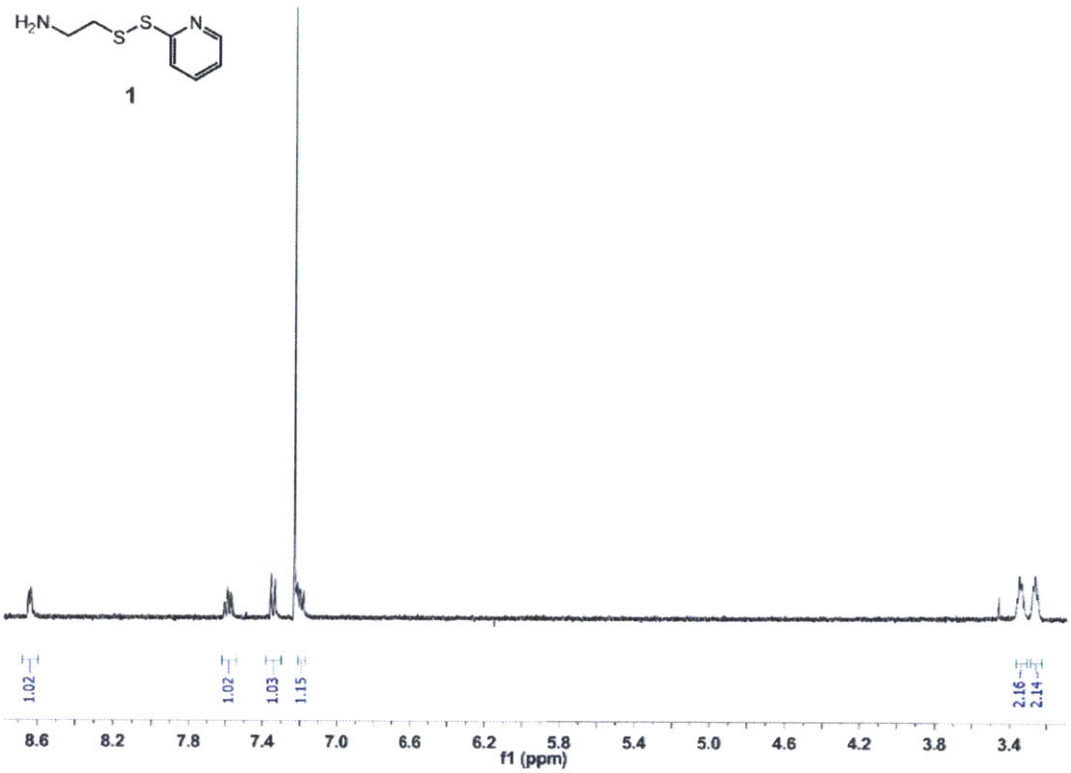

Figure E-1: NMR characterization of compound 1.

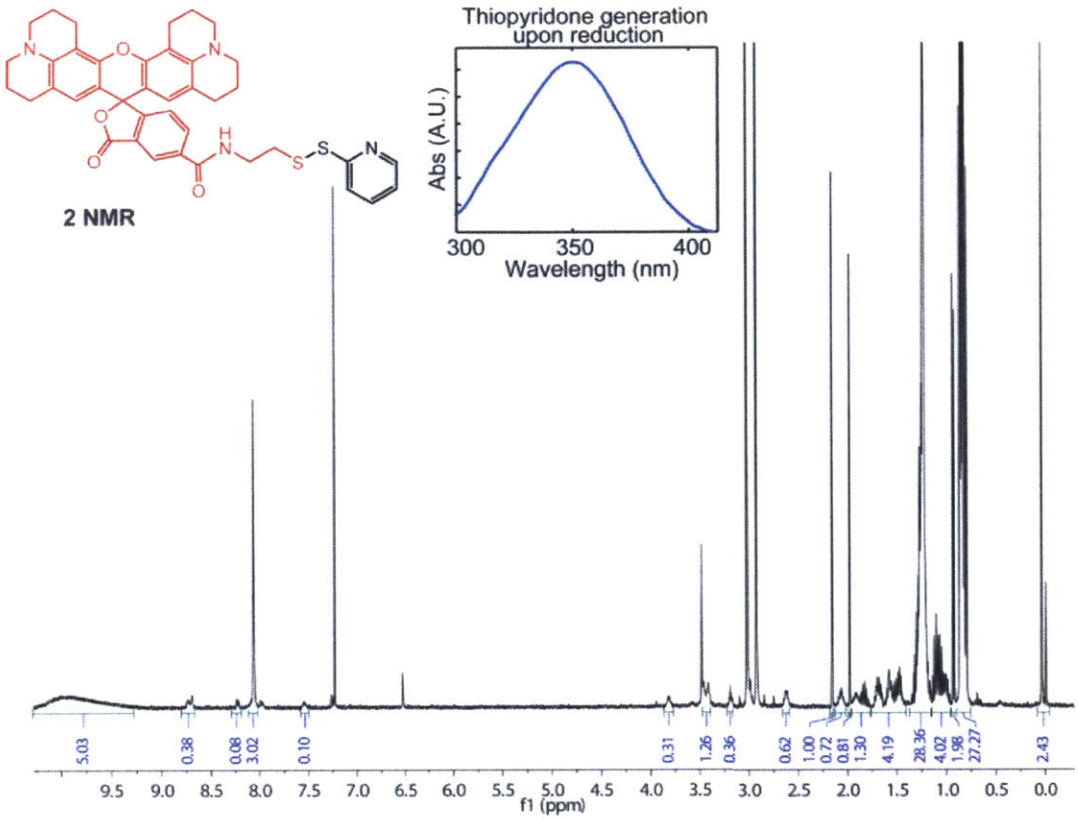

Figure E-2: NMR characterization of compound 2 and confirmation of thiopyridone formation when the compound is put in contact with a reductant, as measured by absorption at 350 nm.

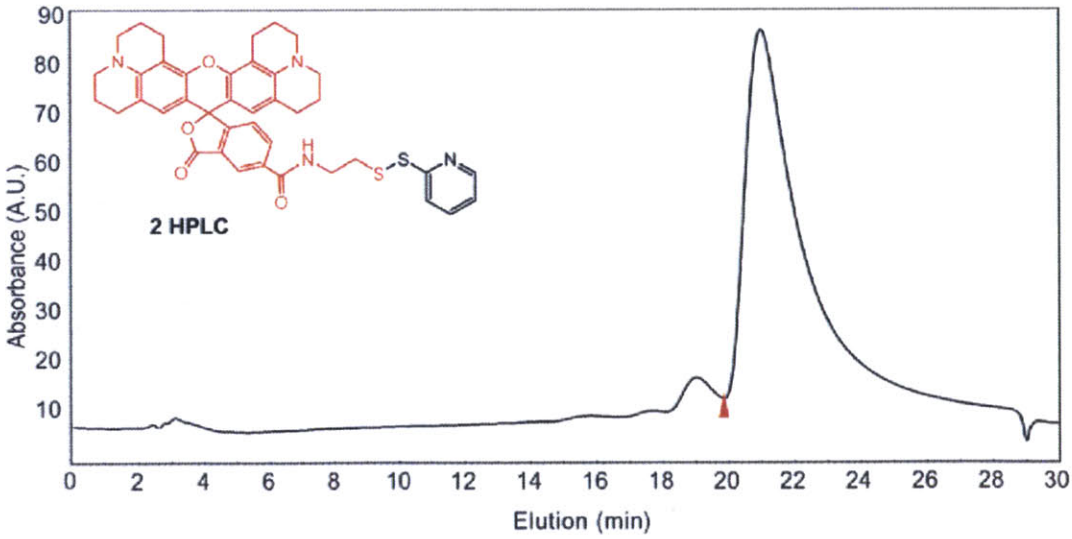

Figure E-3: Purity of compound 2 as measured by HPLC.

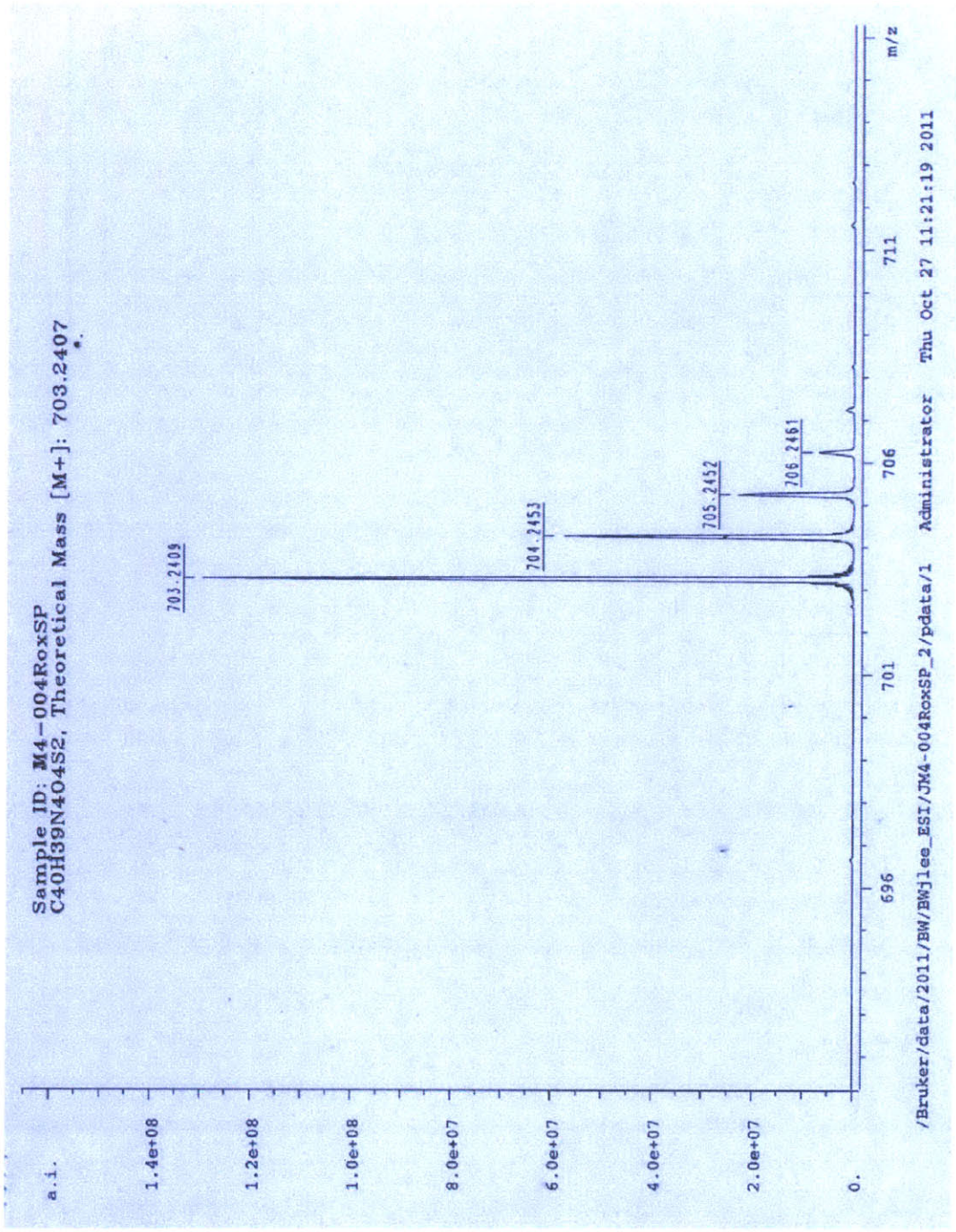

Figure E-4: M/Z spectrum of compound 2.

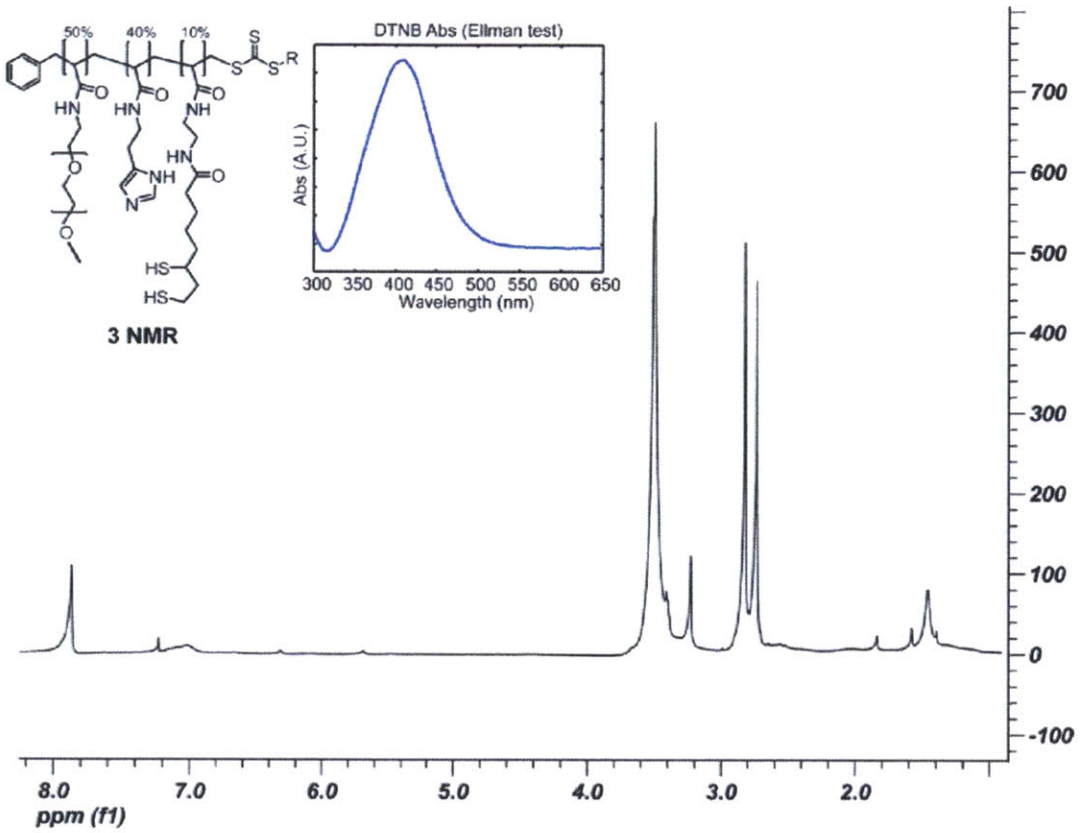

Figure E-5: NMR identification of PIL 3.

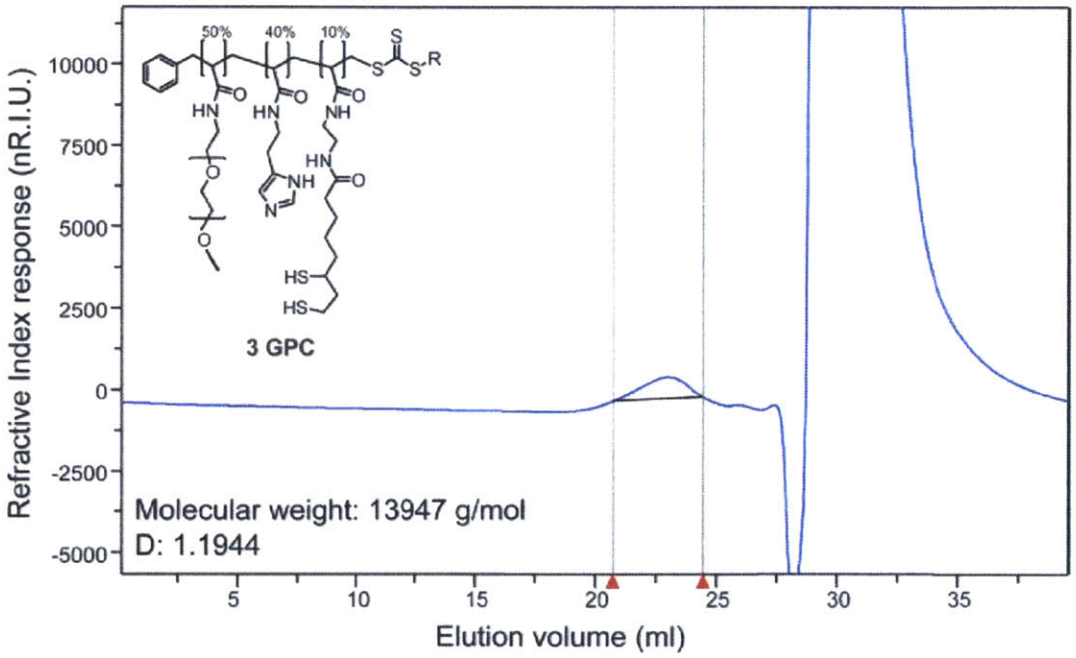

Figure E-6: GPC molecular weight measurement of PIL 3.

Appendix F

In-vitro behavior of QD-S-S-Rox construct

a

Sample	Equivalents Rox added per thiol on PIL	Number of Rox per QD
4-008	1.5x	8
4-014	3.5x	18
4-016	2x	13

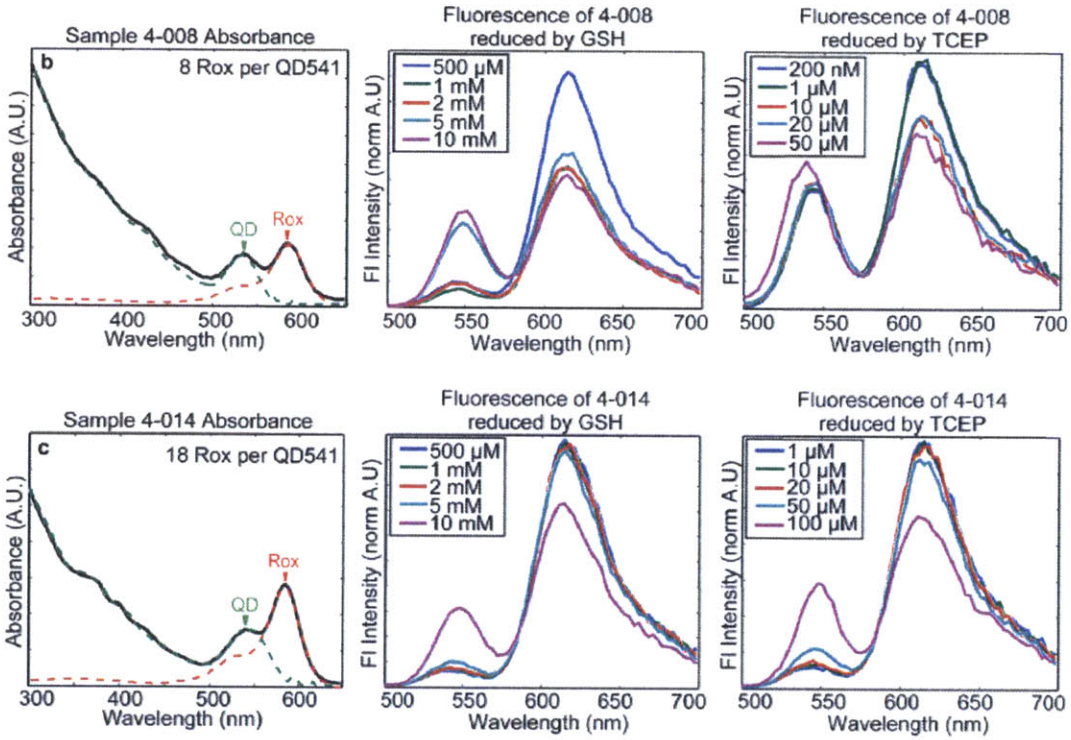

Figure F-1: Reproducibility and stoichiometric control of Rox per QD ratio and disulfide cleavage. **a**, Number of Rox per QD is consistent with reaction stoichiometry. **b** and **c**, absorbance spectrum showing both QD and Rox features, followed by in vitro reduction of the disulfide bond conjugating Rox to QD by glutathione (GSH) and non-thiol based reductant tris(2-carboxyethyl)phosphine (TCEP).

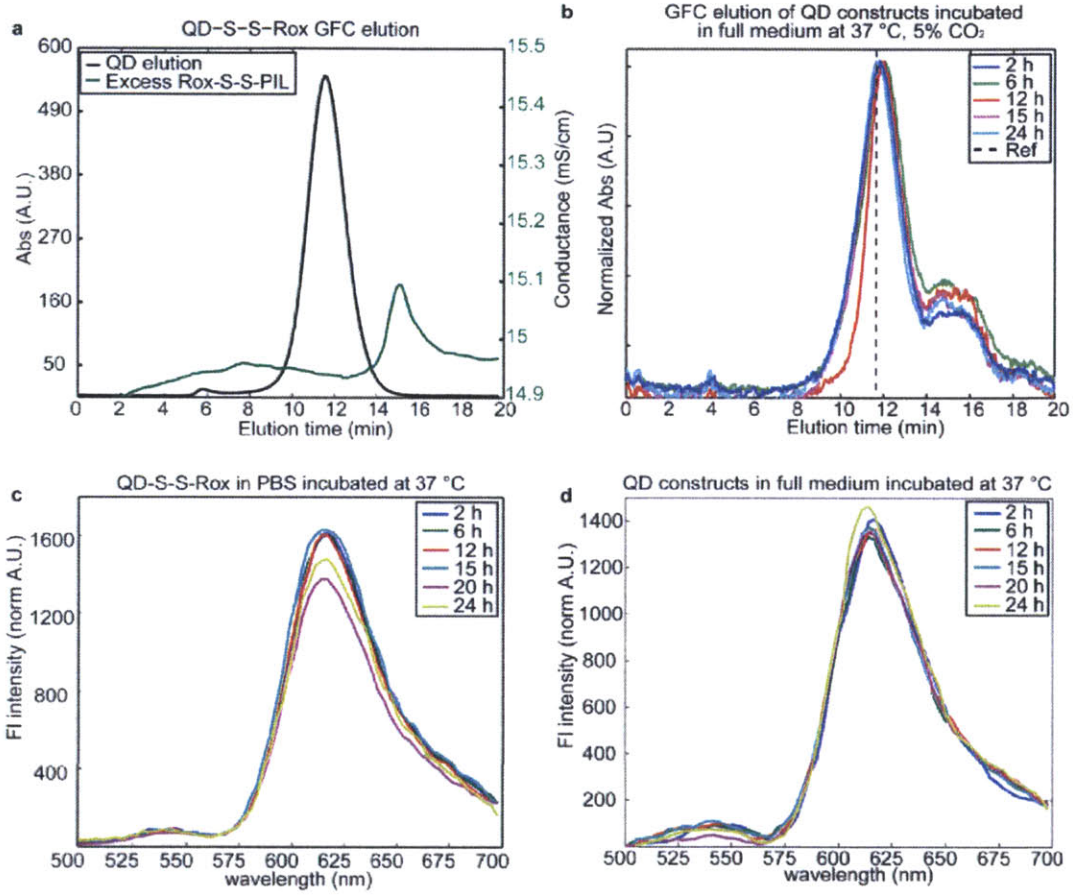

Figure F-2: Stability of QD-S-S-Rox construct against aggregation in full medium at 37 °C (b) and **c**, **d**, cleavage in both PBS and full medium at 37 °C.

Appendix G

Delivery efficiency and cell viability

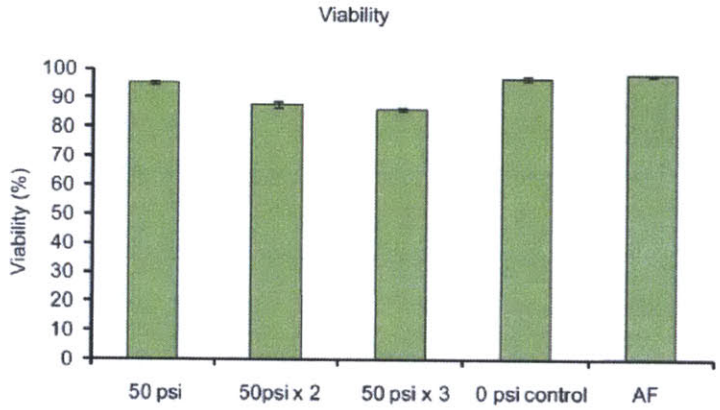

Figure G-1: Viability of HeLa cells upon delivery of plain QD535 by the device, as measured by propidium iodide staining and flow cytometry measurement.

Figure G-2: Far-field view of plain QD535 treated HeLa cells showing increase in cell density from 0 h to 48 h after treatment, demonstrating cell proliferation.

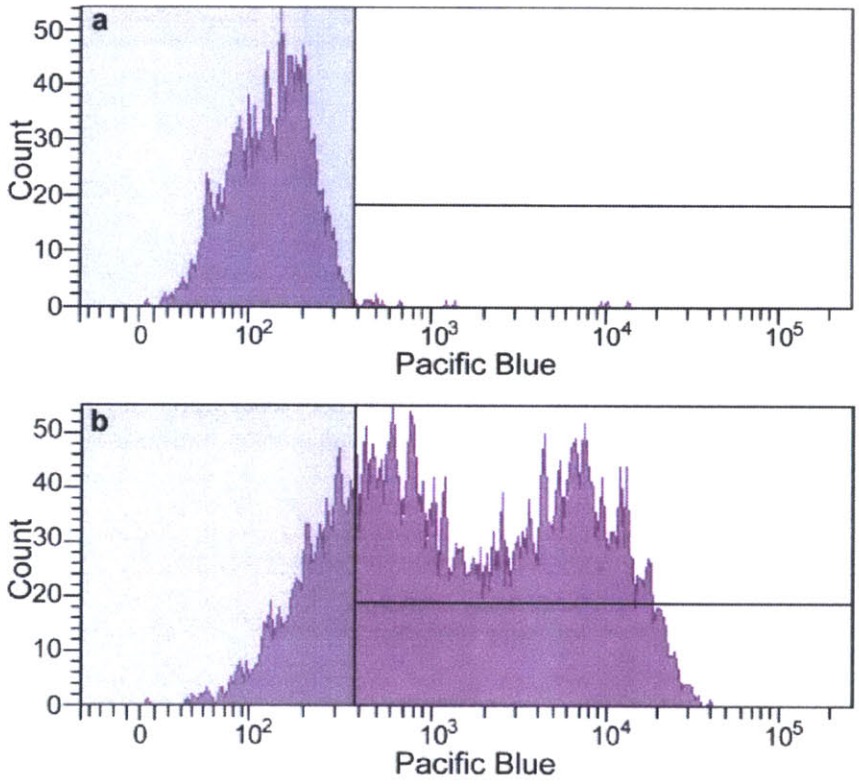

Figure G-3: A demonstration of how we determine the fraction of treated cells amongst the population that have been delivered with fluorescence dyes. **a**, Flow cytometry measurement of the control cell population (incubated with pacific blue dye for 5 minutes at room temperature but untreated by device). **b**, Flow cytometry measurement of cells that have been treated with pacific blue using the device. The grey area represents the level of fluorescence that would not be considered as efficient delivery by the device.

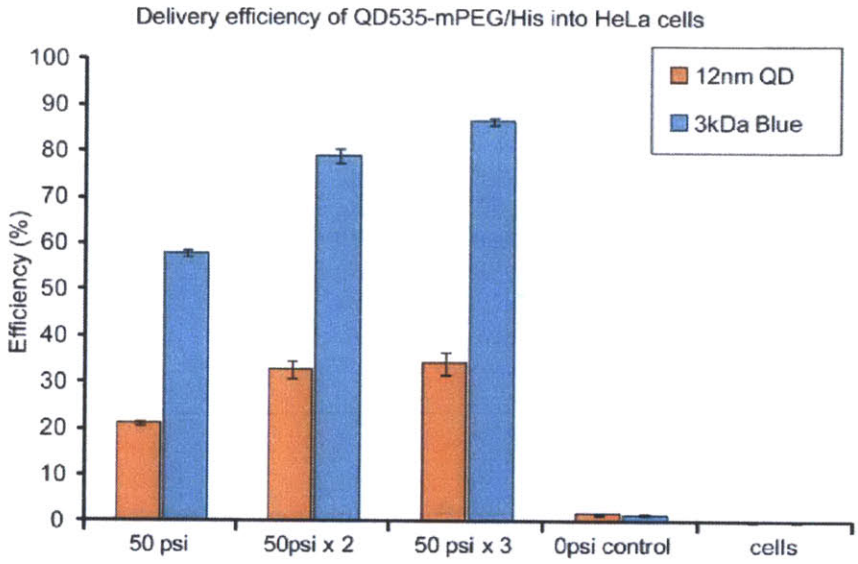

Figure G-4: Delivery efficiency into HeLa cell cytosol upon device treatment with QDs coated with PIL. For delivery efficiency calculation methodology, see figure G-3.

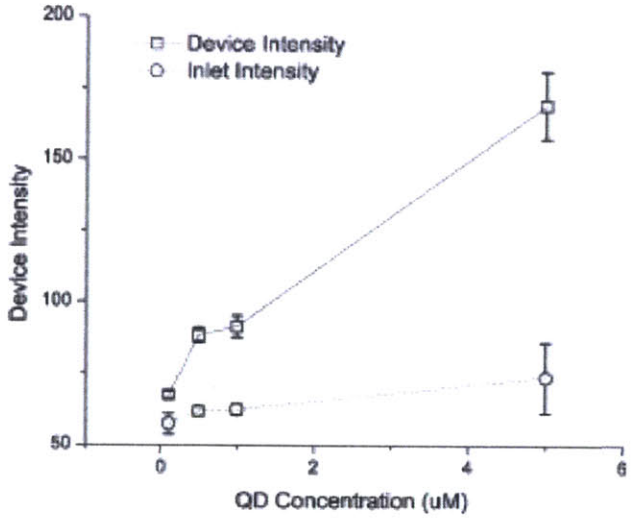

Figure G-5: Delivery efficiency measured at 5 μM, 1 μM, 500 nM and 100 nM QD concentrations during HeLa cell treatment with the microfluidic device. Inlet groups were allowed to sit inside the microfluidic device but were not flown through the channels. Note that delivery concentrations as low as 10 nM were detectable by microscopy, at low enough concentrations to be observed as single molecules.

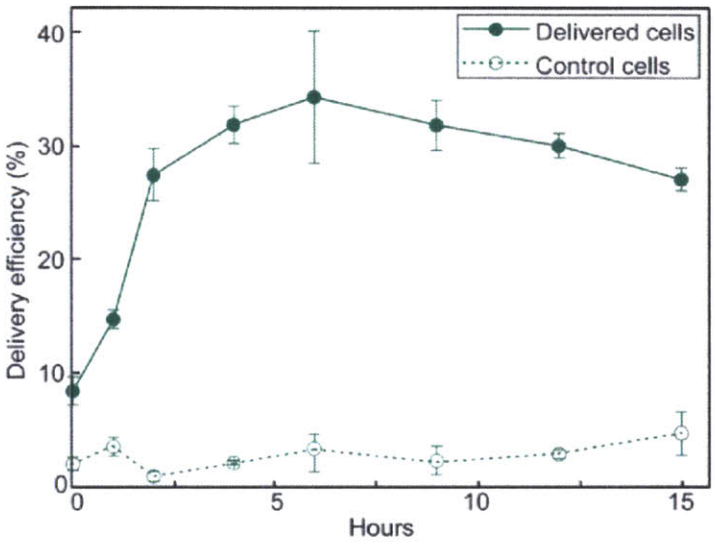

Figure G-6: Delivery efficiency of QD-S-S-Rox construct as measured by tracing the QD fluorescence measured by flow cytometry. The ultimate percentage of the cell population that has QD-S-S-Rox inside the cytosol should be at least 35% according to the plot. This method underestimates cells that have had QD-S-S-Rox delivered, since not all Rox dyes are cleaved from the QD surface.

Appendix H

Delivery Controls

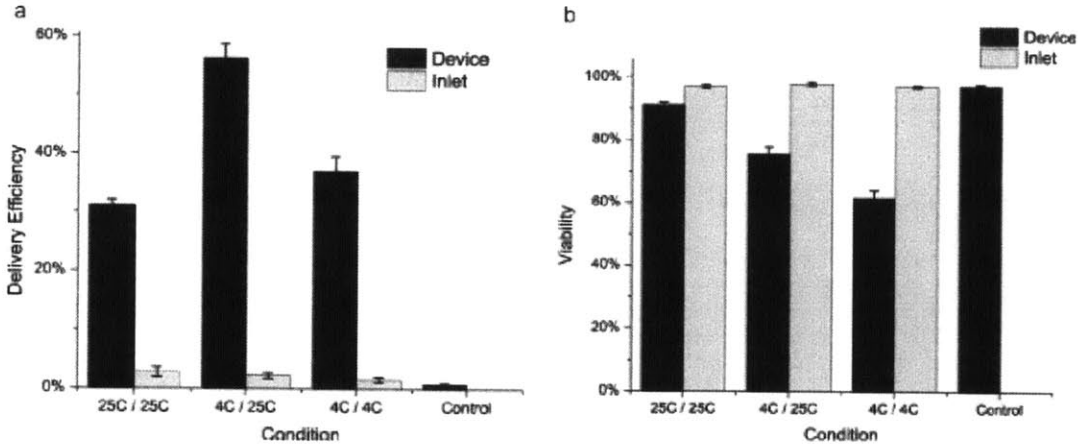

Figure H-1: QDs are delivered into HeLa cells at 4 °C, when biological processes are arrested. Control group was incubated in PBS, and indicate autofluorescence levels. Inlet groups were allowed to sit inside the microfluidic device but were not flown through the channels. **a** Delivery efficiency of QD540 QD fluorescence measured by flow cytometry, and **b** viability of treated, control, and inlet group cells. In these figures, the first number indicates the temperature at which delivery was performed and the second indicates the temperature at which the cells were allowed to recover for 5 minutes prior to washing the QDs.

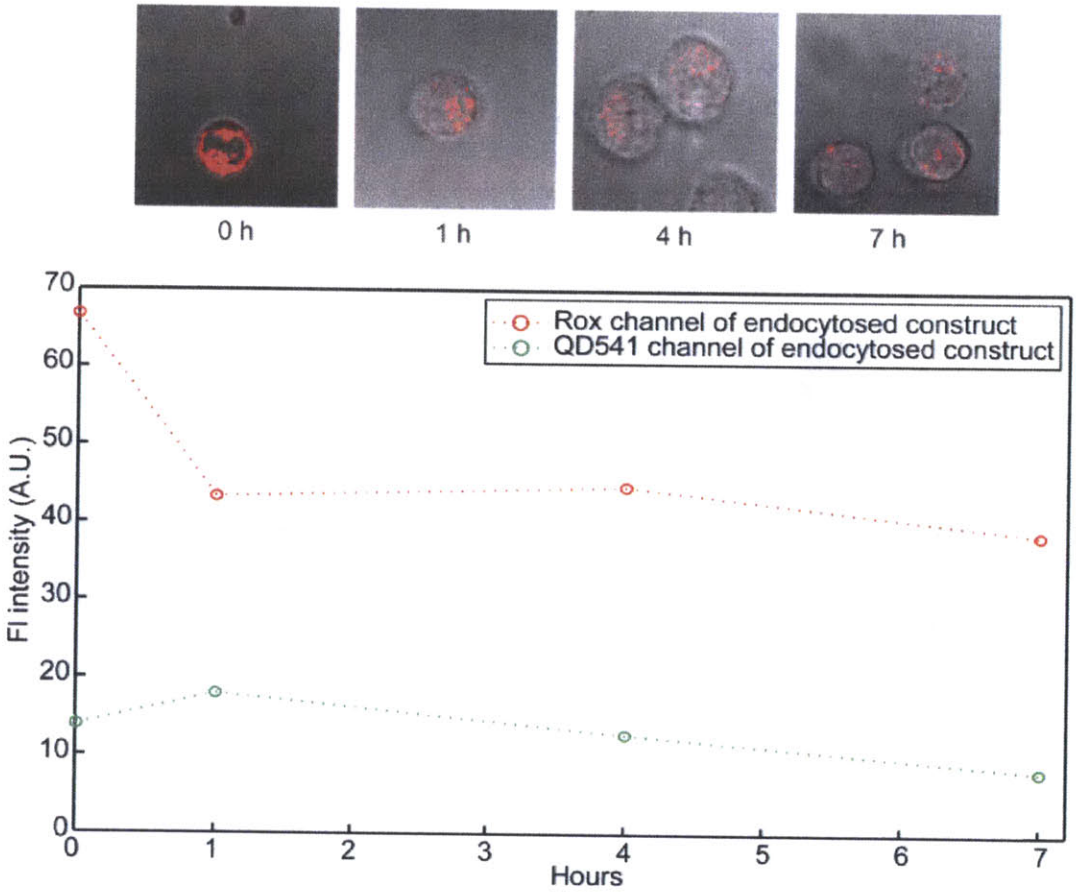

Figure H-2: Fluorescence and transmission overlay images of QD-S-S-Rox constructs that were endocytosed into HeLa cells. Cells were trypsinized and incubated with QD-S-S-Rox for 40 minutes at 37 °C, 5% CO_2.

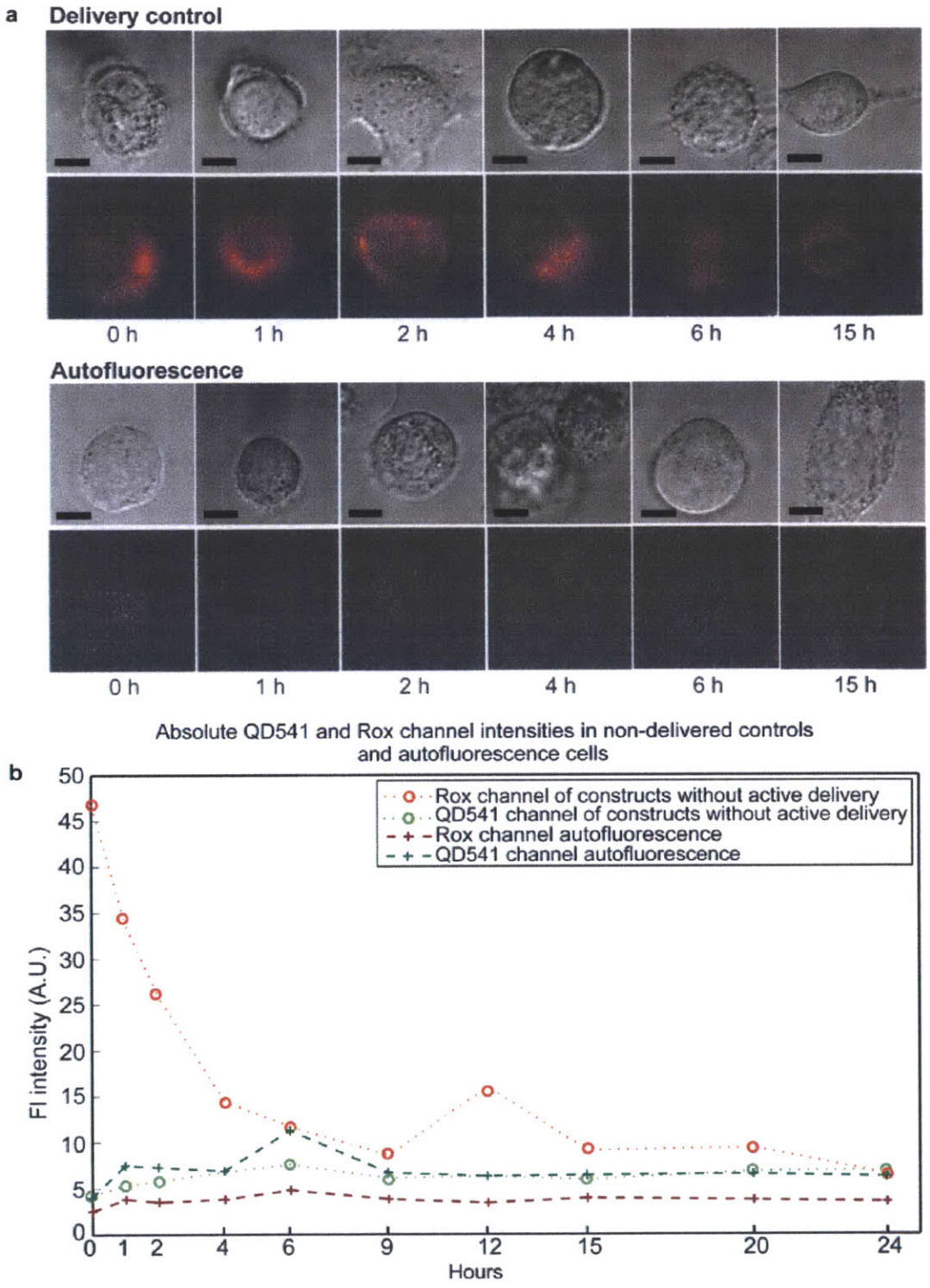

Figure H-3: **a**, Example QD and Rox channel confocal overlay images in the of cells that were incubated, but not delivered, with QD-S-S-Rox (top) and autofluorescence from cells that were completely untreated (bottom). **b**, line graph of average absolute QD and Rox intensities in these cells. Scale bars are 10 μm.

Appendix I

Reproducibility of QD-S-S-Rox Cleavage and Additional Images

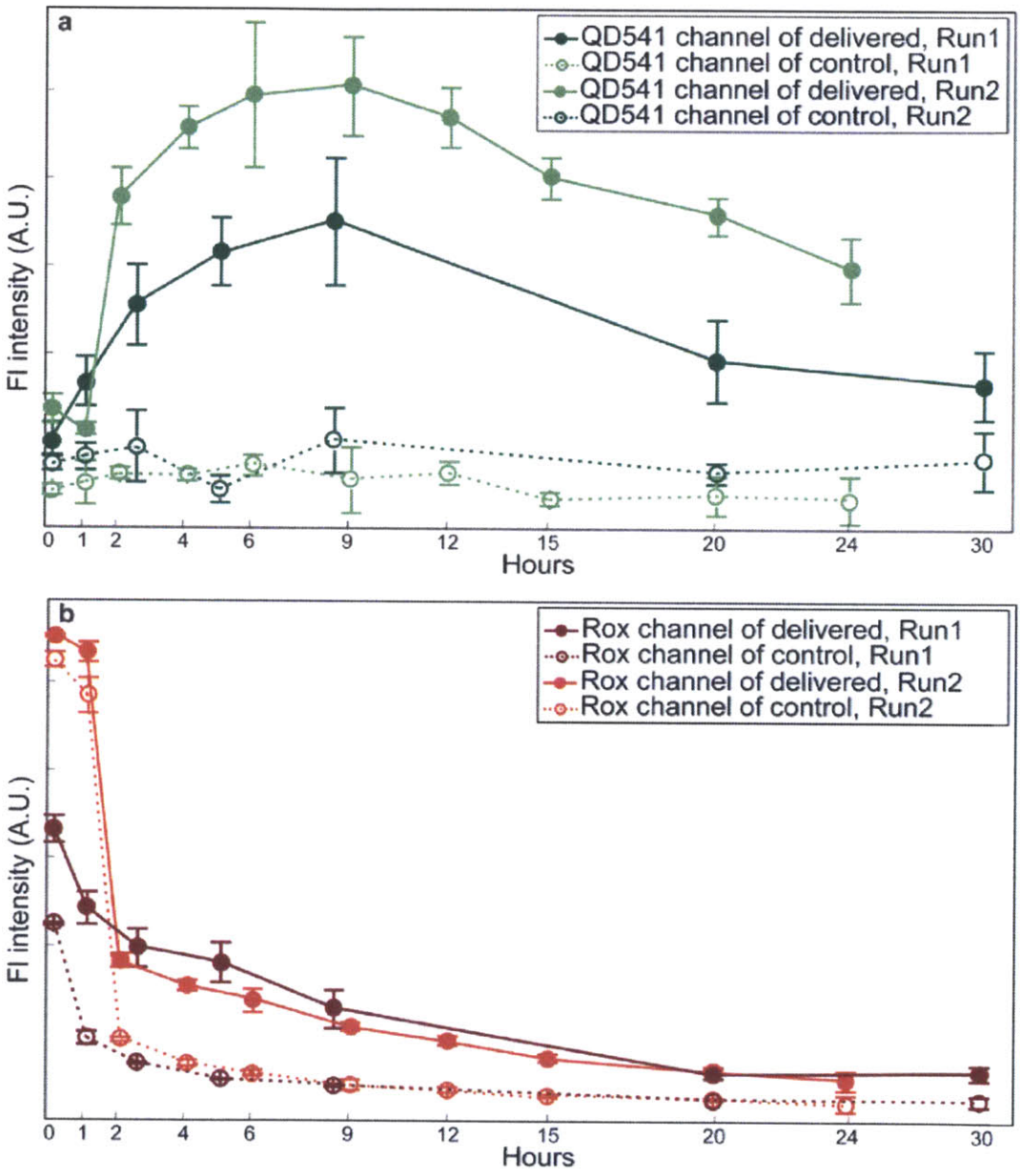

Figure I-1: Reproducibility of cytoplasmic delivery as shown by flow cytometry measurements of different delivery instances of QD-S-S-Rox.

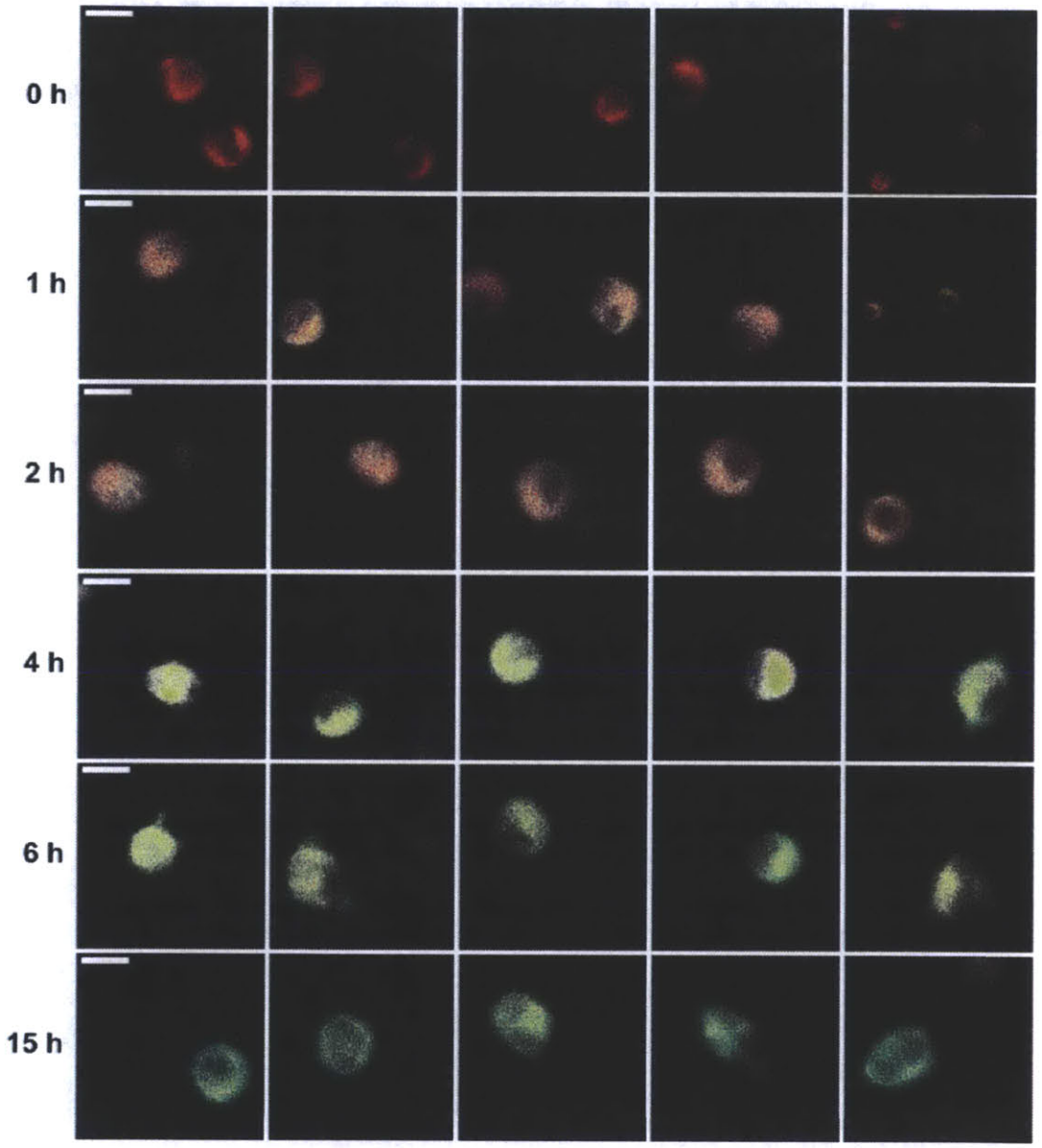

Figure I-2: Additional QD and Rox channel overlay confocal images of HeLa cells that have been delivered with QD-S-S-Rox by the device. Scale bars are 20 μm.

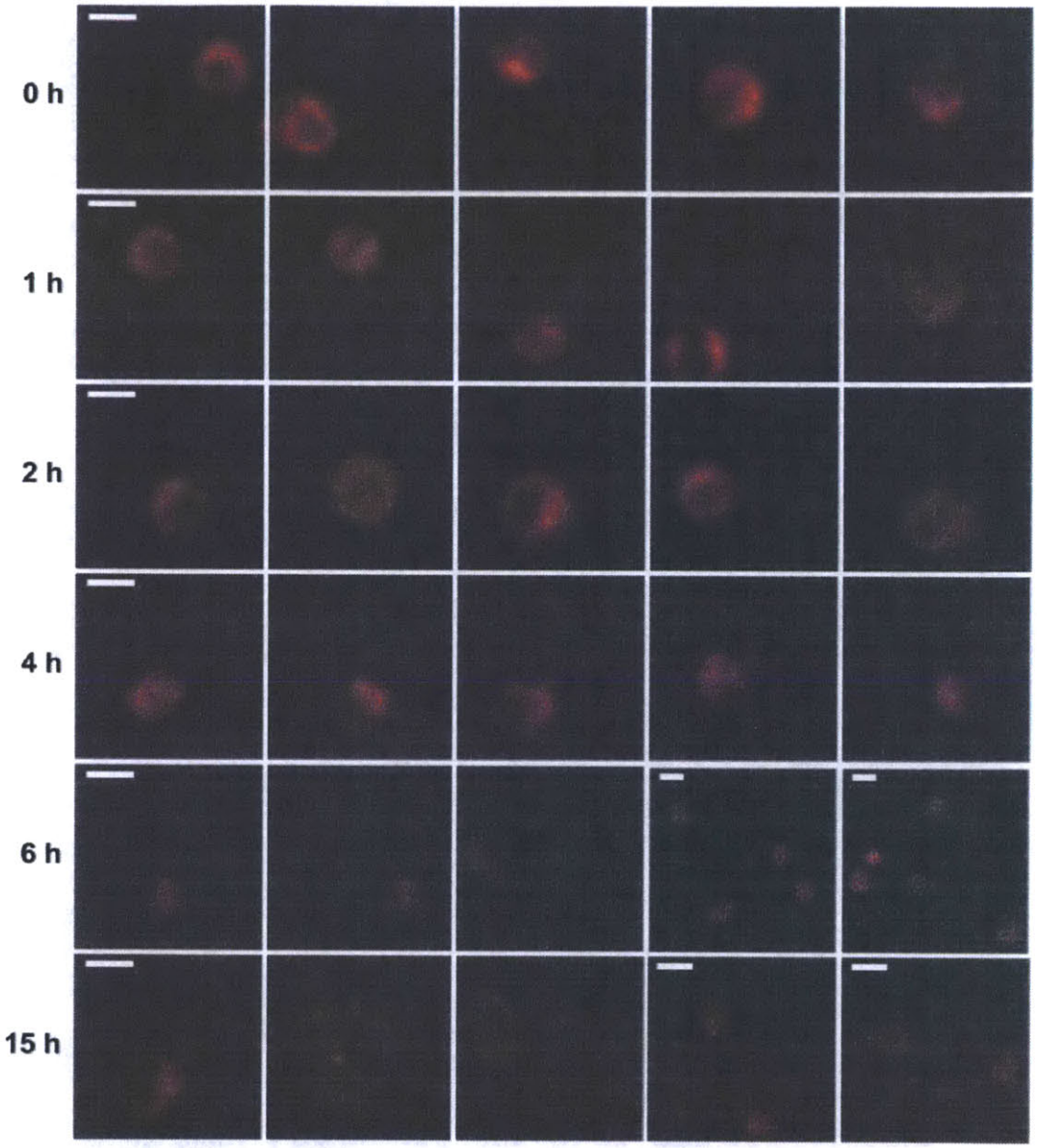

Figure I-3: Additional QD and Rox channel overlay confocal images of HeLa cells that have only been incubated for 5 minutes at room temperature, not delivered, with QD-S-S-Rox. Scale bars are 20 μm.

Appendix J

Tuning the polarity of the Nanoparticle Surface

As mentioned section 4.1, positively charged polymers and cell-penetrating peptides have provided inspiration for numerous nanoparticle designs for cytosolic delivery. However, most attempts including polyethyleneimine [33] and other polymers [34], penetratin [35], HIV-derived Tat-peptide [36], and poly-arginine derivatives [35],[38] have been plagued by a lack of reproducibility: depending on the lab, the nanoparticles stay trapped in endosomes or are able to access the cytoplasm. The mechanism of cytosolic delivery by cell penetrating peptides and polymers is also under debate, as some studies conclude an energy-dependent pathway and others, an energy-independent pathway [39]. Despite the confusion amongst nanoparticle scientists, we experimented with QDs that incorporated elements of viral cell-entry peptides.

Viral cell-penetration research has highlighted arginine residues on cell-penetration peptides as a vital component [40]. Some report a strong association between arginine groups with negatively charged phospholipids and heparin sulfates, even when compared to lysines [41]. Following precedents of polyarginine-mediated cellular delivery of nanoparticles [42], the guanidine group, the functional group on arginine that gives the amino acid positive charge, was incorporated into PIL. Polymer composition was varied from ~2 guanidine per QD to about 8 guanidine groups per PIL. There was clearly increased interaction of QDs with the HeLa cell membrane even for

PILs with 2 guanidines per PIL, despite having a close to zero charge as measured by zeta potential. Preliminary data showed that these guanidine-functionalized QDs are isolated in endosomal compartments and had some binding to glass surface. No evidence of endosomal escape was observed. Therefore, we concluded that arginine does increase nanoparticle-membrane interactions, but that a different driving force is needed in order for QDs to cross the lipid bilayer solely based on surface chemical properties.

It has been shown that non-disruptive delivery of metal nanoparticles is also possible: among the most striking are of oligonucleotide-coated gold particles and of amphiphilic gold particles [3],[43]. These works inspired us to attempt tuning the QD ligands to verify whether amphiphilic ligands can result in cytoplasmic delivery. Interestingly, Kloepfer et al. succeeded in embedding QDs into an artificial phospholipid bilayer, indicating the potential toward tuning the ligands so that QDs could do the same in cellular membranes and act as a stable sensor [44]. Thus, we hoped to see either/both incorporation of QDs within the lipid bilayer (Fig. J-1a) or/and their delivery into the cytoplasm (Fig. J-1b).

J.1 QDs as a Voltage Sensor in Neurology

Concurrent with the surge in fluorescence microscopy, voltage sensitive dye imaging (VSDI) emerged as a non-disruptive technique that could sample a much larger number of cells [45]. Before, neuron action potential responses to environmental stimuli were directly quantified using a microelectrode, which limited the number of cells that could be simultaneously sampled and was detrimental to cell health [46]. Commercial voltage sensitive fluorescent dyes are charged conjugated-hydrocarbon fluorophores that tend to fluoresce only in hydrophobic environments. A membrane electric potential on the order of 100 kV/cm induces a change in the electronic structure depending on both the polarity and the polarization of these dyes, shifting their optical characteristics such as emission, absorption, and birefringence. For example, Invitrogens ANEP series potential-dependent fluorescence intensity when localized to

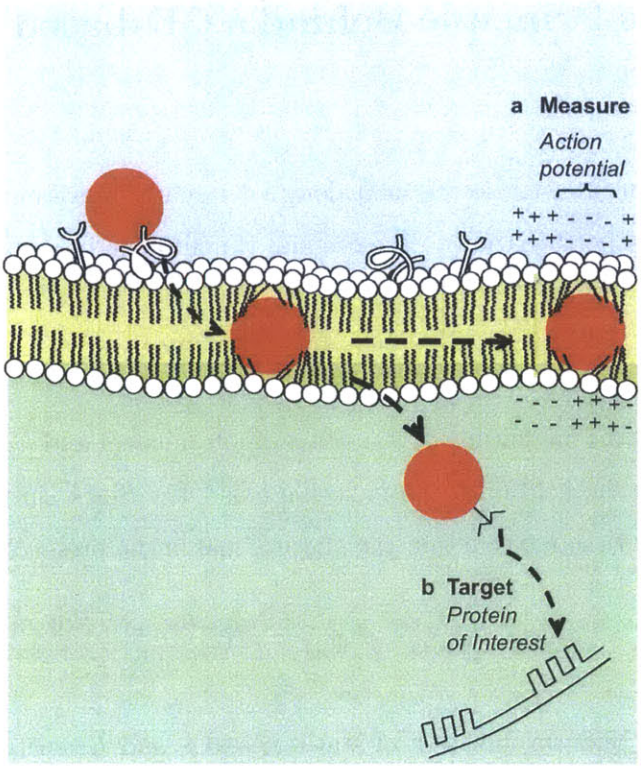

Figure J-1: The two possible localizations of QDs coated with amphiphilic ligands. **a**, QD may become embedded in between the phospholipid bilayer, opening the possibility for voltage sensors. **b**, QD may be released into the cytoplasmic face of the lipid bilayer, achieving access to cytoplasmic proteins of interest.

the membrane. This Stark effect has been unequivocally proven to exist also in QDs [47], [48]. For organic dyes, photobleaching severely limits long-term optical recording of membrane potential and a higher signal-to- noise ratio is desirable since the field across the cell membrane causes only a ~10% change for some dyes optical properties [46]. Therefore, membrane-inserted QDs would be particularly useful for their photostability and high QY. In addition, for nerve studies in vivo, the large absorption coefficient and broad excitation can really reduce the effects of photon attenuation in deeper tissue.

J.2 The Principle Behind a QD-based Voltage Sensor

The effect of an external electric field along a designated z-axis on polarizable molecules is derived by a perturbation to the original Hamiltonian in an unbiased field:

$$H = H_0 - erFcos\theta \tag{J.1}$$

where er is the magnitude of transition dipole moment and $Fcos\theta$ is the projection of applied electric field onto the molecule axis. The Stark shift is the difference in energy states of the molecules in the absence and in the presence of the electric field:

$$\Delta E = \langle \Psi_n | e\vec{r} \cdot \vec{F} | \Psi_n \rangle + \frac{\Sigma_{i \neq n} |\langle \Psi_n | e\vec{r} \cdot \vec{F} | \Psi_n \rangle|^2}{E_n - E_i} \tag{J.2}$$

where Ψ is the wavefunction of states n and i, and E, energy of states n and i. As can be seen, the magnitude of the shift is dependent on the applied electric field and the intrinsic characteristics of the molecule. It is much more relevant to think of the Stark effect in chemical terms:

$$\Delta E = \mu F + \frac{1}{2}\alpha F^2 \tag{J.3}$$

Here, the first term, which shows linear dependence on the electric field, is determined by the excited state dipole, and the second term, which shows quadratic dependence on the electric field, is determined by the polarizability of the molecule. For single QD Stark shifts, both linear and quadratic dependence on the electric field could be extracted. The linear portion, however, is unobservable for averaged single QDs because the dipoles tend to cancel each other out [49]. By virtue of its mesoscopic character, quantum-confined systems enable sensing of larger electric fields than in the bulk. Much stronger electric fields can be applied to quantum-confined systems without completely pulling apart the hole and the electron because the exciton is physically confined. On the other hand, the larger volume of QDs in comparison

to single molecules gives the nanocrystals much larger polarizability. Fused benzene ring molecules, such as anthracene, has a polarizability on the order of $\sim 25\mathring{A}^3$, as opposed to that on the order of $\sim$2x10$^5\mathring{A}^3$ in 5.3 nm diameter QDs [49]. Lupton et al. has already demonstrated that CdSe/CdS nanorod Stark shift can be large enough (30meV) to influence the presence of FRET between donor nanocrystal and acceptor dye within the Forster radius at liquid nitrogen temperature [48]. Single QD Stark shifts have been observed to be as much as 70 meV by Empedocles, on the order of room-temperature single-QD linewidth [49]. These experiments were done by applying 50-375 kV/cm, which is comparable to cellular membrane potential changes during neuron activation ($\sim$100s kV/cm) [50].

J.3 Results

Work by Verma et al. [3] inspired an amphiphilic approach towards cytoplasmic delivery. Hydrocarbon chains were added to the PIL, along with PEG or carboxylic acid-terminated PEG that gave QDs aqueous solubility. The hydrocarbon chains may help create a hydrophobic driving force for QDs to temporarily disrupt lipid packing and intercalate between the lipid bilayer. The degree of PIL hydrophobicity was altered by changing both the length of hydrocarbon chains and the number of hydrocarbon monomers on the polymer. The length of the hydrocarbon chain was optimized to decyl groups, and the number of hydrophobic monomers, 50% and 60% of the monomers on the PIL. Then, QDs ligand exchanged with these polymers were tested for their potential for cell membrane localization by mixing the QDs with a membrane-localizing dye. The binding between QD and this membrane-localizing dye can be monitored via FRET. Thus, a high FRET signal suggests that a particular polymer formulation is a promising candidate for delivering QDs within the cell membrane (Fig. J-2). When treated with these QDs, the cellular membrane appeared to be stained with fluorescence. The solvent mixture, solution volume and concentration can be modified so that membrane staining is faster and brighter. Ultimately, localization between the lipid bilayer has to be ascertained through TEM.

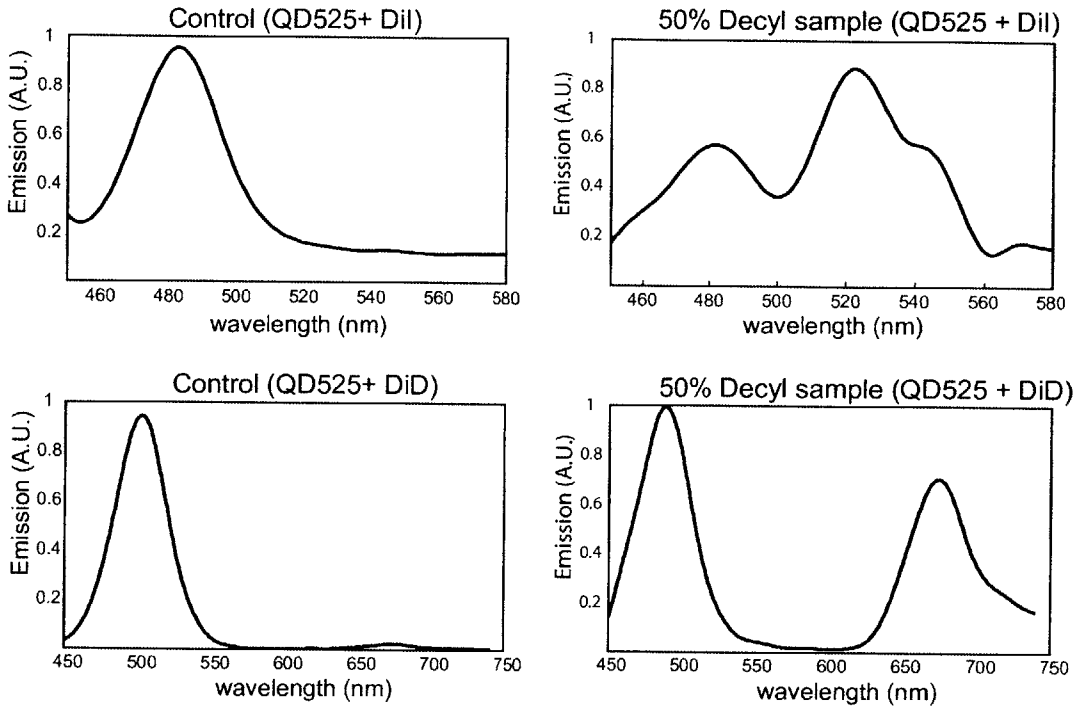

Figure J-2: FRET from a QD donor, coated with amphiphilic ligands containing 50% (top) or 60% (bottom) decyl groups on the PIL monomers, to a FRET acceptor cell membrane dye. Control QDs coated with PEG groups do not show FRET because cell membrane dyes are unable to interact favorably with the QD surface.

In addition, there are reports of PEG changing membrane curvature at close proximity [51], [52]. Upon sweeping different proportions of guanidine-terminated PEG monomer and of hydrophobic monomers, constructs coated with 20% guanidine-PEG/50% decyl/30% imidazole PIL (Fig. J-3) appeared to stain the cell membrane. Due to limitations in time and facilities, we could not obtain clear TEM images. However, as an indirect evidence to discern whether the QDs are non-specifically bound to the surface of the cell or have been able to insert itself within the lipid bilayer, we did a quenching study. In this experiment, cells were incubated with the QD constructs to result in membrane staining. These cells were then immersed in 1-100 μM Ca^{2+} solution for 1-5 minutes. Since treatment with Ca-ions are known to irreversibly quench QDs, we hypothesized that the QD-constructs would be quenched if they were bound to the cell surface but stay fluorescent if protected within the

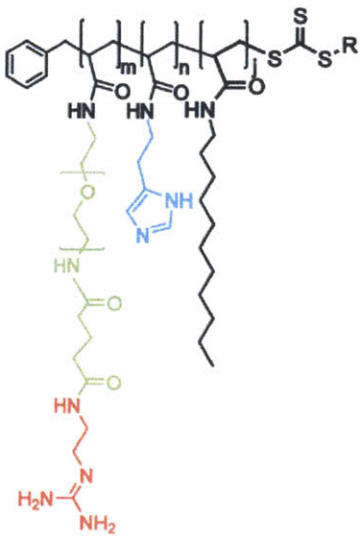

Figure J-3: Schematic of 20% guanidine-PEG/50% decyl/30% imidazole PIL

non-polar environment of the lipid bilayer. The constructs were indeed found to stay brighter than the controls (both non-sticky, PEG-coated QDs and 30% amino-PEG/40% methoxy-PEG/30% imidazole PIL-coated QDs that are known to bind non-specifically onto the cell surface) upon Ca-ion treatment (Fig. J-4). However, due to a lack of rigorous control the results were considered inconclusive.

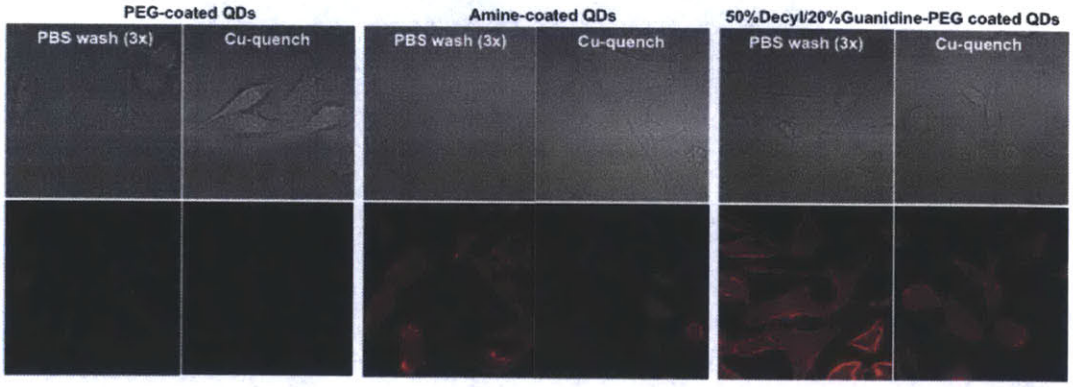

Figure J-4: Comparison of the extent of photoluminescence quenching by Cu ions for: non-sticky PEG-coated QDs (left), amine-coated QDs that are non-specifically bound to the cell surface (middle), and QDs containing cell membrane binding elements along with hydrocarbon chains (right)

A second indirect study was done on the cell surface to further ascertain how

closely the amphiphilic, guanidine-presenting QDs interact with the actual lipid bilayer. In this experiment, InAs QDs emitting at 750 nm were coated with either 20% guanidine-PEG/50% decyl/30% imidazole PIL or 30% amino-PEG/40% methoxy-PEG/30% imidazole PIL. These QDs were then allowed to interact with HeLa cells with membranes pre-stained using a cell membrane dye, DiR, whose absorbance spectrum allows it to act as a FRET acceptor to QD750. The hypothesis here was that, FRET will be observed only if the QDs are able to associate very closely with the lipid bilayer, where the DiR dye is known to associate in between the lipids. As shown in figure J-5, a double-staining of DiR and amphiphilic QDs containing guanidine resulted in FRET emission of DiR, whereas a co-staining of DiR and amine-coated QDs did not.

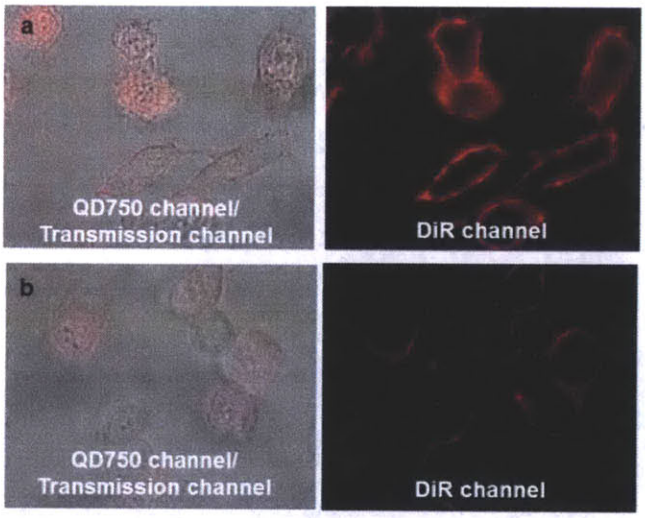

Figure J-5: The presence of FRET between the QD750 donor and the DiR acceptor, on HeLa cell membranes. **a**, QD750 that had been coated with 20% guanidine-PEG/50% decyl/30% imidazole PIL is able to associate close enough with the lipid bilayer to allow FRET to DiR dye, which is known to wedge itself between lipid molecules. Left, an overlay of QD750 emission and transmission images, right, emission detected in the DiR channel. **b**, QD750 coated with 30% amino-PEG/40% methoxy-PEG/30% imidazole PIL is known to non-specifically bind to the cell surface, most likely at the outer rims of the cell. Left, an overlay of QD750 emission and transmission images, right, emission detected in the DiR channel.

In conclusion, the presence of both hydrophobic groups and membrane-directing groups attached to PEG may make it possible for nanoparticles to interact very

closely with the cell lipid bilayer. However, there are many questions as to how the nanoparticles actually interact with the lipids on the membrane because we cannot be absolutely sure that the QDs are in fact settled in between the two lipid layers of the cell membrane. More rigorous control and fluorescence tracking, along with TEM imaging are needed in order to ascertain where the QD is localized.

Bibliography

[1] Howarth, M.; Liu, W.; Puthenveetil, S.; Zheng, Y.; Marshall, L.F.; Schmidt, M.M.; Wittrup, K.D.; Bawendi, M.G.; Ting, A.Y. *Nature Methods* **2008**, 5, 397-399.

[2] Resch-Genger, U.; Grabolle, M.; Cavaliere-Jaricot, S.; Nitschke, R.; Nann, T. *Nature Methods* **2008**, 5, 763-775.

[3] Verma, A.; Uzun, O.; Hu, Y.; Hu, Y.; Han, H.; Watson, N.; Chen, S.; Irvine D.J.; Stellacci, F. *Nature Materials* **2008**, 7, 588.

[4] Yum, K.; Na, S.; Xiang, Y.; Wang, N.; Yu, M. *Nano Letters* **2009**, 9, 2193-2198.

[5] Boukany, P.E.; Morss, A.; Liao, W.; Henslee, B.; Jung, H.; Yu, B.; Wang, X.; Wu, Y.; Li, L.; Gao, K.; Hu, X.; Hemminger, O.; Lu, W.; Lafyatis, G.P.; Lee, L.J. *Nature Nanotechnology* **2011**, 6, 747-754.

[6] Smith, A.M.; Wen, M.M.; Nie, S. Biochem (Lond) **2010**, 3, 1-12.

[7] Biju, V.; Itoh T.; Ishikawa, M. *Chem. Soc. Rev.* **2010**, 39, 3031-3056.

[8] Yoo, J.S.; Kim, H.B.; Bang, J.; Kim, S.; Ahn, S.; Lee, B.C.; Soh, K.S. *Mol Imaging Biol* **2011**, 13, 471-480.

[9] Delehanty, J.B.; Bradburne, C.E.; Boeneman, K.; Susumu, K.; Farrell D, Mei BC, Blanco-Canosa JB, Dawson G, Dawson PE, Mattoussi H, Medintz IL. *Integr. Biol.* **2010**, 2, 265-277.

[10] Bruchez, M.P.; Hotz, C.Z. Quantum dots: applications in biology.; Humana Press: Totowa, **2007**.

[11] Courty, S.; Luccardini, C.; Yohanns, B.; Cappello, G.; Dahan, M. *Nano Lett.* **2006**, 6, 1491-1495.

[12] Fuller, J.E.; Zugates, G.T.; Ferreira, L.S.; Ow, H.S.; Nguyen, N.N.; Wiesner, U.B.; Langer, R.S. *Biomaterials* **2008**, 29, 1526-1532.

[13] Hu, Y.; Atukorale, P.U.; Lu, J.J.; Moon, J.J.; Um, S.H.; Cho, E.C.; Wang, Y.; Chen, J.; Irvine, D.J. *Biomacromolecules* **2009**, 10, 756-765.

[14] Kim, B.Y.S.; Jiang, W.; Oreopoulos, J.; Yip, C.M.; Rutka, J.T.; Chan, W.C.W. *Nano Letters* **2008**, 8, 3887-3892.

[15] Bayles, A.R.; Chahal, H.A.; Chahal, D.S.; Goldbeck, C.P.; Cohen, B.E.; Helms, B.A. *Nano Letters* **2010**, 10, 4086-4092.

[16] Liu, B.R.; Huang, Y.; Winiarz, J.G.; Chiang, H.; Lee, H. *Biomaterials* **2011**, 32, 3520-3537.

[17] Dudu, V.; Ramcharan, M.; Gilchrist, M.L.; Holland, E.C.; Vazquez, M. *J Nanosci Nanotechnol* **2008**, 8, 2293-2300.

[18] Dhar, S.; Daniel, W. L.; Giljohann, D. A.; Mirkin, C. A.; Lippard, S. J. *JACS* textbf2009, 131, 1465214653.

[19] Jaiswal, J.K.; Mattoussi, J.; H.; Mauro, M.; Simon, S.M. *Nature Biotech* **2002**, 21, 47-51.

[20] Medintz, I. L.; Uyeda, H. T.; Goldman, E. R.; Mattoussi, H. *Nature Materials* **2005**, 4, 435-446.

[21] Patterson, G.; Davidson, M.; Manley S.; Lippincott-Schwartz, *J. Rev. Phys. Chem.* **2010**, 61, 34567.

[22] Zelman-Femiak, M.; Wang, K.; Gromova, K.; Knaus, P.; Harms, G.S. Biotechniques **2010**, 49, 574-579.

[23] Sharei, A.; Zoldan, J.; Adamo, A.; Sim, W.Y.; Cho, N.; Jackson, E.; Mao, S.; Schneider, S.; Han, M.; Lytton-Jean, A.; Basto, P.A.; Jhunjhunwala, S.; Lee, J.; Heller, D.A.; Kang, J.W.; Watson, N.; Kim, K.; Anderson, D.G.; Langer, R.; Jensen, K.F. Submitted.

[24] Liu, W.; Greytak, A.B.; Lee, J.; Wong, C.R.; Park, J.; Marshall, L.F.; Jian, W.; Curtin, P.N.; Ting, A.Y.; Nocera, D.G.; Fukumura, D.; Jain, R.K.; Bawendi, M.G. *JACS* **2010**, 132, 472-483.

[25] Aw, T.Y. *News in Physiological sciences* **2003**, 5, 201-204.

[26] Jones, D.P. *Methods Enzymol* **2002**, 348, 93-112.

[27] Agarwal, A.; Zudans, I.; Weber, E.A.; Olofsson, J.; Orwar, O.; Weber, S.G. Anal. Chem. 2007, 79, 3589-3596.

[28] Hong, S.; Leroueil, P.R.; Janus, E.K.; Peters, J.L.; Kober, M.M.; Islam, M.T.; Orr, B.G.; Baker Jr, J.R.; Banaszak Holl, M.M. *Bioconjugate Chem* **2006**, 17, 728-734.

[29] Pinaud, F.; Clarke, S.; Sittner, A.; Dahan, M. *Nature Methods* **2010**, 7, 275 - 285.

[30] Chakravarty, P.; Qian, Q.; El-Sayed, M.A.; Prausnitz, M.R. *Nat Nanotechnol.* **2010**, 8, 607-611.

[31] Peng, Z. A.; Peng, X. *J. Am. Chem. Soc.* **2001**, 123, 183-184.

[32] Leatherdale, C. A.; Woo, W. K.; Mikulec, F. V.; Bawendi, M. G. J. Phys. Chem. B. 2002, 106, 7619-7622.

[33] Duan, H. and S. Nie, Cell-Penetrating Quantum Dots Based on Multivalent and Endosome-Disrupting Surface Coatings. *JACS* **2007**, 129(11): p. 3333-3338.

[34] Fuller, J.E., et al., Intracellular delivery of core-shell fluorescent silica nanoparticles. *Biomaterials*, 2008. 29(10): p. 1526- 1532.

[35] Philipp, A., et al., Hydrophobically Modified Oligoethylenimines as Highly Efficient Transfection Agents for siRNA Delivery. *Bioconjugate Chemistry* **2009**, 20(11): p. 2055-2061.

[36] Thoren, P.E.G., et al., Uptake of analogs of penetratin, Tat(48-60) and oligoarginine in live cells. *Biochemical and Biophysical Research Communications* **2003**, 307(1): p. 100-107.

[37] Wei, Y., et al., Surface Coating Directed Cellular Delivery of TAT-Functionalized Quantum Dots. *Bioconjugate Chemistry* **2009**, 20(9): p. 1752-1758.

[38] Zaro, J.L., et al., Nuclear Localization of Cell-Penetrating Peptides Is Dependent on Endocytosis Rather Than Cytosolic Delivery in CHO Cells. *Molecular Pharmaceutics* **2009**, 6(2): p. 337-344.

[39] Thoren, P.E.G., et al., Membrane destabilizing properties of cell-penetrating peptides. *Biophysical Chemistry* **2005**, 114(2- 3): p. 169-179.

[40] Calnan, B., et al., Analysis of arginine-rich peptides from the HIV Tat protein reveals unusual features of RNA-protein recognition. *Genes and Development* **1991**, 5: p. 201-210.

[41] Fuchs, S.M. and R.T. Raines, Pathway for Polyarginine Entry into Mammalian Cells. *Biochemistry* **2004**, 43(9): p. 2438- 2444.

[42] Delehanty, J.B., et al., Self-Assembled Quantum Dot Peptide Bioconjugates for Selective Intracellular Delivery. *Bioconjugate Chemistry* **2006**, 17(4): p. 920-927.

[43] Giljohann, D.A., et al., Oligonucleotide Loading Determines Cellular Uptake of DNA-Modified Gold Nanoparticles. *Nano Letters* **2007**, 7(12): p. 3818-3821.

[44] Kloepfer, J.A., N. Cohen, and J.L. Nadeau, FRET between CdSe Quantum Dots in Lipid Vesicles and Water- and Lipid- soluble Dyes. *The Journal of Physical Chemistry B* **2004**, 108(44): p. 17042-17049.

[45] Chemla, S. and F. Chavane, Voltage-sensitive dye imaging: Technique review and models. *Journal of Physiology-Paris* 104(1-2): p. 40-50.

[46] Grinvald, A. and R. Hildesheim, VSDI: a new era in functional imaging of cortical dynamics. *Nat Rev Neurosci* **2004**,5(11):p. 874-885.

[47] Sacra, A., Ph.D. Thesis. Department of Chemistry, Massachusetts Institute of Technology, 1996.

[48] Becker, K., et al., Electrical control of Forster energy transfer. *Nat Mater* **2006**, 5(10): p. 777-781.

[49] Empedocles, S.A. and M.G. Bawendi, Quantum-Confined Stark Effect in Single CdSe Nanocrystallite Quantum Dots. *Science* **1997**, 278(5346): p. 2114-2117.

[50] Barnett, M. and P. Larkman, How to understand it: The action potential. *Practical Neurology* **2007**, 7: p. 192-197.

[51] Lentz, B., PEG as a tool to gain insight into membrane fusion. *European Biophysics Journal* **2007**, 36(4): p. 315-326.

[52] Malinin, V.S., P. Frederik, and B.R. Lentz, Osmotic and Curvature Stress Affect PEG-Induced Fusion of Lipid Vesicles but Not Mixing of Their Lipids. *Biophysical Journal* **2002**, 82(4): p. 2090-2100.

Acknowledgments

"God will illuminate your path."
- My mother

My five years at MIT have been incredibly seminal in my growth, not in the least making a believer out of an infidel. My mother's wise words turned out to be true: the countless failures, the many late nights, the seemingly infinite number of stupid mistakes..., all culminated in a body of work that somehow is worthy of awarding me a Ph.D. All of this would have been impossible without the following persons: Moungi G. Bawendi, our fearless leader who has the gentlest way of telling us something is bullshit or brilliant; Jose M. Cordero, who has become my partner in crime and the chattiest labmate I am happy to talk to; Raoul Correa, Darcy Wanger, and Jian Cui, who joined this blessed group with me. Without them I would have felt incredibly alone. Wenhao Liu, Peter Allen, Euan Kay, Gautham Nair, Lisa Marshall, Zoran Popovic, Russ Jensen, Dan Harris, and Brian Walker all have been good friends to me and taught me everything I know around the wet/laser lab.

My years here may very well have resulted in my institutionalization without the partying, eating, drinking, lamenting, and laughing with these persons: Armon Sharei, Kevin Lin, Louisa Chiao, Kartik Trehan, and Jen Lee, I lack the words to describe the memories I have (clubs, restaurants, house parties, birthdays, trips) and how much I cherish them; Junwon Choi, Kyunghee Koh, and Peter Kyungchul Kang, who I connect with so profoundly and who kept me in my place or cheered me up as needed; SunMin May Hwang, James Jeongwon Lee, CJ Yu, YJ Kim, Wontae Cha, Wonjoon Choi, James Jongsup Hong, Yale Song, Hye-vin Kim, whom I can talk to frankly and who will always be honest and upfront with me; Tanguy Chau, who is always driving me to be a better person and whose energy I truly feed off of; James Thornton, who is a joy to talk to half-yearly, his elegance and well-spokenness always inspiring me to stop being tacky; Yoonju Hong, a friend that I never thought I would re-discover so far away from our homeland, who always finds me good enough to be proud of...I am truly humbled by your appreciation of me. There are many others whose support and jokes I couldn't have done without. You are all in my thoughts.

Without naming names, I would also like to thank the men who took me out to nice (and not so nice) places and told me sweet nothings. You have been instrumental in my Boston exploration and my adventures. Some of you taught me what I wanted,

yet more of you made me realize precisely what I could not stand. I have Gu to thank for this past half year's happiness, most of which was spent discovering/reaffirming what I found adorable and venerable. If things don't work out, I can always tell the story of how I dated a Hahvahd professor and you can always brag about how you dated this really young sexy thing.

Most importantly, I would like to express my gratitude for my family. My silent, moral, upright, and hardworking father, who has been my role model in weathering life and whose steadfast belief and pride in me - hardly supported by any logic or reason - have driven me. I strive to treat people as gently as he does, failing rather comically at times. My loving, expressive, fun, and intelligent mother lent me her love and prayers as my armor and pillar. My friendship with her helped me get through quite a few depressing moments, and her apt scoldings and wisdom helped me get through moments when I became weak. My humorous, good-natured, smarty-pants, sexy brother put my measly milestones on the most ridiculous pedestal and thus inspired me to become a better person.

I look forward to my life ahead, and I wish the best to everyone that came before me as well as to those that will come after me.